Abstract

PEEPLES, JOHANNA LOUISE. Design and Testing of Thermosyphon Batch Targets for Production of ^{18}F. (Under the direction of Joseph Michael Doster.)

^{18}F is a short-lived radioisotope commonly used in Positron Emission Tomography (PET). This radionuclide is typically produced through the $^{18}O(p,n)^{18}F$ reaction by proton bombardment of ^{18}O-enriched water. Thermosyphon batch targets have been proposed as a means to increase ^{18}F production due to their enhanced heat rejection capabilities. These boiling targets have been operated with up to 3.2 kW of beam power with manageable ^{18}O enriched water volumes. The primary purpose of this work has been to develop a fundamental approach to target design from a modeling perspective, and to implement this approach to design new thermosyphon targets with enhanced production capabilities. Computational methods have been developed to predict target thermal performance and have been validated with experimental test data from the Duke University Medical Cyclotron and the Wisconsin Medical Cyclotron. These methods have been used to design a new production target for the Duke cyclotron with enhanced ^{18}F production capabilities. Low volume test targets have been successfully operated at the Wisconsin cyclotron with beam powers in excess of the desired 1.6 kW.

Design and Testing of Thermosyphon Batch Targets for Production of ^{18}F

by

Johanna Louise Peeples

A dissertation submitted to the Graduate Faculty of
North Carolina State University
in partial fulfillment of the
requirements for the Degree of
Doctor of Philosophy

Nuclear Engineering

Raleigh, North Carolina

2008

APPROVED BY:

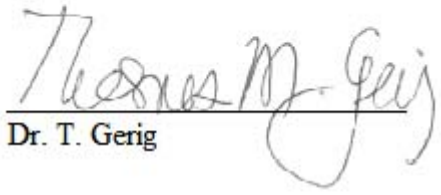

Dr. T. Gerig

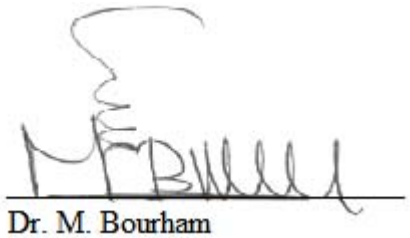

Dr. M. Bourham

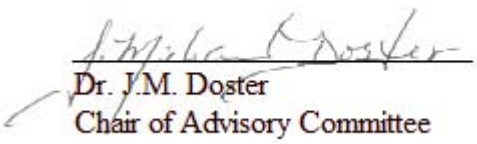

Dr. J.M. Doster
Chair of Advisory Committee

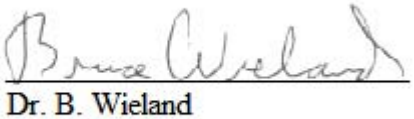

Dr. B. Wieland

Dedication

“There is a beauty in discovery. There is mathematics in music, a kinship of science and poetry in the description of nature, and exquisite form in a molecule. Attempts to place different disciplines in different camps are revealed as artificial in the face of the unity of knowledge. All literate men are sustained by the philosopher, the historian, the political analyst, the economist, the scientist, the poet, the artisan and the musician.”

— Glenn T. Seaborg, 1958

Biography

Johanna Louise Peeples was born in Durham, North Carolina in May of 1985 to Jane Cornelius and Wayne Cornelius. She was educated in the public school system and graduated from William G. Enloe High School in Raleigh, NC in 2002. Following her early graduation from high school, she began her college career at North Carolina State University. She graduated in May of 2005, with a Bachelor of Science degree in Nuclear Engineering, as a university valedictorian. While pursuing her B.S. degree, she met Cody Ryan Peeples, a graduate student in the Nuclear Engineering department, and they wed in June of 2006. She continued on at North Carolina State University to obtain her Master of Science degree in December of 2006 and Ph.D. in May of 2008, both in Nuclear Engineering.

Acknowledgements

I would like to thank all of the members of my graduate committee. I would like to thank Dr. Doster for all of his help and guidance in completing my degree. I would like to thank Dr. Bourham, my friend and mentor, for all of his faith in me and support over the last six years. I would like to thank Matt Stokely for his countless hours developing control systems, negotiating target construction, and performing beam tests at the Duke and Wisconsin facilities, without which validation of the modeling would not have been possible. I would like to thank everyone at the Positron Emission Tomography Facility at Duke University Medical Center, especially Dr. Bruce Wieland and Dr. Jerry Bida.

I would like to thank my parents for everything they have done for me and all that they continue to do. I would like to thank my sister for her help and encouragement. I would like to thank my husband, Cody, for all of his love and support, for believing in me and helping me to reach my goals.

Table of Contents

List of Tables

List of Figures

List of Symbols and Abbreviations

A – area (ft^2)

A_x – cross-sectional area (ft^2)

A_ω – cross-sectional area associated with ω (ft^2)

α – void fraction

Bo – Bond number

C_o – Wallis Equation coefficient

C_p – specific heat (Btu/lbm-F)

CFD – Computational Fluid Dynamics

d – jet exit diameter (ft)

D – diameter (ft)

D_e – equivalent diameter (ft)

D/d – ratio of the diameter of the impingement surface to the jet exit diameter

$-dE/dx$ – stopping power (MeV/cm)

E – proton energy (MeV)

f – friction factor

F – leading coefficient

F_{jet} – fraction of heat removed by jet cooling system

F_{rad} – fraction of heat removed by radial cooling

FDG – fluorodeoxyglucose

g – acceleration due to gravity ($32.2 \cdot 3600^2$ ft/hr^2)

g_c – conversion factor ($32.2 \cdot 3600^2$ ft-lbm/lbF-hr^2)

G – mass flux (lbm/hr-ft^2)

G_p – mass flux in piping (lbm/hr-ft^2)

G_T – mass flux in target channels (lbm/hr-ft^2)

G_ω – mass flux at location ω (lbm/hr-ft^2)

h_{CD} – condensing heat transfer coefficient (Btu/hr-ft^2-F)

h_{boil} – pool boiling heat transfer coefficient (Btu/hr-ft^2-F)

h_c – heat transfer coefficient (Btu/hr-ft^2-F)

h_{cool} – radial coolant heat transfer coefficient (Btu/hr-ft^2-F)

h_{fg} – enthalpy change by evaporation (Btu/lbm)

h'_{fg} – modified enthalpy change by evaporation (Btu/lbm)

h_{jet} – submerged jet impingement heat transfer coefficient (Btu/hr-ft^2-F)

h_{rad} – radial coolant heat transfer coefficient (Btu/hr-ft^2-F)

h_ω – heat transfer coefficient associated with ω (Btu/hr-ft^2-F)

H – total height (cm)

H_b – boiling height (cm)

H_{cd} – condensing height (cm)

I – beam current (μA)

k – thermal conductivity (Btu/hr-ft-F)

k_F – fluid thermal conductivity (Btu/hr-ft-F)

K_ω – forms loss coefficient associated with ω

l – fin length (in)

l_{back} – back thickness (in)

L – length (m)

Δm – change in mass (lbm)

$\dot{m}$ – mass flow rate (lbm/hr)

$\dot{m}_{jet}$ – mass flow rate in jet cooling system (lbm/hr)

$\dot{m}_{rad}$ – mass flow rate in radial cooling system (lbm/hr)

μ – dynamic viscosity (lbm/ft-hr)

Nu – Nusselt number

υ_F – kinematic viscosity (ft^2/hr)

P – target pressure (psi)

P_{exit} – exit pressure (psi)

P_{in} – inlet pressure (psi)

P_{ω} – pressure at location ω (psi)

ΔP – pressure difference between manifolds (psi)

PET – positron emission tomography

Pr – Prandtl number

Prz – pressure (psi)

q''_{avg} – average heat flux (Btu/hr-ft^2)

q'''_{avg} – average volumetric heat generation rate (Btu/hr-ft^3)

q''_{crit} – critical heat flux (Btu/hr-ft^2)

$q''_{\max z}$ – Zuber-Kutateladze critical heat flux (Btu/hr-ft^2)

$\dot{Q}_{boil}$ – boiling heat transfer rate (W)

$\dot{Q}_{cd}$ – condensing heat transfer rate (W)

$\dot{Q}$ – total rate of heat input (W)

Ra – Rayleigh number

Re – Reynolds number

R_{pta} – peak-to-average ratio

R_{pta}^{crit} – critical peak-to-average ratio

ρ – density (lbm/ft^3)

ρ_{cool} – density of coolant water (lbm/ft^3)

ρ_{eff} – effective average density of target water (lbm/ft^3)

$\rho_{\exp}$ – density of water expelled from target (lbm/ft^3)

ρ_f – fluid density (lbm/ft^3)

ρ_f^{sat} – fluid density at saturation (lbm/ft^3)

ρ_{fg} – density change by evaporation (lbm/ft^3)

ρ_g – vapor density (lbm/ft^3)

ρ_g^{sat} – vapor density at saturation (lbm/ft^3)

s – fin-to-fin spacing (in)

S – jet exit-to-impingement distance (ft)

S/d – ratio of the exit-to-impingement distance to the jet exit diameter

σ – surface tension (lbF/ft)

t – fin width (in)

T_{sat} – saturation temperature (°F)

T_{wall} – wall temperature (°F)

TS – thermosyphon

v_g – vapor velocity (ft/hr)

ΔV_{boil} – volume expelled due to boiling (μL)

$\Delta V_{\exp}$ – total volume expelled (μL)

ΔV_{th} – volume expelled due to thermal expansion (μL)

V_T – total volume (mL or cc)

WMC – Wisconsin Medical Cyclotron

ξ – expression which takes values $\in [0,1]$

Chapter 1

Introduction

1.1 Background

Positron emission tomography (PET) is a medical imaging technique that can provide a detailed map of molecular activity and biology in patients. PET has applications in oncology, neurology, cardiology, psychiatry, and pharmacology. In the field of oncology, fluorodeoxyglucose (FDG), a sugar, is used as a radiotracer. FDG is tagged with the positron emitting radioisotope Flourine-18 (^{18}F), which can be detected with PET scanning. When injected into the human body, FDG is absorbed and metabolized in cells which use glucose, releasing the ^{18}F which remains trapped in the cell. Higher uptake occurs in certain tissues, including the brain, the liver and cancerous cells. As a result, these high activity cells appear as bright spots on a PET image (Valk, 2003).

The physics of PET scanning is based on the positron emission of certain radionuclides. During this nuclear decay, a positron, or positively charged electron, is emitted. The positron travels only a short distance, 0.6 mm on average in human tissue for positrons emitted from ^{18}F, before colliding with an electron. This collision results in an annihilation of the electron-positron pair and leads to the emission of two annihilation photons. These photons each have 511 keV of energy, corresponding to the rest mass of the annihilated particles, and travel along a straight line in opposite directions. A PET scanner

detects the two photons in coincidence and creates a map from the intersecting decay lines (Valk, 2003).

^{18}F is a short-lived radioisotope, which decays by positron emission with a half-life of 109.77 minutes. This radionuclide is commonly produced through the $^{18}O(p,n)^{18}F$ reaction. A cyclotron is used to accelerate protons above the 2.4 MeV reaction threshold. The protons are focused into a beam and directed into a small volume of ^{18}O-enriched water. The ^{18}F produced is then chemically synthesized into FDG. Due to the short half-life, the production must occur in a cyclotron with a short delivery-time to the PET scanner. The ^{18}F activity can decay significantly over the course of a day, so PET facilities require either a cyclotron on-site or a nearby FDG distribution center (Nuclides, 1996).

Thermosyphon batch targets are one type of target used for ^{18}F production. These targets feature pressurization from the bottom and eliminate the presence of non-condensable gases. Protons deposit heat into the target water as they are slowed down, and the target water is permitted to boil during this process. The increased heat transfer due to boiling within the chamber and the absence of non-condensable gases both contribute to higher thermal capacity when compared to other batch boiling targets. Boiling conditions within the target chamber during operation are governed by the heat input and available cooling systems (Wieland, 2002).

Adequate cooling of the target is necessary to avoid over-pressurization of the target chamber or excessive voiding. Excessive voiding would allow the proton beam to penetrate to the back of the target, which would greatly reduce the yield of ^{18}F. Beam penetration to

the back of the target could also damage the walls of the chamber, and/or adversely affect the chemistry of the FDG produced.

1.2 Purpose

The primary purpose of this work was to develop a fundamental approach to target design from a modeling perspective, and to implement this approach to design new thermosyphon targets with enhanced production capabilities. The first step in accomplishing this task was to develop an understanding of the underlying heat transfer phenomena. Convective heat transfer, heat conduction, boiling dynamics within the target chamber, and boiling and condensing heat transfer are all important in characterizing the heat transfer capabilities of a batch boiling target. Knowledge of these phenomena can be used to develop computer models to predict target performance. These models allow researchers to predict the effects of changing target geometry and materials in the absence of, or with limited, expensive and time-consuming experiments. Prior to this work, target design was purely empirical, which required a significant amount of trial and error, long lead times and no guarantee of an optimal design.

Due to the high cost of enriched water and the limited size of FDG synthesis units, it is desirable for new targets to produce the maximum activity of viable ^{18}F with the minimum liquid volume. The production rate of ^{18}F is directly proportional to the proton beam current. As a result, the maximum ^{18}F activity will be produced using the maximum feasible beam current. The amount of heat deposited into the liquid volume, that must be removed to produce large ^{18}F yields, is also directly proportional to the beam current. Under ideal operating conditions, all of the protons are absorbed in the target water. This implies that the

rate of heat input into the target water is the same as the proton beam power, the product of the beam current and the proton energy.

If heat input exceeds the heat removal capability of the target, excessive voiding can occur in the target water. Protons of a given energy have a characteristic range in water which is inversely related to the water density. Since water density decreases with void fraction, the operating void fraction dictates the necessary target depth to prevent the beam from penetrating to the target back. If the proton beam penetrates the water volume and deposits heat in the back wall of the target, the ^{18}F yield will be reduced due to less proton interactions in the water. Interactions between the beam and the target wall can also release ions into the water, which react with the ionic ^{18}F to further reduce the yield. Beam penetration can not only reduce yields in the current batch, but can result in long-term or permanent contamination of the production target.

Adequate cooling of the target can prevent excessive voiding and prevent beam penetration. The optimal cooling configuration maximizes heat removal while minimizing the target water volume. This allows for the highest heat input, or highest acceptable beam current, and therefore produces the most ^{18}F. Minimizing the volume of enriched water needed to provide these conditions reduces the production costs. Computational models can be used to optimize target chamber dimensions and cooling configuration for a given cyclotron, with given beam characteristics.

The models developed in this work have helped guide the design of new targets, for both the Cyclotron Corp. CS-30 cyclotron at the Duke University Medical Center located in Durham, NC and the Wisconsin Medical Cyclotron located in Milwaukee, WI. Several new targets have been fabricated and tested experimentally at each facility, and the results of

these tests have been used to draw important conclusions about target behavior during operation, estimate practical thermal limits, and to validate the existing models. These experiments have demonstrated the capability of thermosyphon targets to produce high FDG yields at high beam power.

1.3 Related Work

Enriched ^{18}O water targets have been under development for more than 20 years. Conventional production targets are boiling liquid targets, which operate in batch mode. Many of these targets are used on small cyclotrons which can produce beam powers in the range of 300 to 1000 W. More than half of the installed base of PET cyclotrons in the US can produce higher beam powers, but losses associated with boiling have limited most conventional targets to operation below 1 kW. Several new targets capable of operating in the 2 kW range are currently under development. Target construction materials and associated water contamination has been shown to affect ^{18}F yields (Alvord, 2005).

Target yields at 79% theoretical maximum have been observed for a silver body, gold back target with small water volume and beam power up to 440 W (Roberts, 1995). Good yields have also been observed for a double foil, low pressure production target with silver body and Havar window foils at 340 W beam power (Berridge, 1999). A spherical niobium target with external water cooling has been operated at 650 W to produce 95% theoretical yield (Zeisler, 2000). Increased production yields have also been demonstrated using single foil targets constructed of niobium and titanium. These large volume, low pressure targets operate at beam power up to 850 W (Berridge, 2002). In recent years, tantalum has been used as a target material, due to its good oxidation resistance. Production yields have been

increased using a compact tantalum target with maximum beam power approaching 1 kW (Alvord, 2005). A horizontal beam niobium target has been demonstrated at 2.3 kW heat input and 4 mL volume (Strangis, 2007).

Bruce Technologies, Inc. has been investigating the use of thermosyphon batch boiling targets for ^{18}F production for the past eight years (Wieland, 2006). The targets are initially filled with water, and pressure is applied to the bottom of the target to produce a self-regulating condensing surface. Early thermosyphon targets with 1 mL water volume operated at 440 W beam power. Experiments have been performed at higher beam powers, and enhancements have been made in successive designs to increase yield. Experiments have indicated that thermosyphon targets are capable of operation with beam power in excess of 1 kW (Roberts, 2002). Computational methods have been developed that can be used to design new thermosyphon targets (Peeples, 2006). Thermosyphon targets have been tested at both the Duke University Medical Center cyclotron and the Wisconsin Medical Cyclotron, with beam power as high as 2.3 kW.

Alternate target designs have been proposed to increase production of ^{18}F. Recirculating targets which remove heat through an external heat exchanger have been demonstrated to reject high heat inputs. A prototype recirculating target was shown to reject heat inputs above 2.7 kW at atmospheric pressure (Clark, 2004). Rejection of 6 kW has been demonstrated using a small shell and tube heat exchanger. Rejection of 7.6 kW has been demonstrated using a small cross-flow heat exchanger with predicted peak performance of 10 kW (Newnam, 2007). Recirculating targets require greater water volumes than boiling targets but are capable of operating at much higher beam powers.

Chapter 2

Review of Thermosyphon Target Design

2.1 Materials

The major components of a thermosyphon target include the target chamber, target body or housing and the target window.

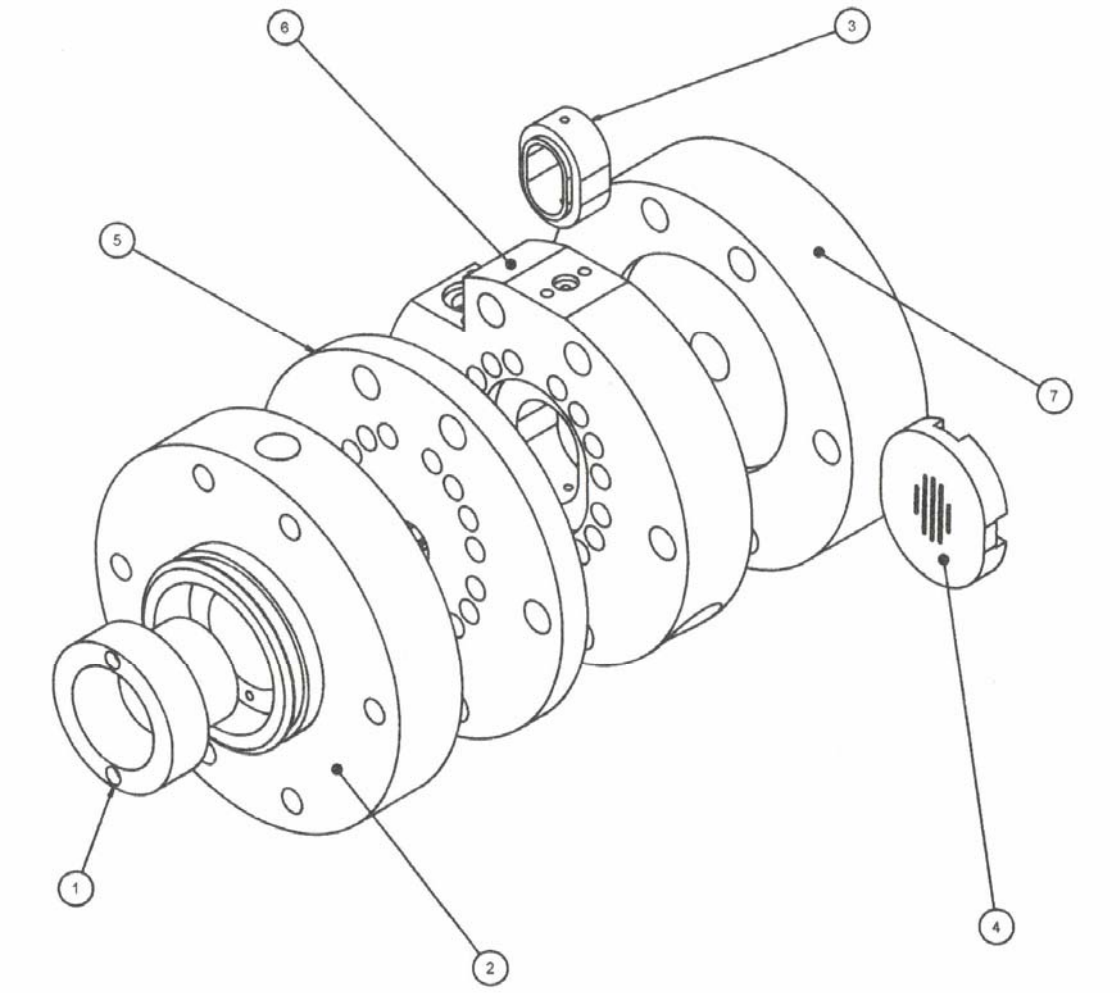

Figure 1: TS-5 Assembly Drawing (Mark Humphrey 2005)

Table 1: TS-5 Target Parts List

Item	Description
1	Shadow Grid (Body)
2	Front Flange (Body)
3	Target Chamber
4	Target Chamber Back
5	Intermediate Flange (Body)
6	Target Flange (Body)
7	Back Flange (Body)

The target window is a thin metal foil through which the proton beam enters the target chamber. The target window should be thin enough to allow protons to enter with minimum attenuation, generally 12 to 50 μm, but must be thick enough to withstand the high target operating pressure. Use of a light material is also desirable to minimize beam attenuation. The window material should have high mechanical strength, high resistance to radiation damage, and a high melting point. High thermal conductivity is preferred to facilitate cooling of the foil. Because the foil is in contact with the target water, a material should be selected to minimize chemical contamination of the water and synthesized FDG. Common window materials include beryllium copper, titanium, tantalum, and most frequently a proprietary alloy called Havar.

The target chamber internals are also in contact with the target water. Chemical compatibility, i.e. low potential for contamination, is a key concern. High thermal conductivity, for effective cooling, is also highly preferred. As with the window, high melting point, high material strength, and good corrosion resistance are important. Beam interactions with the metal foil and the metal target internals can result in formation of metal ions. The ions can interact with the ^{18}F, which is also produced in an ionic form.

Contamination from the target materials pollutes the target water and can significantly reduce the yield of ^{18}F.

The target housing supports the target window and internals and allows it to be properly positioned on the cyclotron beam line. The target housing should be durable, have high strength, and high resistance to radiation damage and activation. During long production runs with high beam currents, activation can be significant.

In the past, silver has been used for the target chamber due to its high thermal conductivity and above average chemical compatibility. Aluminum has also been used in target bodies due to its high thermal conductivity, ease of machining, and low cost. Poor chemical compatibility, however, required the use of a protective coating or film to separate the target water from the aluminum. Tantalum is an attractive interface material due to its excellent chemical compatibility, but suffers from a relatively low thermal conductivity. Tantalum inserts, press fit into an aluminum target body, were examined, but early designs exhibited high thermal resistance due to large conduction distances and high contact resistance at the aluminum/tantalum interface. Experiments by researchers at Duke University are examining the feasibility of chemical vapor deposition coating of aluminum with tantalum. Successful sputtering of tantalum onto aluminum could yield a surface with the chemical inertness of tantalum and the high thermal conductivity of aluminum. While the feasibility of this method is being determined, target designs are being developed with internals constructed of pure tantalum. Tantalum is expensive, difficult to machine and has much lower thermal conductivity, but the chemical compatibility must take precedence to ensure a high ^{18}F yield. High power tantalum targets are feasible because the low thermal conductivity of tantalum can be compensated for by reducing the conduction distance.

Aluminum can be used for the target housing due to its low cost and ease of machining. Since the target cooling systems can be located completely within the tantalum internals, good thermal contact between the internals and the housing is not necessary.

2.2 Particle Energy

The Duke Medical Center cyclotron accelerates protons to a maximum of 26 MeV and focuses them into a narrow beam. The Wisconsin Medical Cyclotron accelerates protons to a maximum of 16.5 MeV. The protons in the beam lose a small amount of energy when they pass through the window into the target chamber. The protons then lose additional kinetic energy as they travel through the water due to charged particle interactions and bremsstrahlung. Bremsstrahlung losses are radiation losses that occur as a charged particle slows down in a material.

The incremental energy loss of the proton per unit of distance traveled in the media $\left(-dE/dx\right)$ is defined to be the stopping power. The stopping power changes with the energy of the proton as it travels farther into the water, and can be shown to increase to a peak near the end of the particle path and then decrease suddenly to zero (Faw, 1999).

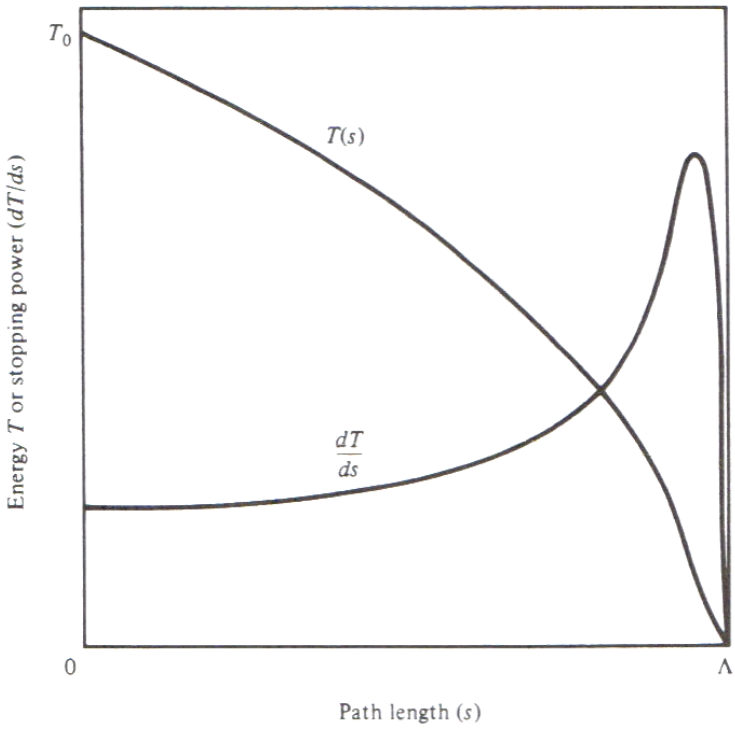

Figure 2: Variation of Stopping Power and Energy along Charged Particle Path (Faw, 1999)

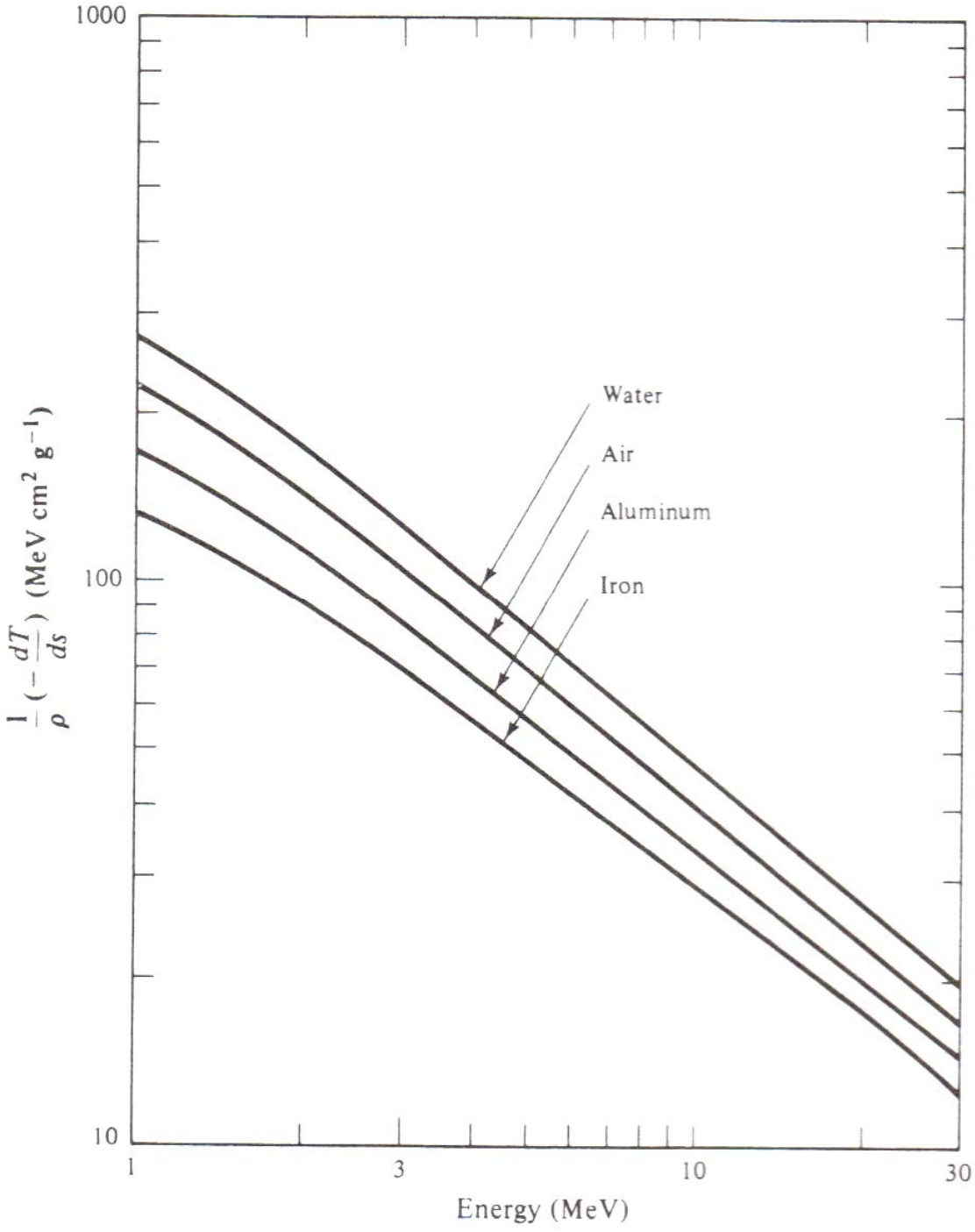

Figure 3: Collisional Stopping Power for Protons in Air, Water, Aluminum, and Iron (Faw, 1999)

The majority of the heat is deposited in the region where the stopping power is the greatest. With the deposition of heat, the water density decreases and vapor voids are formed. Higher incident proton energies result in lower stopping power, and therefore deeper penetration into the water volume. The range of the protons is the average distance that they will travel in the water before being stopped (Faw, 1999).

To prevent the proton beam from striking the back wall of the target, the target must be range thick. In other words, the target depth should exceed the range of the protons in the saturated mixture. The range of protons with incident energy between 8 and 30 MeV in water at 300 psi saturation conditions and various void fractions was determined using The Stopping and Range of Ions in Matter program (SRIM). The desired operating pressure of the Duke target is between 300 and 400 psi and was chosen to limit stress on the beam window and accommodate the pressure rating of the valves in the target system.

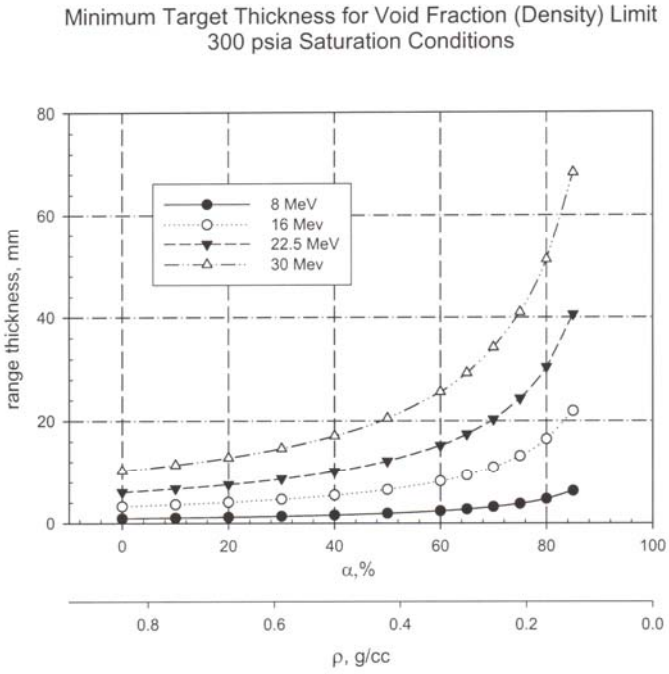

Figure 4: Range Thickness for Protons in 300psi Saturated Water (Matthew Stokely 2006)

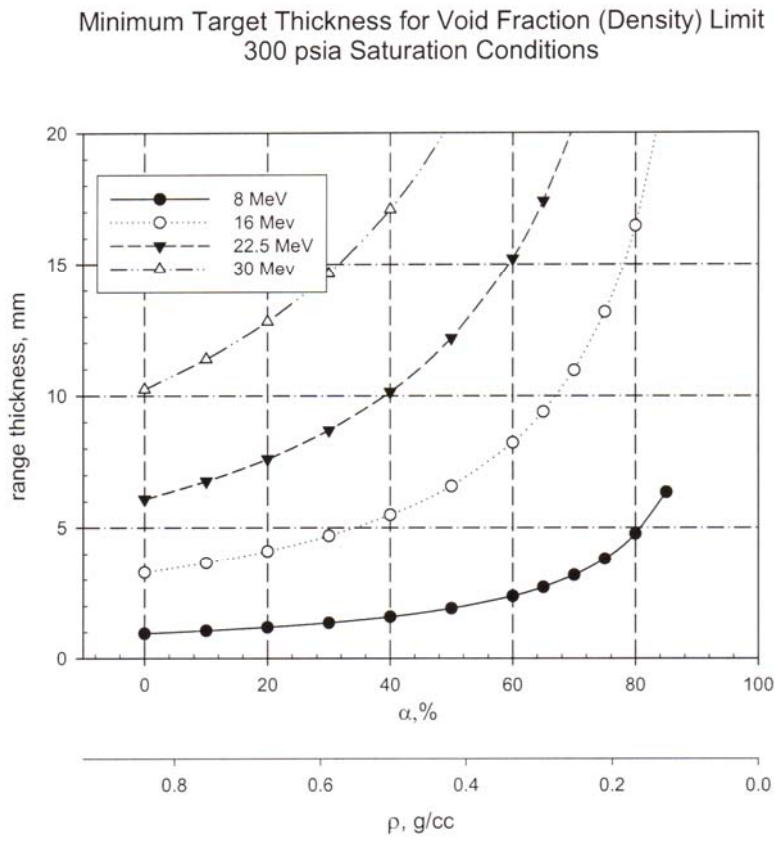

Figure 5: Range Thickness for Protons in 300psi Saturated Water (Matthew Stokely 2006)

The depth of the target chamber dictates the maximum amount of voiding that can be tolerated. A depth of 15 mm was selected for the Duke target by the Cyclotron Director, Dr. Gerald Bida. During operation of Duke targets, protons will be accelerated to 26 MeV. For most of the experimental test work performed at Duke, however, protons were accelerated to 22 MeV, rather than the 26 MeV maximum. For operation at 22 MeV, Figure 5 implies the target should be designed to ensure that the average void fraction in the path of the beam would never exceed 60%. For operation at 26 MeV, the target should provide range thickness for void fractions as high as 47%. During operation at the Wisconsin Medical

Cyclotron, protons will be accelerated to 16.5 MeV. A 15 mm depth should provide range thickness for void fractions as high as 76%.

2.3 Heat Input

The heat input $(\dot{Q})$ to the target is a function of the beam current and the energy of the incident protons. Beam current (I) is quantified in micro-amps (μA) and proton energy (E) is quantified in mega-electron volts (MeV).

$$\dot{Q}(W) = I(\mu A) \cdot \left(\frac{10^{-6}\, C/s}{1 \mu A} \right) \cdot \left(\frac{1}{1.6 \cdot 10^{-19}\, C/p^{+}} \right) \cdot E\left(MeV/p^{+} \right) \cdot \left(\frac{1.6 \cdot 10^{-13}\, J}{1 MeV} \right) \left(\frac{1W}{1\, J/s} \right)$$

$$\dot{Q}(W) = I(\mu A) \cdot E_p\left(MeV/p^{+} \right)$$

The beam power in Watts, which is equivalent to the heat input, can be determined directly by taking the product of the beam current in μA and the incident proton energy in MeV.

2.4 Thermal Limit

There are two proposed modes of operation for thermosyphon targets, as illustrated in Figure 6. The operating mode for a given target design will depend on the size of the target chamber and the magnitude of the heat input. A thermosyphon target is designed to allow considerable boiling in the target chamber to take advantage of the high rate of heat transfer. Heat deposition in the water causes boiling, and results in the formation of voids or bubbles. Buoyancy forces cause these bubbles to rise, and condensation on the ceiling of the target may occur. The two potential modes of target operation can be described as (a) the

formation of a distinct condensing region in the top of the target and (b) turbulent boiling in the target chamber without the formation of a distinct condensing region.

The condensing region mode of operation implies that bubbles which rise to the top of the target enter a distinct condensing region. Steam condenses on the chamber walls and flows back down the walls into the boiling pool. Under steady-state operation, there will be a pool of boiling water with some height (H_b) and above it will be a completely voided condensing region with some height (H_{cd}). These regions compose the total height of the target chamber $(H = H_b + H_{cd})$.

The turbulent boiling mode of target operation implies that turbulent boiling occurs in the target without the formation of a distinct condensing region $(H = H_b)$. This boiling mode is characterized by high levels of turbulent mixing resulting in bubble condensation and collapse.

Thermosyphon targets operating under either boiling mode are self-regulating, in that the boiling height and/or average void in the boiling region will change according to the heat input. The water level and/or average void will attain a value such that the amount of heat being removed via cooling equals the heat input.

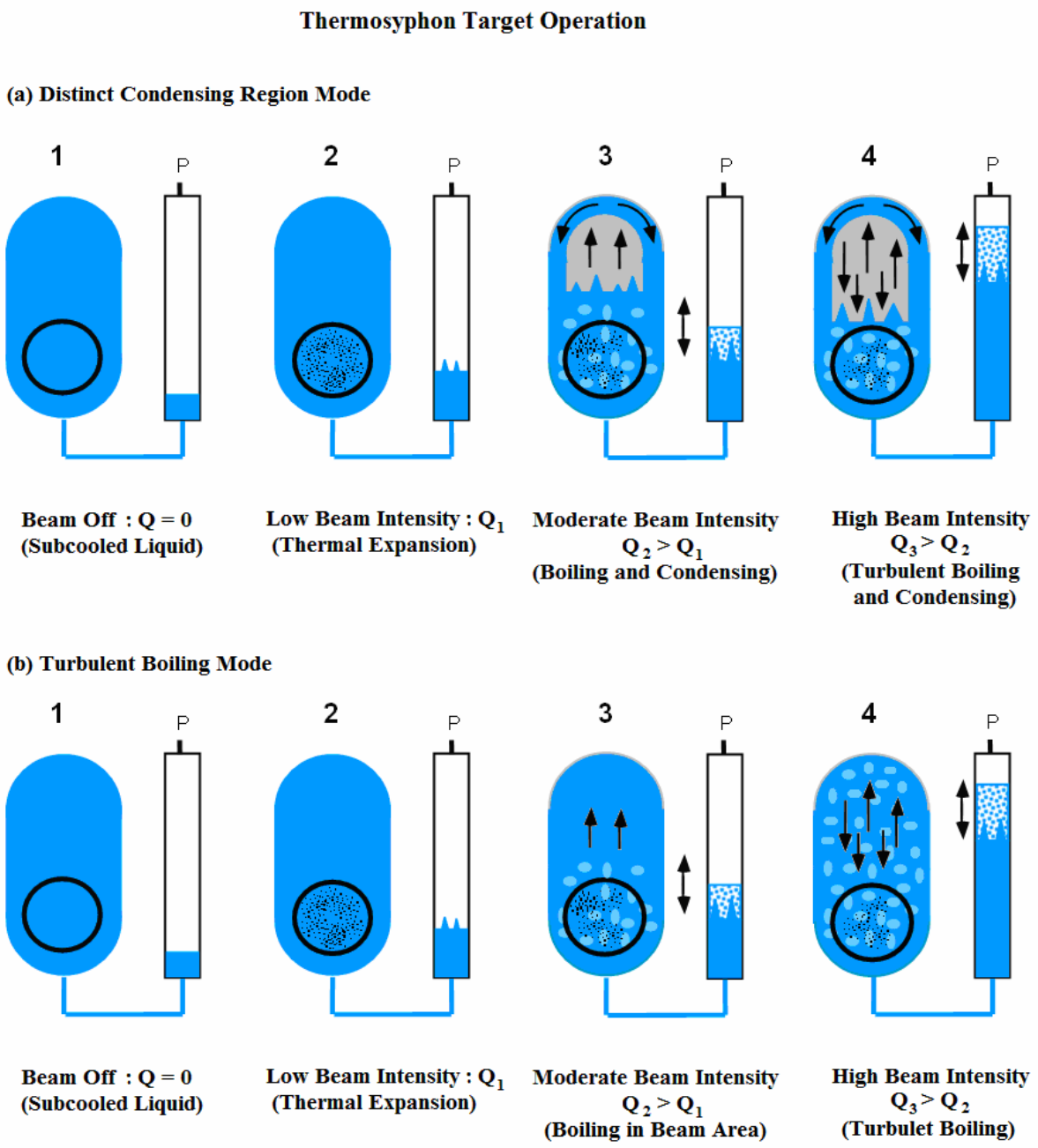

Figure 6: Thermosyphon Target Operation (Images: Bruce Wieland 2005)

Protons accelerated in the cyclotron are focused into a narrow beam. The optics of this beam vary for each cyclotron and must be characterized for target design. The proton beam passes through a circular window and enters the target water volume. The Duke target

requires a 10 mm diameter beam window. This window is positioned near the bottom of the target to increase the chances that the beam enters a boiling region of the water volume rather than a condensing region.

If the boiling water level drops below the height of the beam window, in the presence of a distinct condensing region, there will be insufficient water density to maintain range thickness and some of the beam can penetrate to the target back. The thermal limit of a target is then defined to be the minimum heat input that will result in either (1) the average void fraction in the path of the beam exceeding the value necessary for the target to remain range thick or (2) the boiling height falling below the height of the beam window. For Duke targets, these values are approximately 47% and 10 mm, respectively. For Wisconsin targets, these values are approximately 76% and 15 mm, respectively. It should be noted, that operation of the target is still possible above the defined thermal limit, though ^{18}F yields will suffer and ultimately target damage can occur.

2.5 Integrated Target System

The most recent thermosyphon target designs feature cooling of the target chamber by two independent systems as illustrated in Figure 7. Radial coolant channels are located around the target chamber and run parallel to the target chamber and the direction of the beam. Additional cooling is provided by a jet of water which impinges on the back of the target. Heat deposited in the target causes the water temperature to rise and heats the walls of the target chamber. This heat conducts through the walls of the chamber and is then removed by either the radial coolant channels or the jet system. Many commercial targets rely on

cooling through a single jet on the back of the target. The use of radial cooling can result in increased heat removal capability for the same water volume.

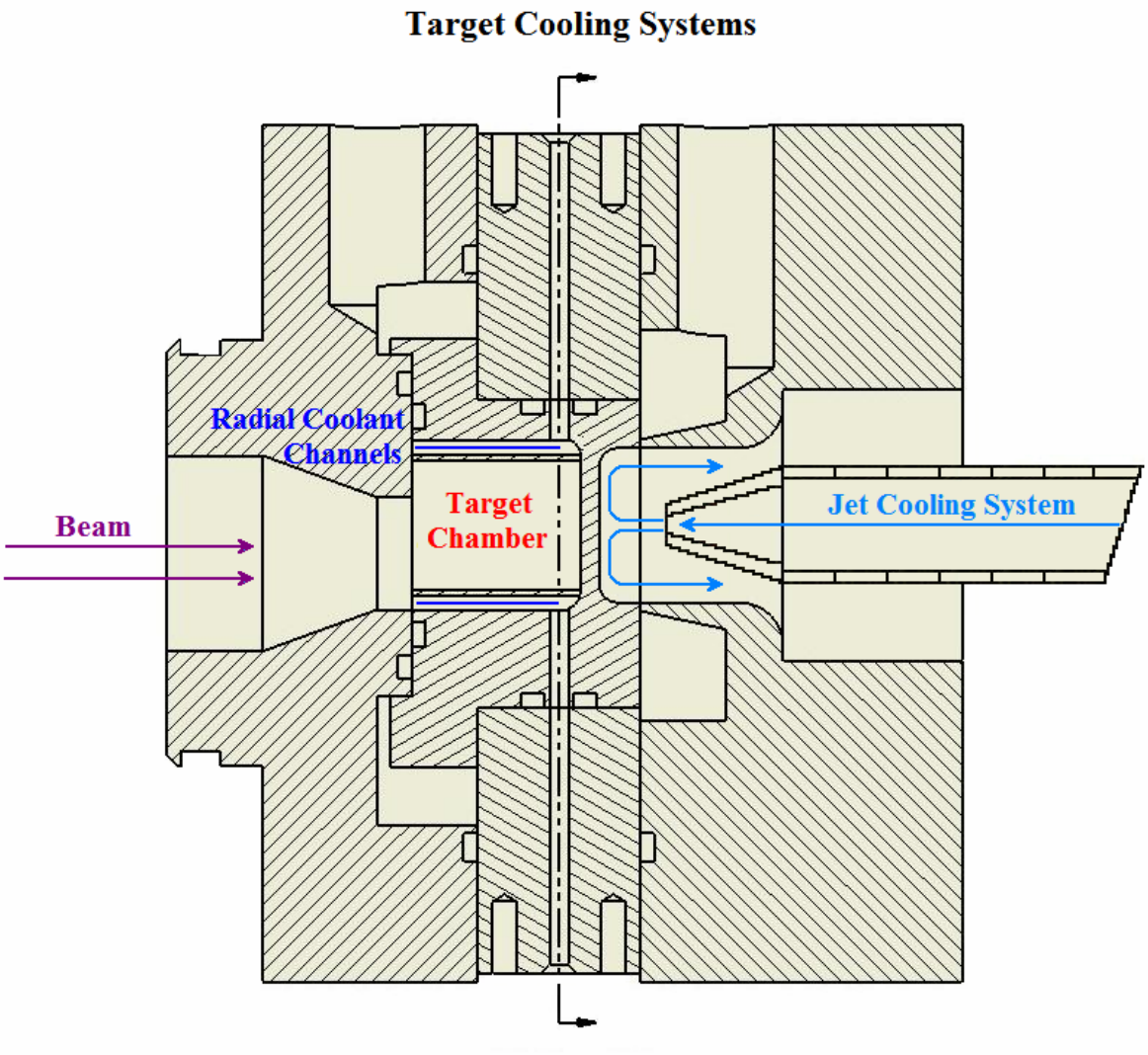

Figure 7: Axial View of Target Cooling Systems (Mark Humphrey and Johanna Peeples 2006)

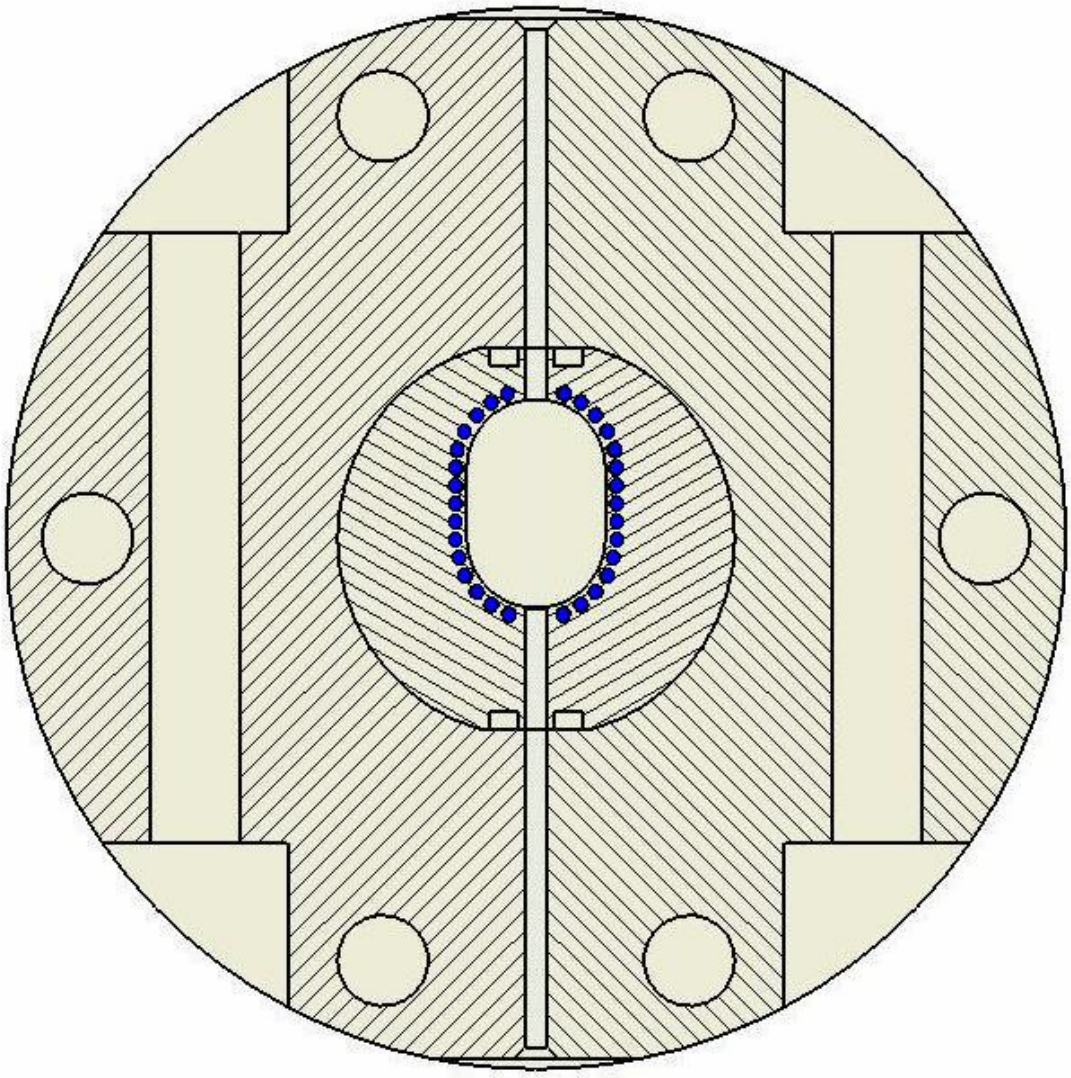

Figure 8: Radial View of Target Cooling Systems (Mark Humphrey and Johanna Peeples 2006)

Chapter 3

Overview of Original Thermosyphon Target Model

A detailed overview of prior thermosyphon modeling techniques developed in support of this research work is available (Peeples, 2006).

3.1 Radial Coolant Channels

Most cyclotron facilities contain a large volume of cool water in an inlet manifold which provides cooling water to the cyclotron. Coolant flow is driven by a manifold pressure difference, typically on the order of 70 psi, between inlet and outlet manifolds. Pressure losses occur in the piping that connects the radial cooling system to the manifolds. Additional pressure losses occur within the radial channels as a result of wall friction, manifold losses, and bends in the channels and piping. Coolant flow in the radial channels is estimated using characteristic forms losses. Coolant mass flow rate, along with known coolant temperature, will determine the heat removal capability of the radial channels for a given target.

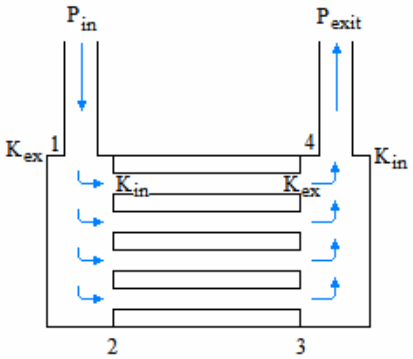

Figure 9: Mass Flow through Radial Coolant Channels

The total pressure drop across the radial coolant system can be written as

$$P_{in} - P_{exit} = \left\{ \left(\frac{fL}{D} \right)_p + K_p + K_{ex} + K_{in} \right\} \frac{G_p{}^2}{2\rho g_c} + \left\{ K_{in} + K_{ex} + \left(\frac{fL}{D} \right)_T \right\} \frac{G_T{}^2}{2\rho g_c} \quad (1)$$

In Equation 1, the subscript p refers to the flows in the smooth plastic piping that connects the water manifolds to the target. The subscript T refers to the flows within the target. Appropriate values for the various loss coefficients can be found in classic literature or determined experimentally.

The friction factor can be expressed as a function of the Reynolds number, which in turn is a function of the mass flux. Conservation of mass can be used to restate the total pressure loss equation in terms of the total mass flow rate in the radial coolant system.

$$\Delta P = \left\{ \frac{L_p}{D_p} a_p \left(\frac{D_p}{\mu A_p} \right)^{b_p} \dot{m}^{b_p} + K_p + K_{ex} + K_{in} \right\} \frac{\dot{m}^2}{2\rho g_c A_p{}^2} + \left\{ K_{in} + K_{ex} + \frac{L_T}{D_T} a_T \left(\frac{D_T}{\mu A_T} \right)^{b_T} \dot{m}^{b_T} \right\} \frac{\dot{m}^2}{2\rho g_c A_T{}^2} \quad (2)$$

Equation 2 can be solved implicitly for the mass flow rate.

The heat removal capability of the radial channels is estimated using a heat transfer coefficient (h_{rad}) and the known coolant fluid temperature. The heat transfer coefficient for the radial channels is estimated using the Dittus-Boelter equation under the condition of the fluid being heated (Incropera, 2007).

$$h_{rad} = 0.023 \frac{k}{D_e} \left(\frac{\dot{m} D_e}{A_x \mu} \right)^{0.8} \left(\frac{C_p \mu}{k} \right)^{0.4} \quad (3)$$

3.2 Jet Cooling System

Additional cooling for the target is achieved by jetting cool water from the cyclotron inlet manifold onto the back of the target. Radial and jet coolant flows can be run in series, or the two can be run in parallel to maximize coolant flow and available cooling in each system.

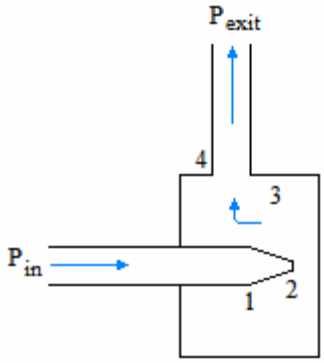

Figure 10: Mass Flow through Jet Cooling System

Many correlations have been developed for heat transfer coefficients associated with cooling from submerged jets (Brdlik, 1965; Sitharamayya, 1969; Martin, 1977; and Womac, 1993). These correlations are generally based on the geometry of the jet and of the impingement surface. The geometry of this type of jet can be evaluated based on two dimensionless ratios: the ratio of the exit-to-impingement distance to the jet exit diameter (S/d) and the ratio of the diameter of the impingement surface to the jet exit diameter (D/d) (Womac, 1993).

The prior thermosyphon model employed a jetting heat transfer correlation valid over a wide range of Reynolds numbers (Martin, 1977). This correlation provides that the Nusselt number is

$$Nu = \frac{d}{D}\frac{\left[2 - 4.4\frac{d}{D}\right]}{\left[1 + 0.2\left(\frac{S}{d} - 6\right)\left(\frac{d}{D}\right)\right]} F\left(\mathrm{Re}_d\right)\mathrm{Pr}^{0.42} \tag{4}$$

where

$$F\left(\mathrm{Re}_d\right) = 2\,\mathrm{Re}_d{}^{0.5}\left[1 + \frac{\mathrm{Re}_d{}^{0.55}}{200}\right]^{0.5}$$

and is valid for submerged water jets with $2 \le S/d \le 12$, $5 \le D/d \le 15$, and $2000 \le \mathrm{Re}_d \le 400{,}000$.

Coolant mass flow rate in the jet system can be determined using characteristic forms losses. For parallel cooling systems,

$$P_{in} - P_{exit} = \left\{\left(\frac{fL}{D}\right)_p + K_p + K_{in}\right\}\frac{G_p{}^2}{2\rho g_c} + \left\{K_n + K_{baffle}\right\}\frac{G_2{}^2}{2\rho g_c} + \left\{K_{90}\right\}\frac{G_3{}^2}{2\rho g_c} \tag{5}$$

Appropriate values for the various loss coefficients can be found in classic literature or determined experimentally. When the mass flux and Reynolds number associated with each section of piping are written in terms of the mass flow rate, the pressure balance is

$$\Delta P = \left\{\frac{L_p}{D_p} a_p \left(\frac{D_p}{\mu A_p}\right)^{b_p} \dot{m}^{b_p} + K_p + K_{in}\right\}\frac{\dot{m}^2}{2\rho g_c A_p{}^2} + \left\{K_n + K_{baffle}\right\}\frac{\dot{m}^2}{2\rho g_c A_2{}^2} + \left\{K_{90}\right\}\frac{\dot{m}^2}{2\rho g_c A_3{}^2} \tag{6}$$

Equation 6 can be solved implicitly for the mass flow rate.

3.3 Target Chamber

The original thermosyphon model for the target chamber was developed assuming a steady-state boiling condition with distinct boiling and condensing regions. These regions consist of a boiling mixture region in the bottom of the target and a condensing vapor region in the top of the target.

Heat transfer from the boiling region is modeled using a boiling heat transfer coefficient which depends on the void fraction and the boiling height.

$$h_{boil} = \frac{k_F}{H_b} Nu \tag{7}$$

The Nusselt number for volumetrically heated pools is often correlated in the form (Wen, 2006)

$$Nu = cRa^a \tag{8}$$

Proposed values for the correlation parameters yield

$$Nu = \begin{cases} 1.54Ra^{1/4} & Ra \le 1.865 \cdot 10^{11} \\ 0.0314Ra^{0.4} & Ra > 1.865 \cdot 10^{11} \end{cases} \tag{9}$$

where the Rayleigh number is defined to be

$$Ra \equiv \frac{g\alpha {H_b}^3 \,\mathrm{Pr}}{{\upsilon_F}^2} \tag{10}$$

The void fraction in the boiling region is estimated assuming steady state conditions as a function of the height of the condensing region (H_{cd}) to be

$$\alpha = \frac{\xi(H_{CD})}{1 + C_o \xi(H_{CD})} \tag{11}$$

$$\text{where} \quad \xi(H_{CD}) = \frac{\dot{Q}_{cd}(H_{CD})}{\rho_g v_{g_j} A_x h_{fg}}$$

Heat transfer from the condensing region is modeled using a condensing heat transfer coefficient (Incropera, 1996).

$$h_{CD} = 0.943\left[\frac{g_c \rho_f \rho_{fg} k^3 \left[h_{fg} + 0.68 C_p (T_{sat} - T_{wall})\right]}{\mu (T_{sat} - T_w) H_{CD}}\right]^{1/4} \tag{12}$$

The total heat input to the target, which corresponds to the total heat transfer rate, is expressed as a single nonlinear equation in the condensing height (Peeples, 2006). This equation is solved iteratively to yield condensing height and the total heat transfer rates from the boiling and condensing regions.

3.4 Integrated Model

The original integrated thermosyphon target model, which assumes the formation of a distinct condensing region, consists of a FORTRAN code coupled with a COMSOL Multiphysics program. The COMSOL Multiphysics program uses finite element techniques to solve partial differential equations to determine radial temperature profiles in a specified target under given operating conditions. The COMSOL solution for wall temperatures and boiling and condensing heat transfer rates in the radial direction is used in the FORTRAN code to evaluate the total target heat input as a function of condensing height. Iteration between the FORTRAN code and COMSOL model will yield a converged solution for heat input and corresponding condensing height.

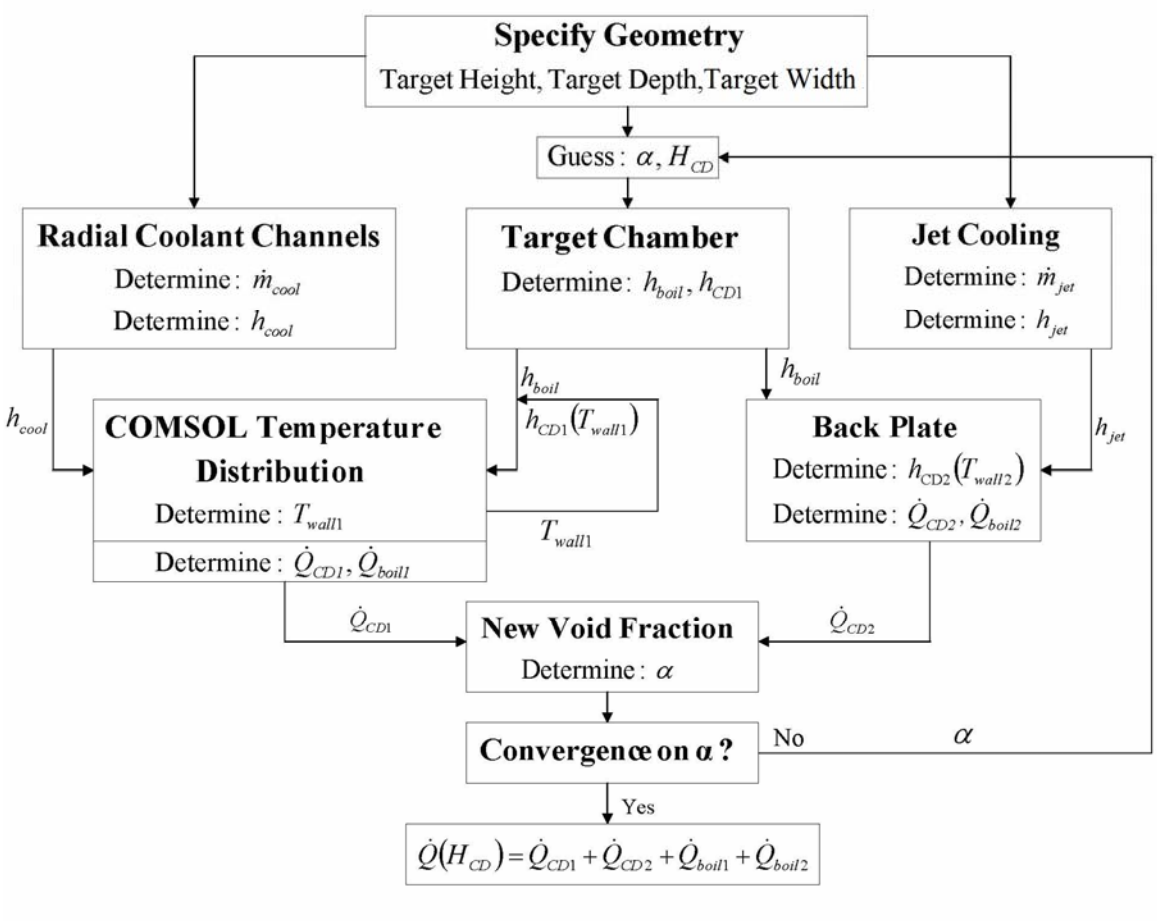

Figure 11: Flow Chart for FORTRAN Solution of Heat Input

Chapter 4

Modifications to Original Thermosyphon Target Model

4.1 Volume Averaged Boiling

The thermosyphon target model developed in previous work assumed steady state boiling conditions in the target chamber during operation that consisted of distinct boiling and condensing regions. An alternate boiling dynamic that could exist in the target chamber during operation is turbulent boiling, without formation of a distinct condensing region. This boiling mode can be modeled, assuming volume averaged boiling, with minor modification to the original target chamber model.

When using a purely volume averaged boiling target model, heat input is no longer described by a single nonlinear equation in the condensing height. The correlation for the boiling heat transfer coefficient, presented earlier in this work, was used to generate coefficients for a suite of target chamber void fractions. These coefficients were applied for the entire target chamber region in the absence of any condensing area. The FORTRAN/COMSOL model was then used to predict the heat input corresponding to each void fraction. Under these modified conditions, the heat input can be calculated directly without iteration.

During experiments, the void fraction in the target cannot be measured directly. Instead, the amount of water displaced from the target during operation is observed. A straightforward relationship exists between the void fraction in the pure boiling mode and the

predicted amount of water displaced from the target chamber during operation. This allows for direct comparison between experimental data obtained over a suite of pressures and heat inputs and target behavior predicted by the model under conditions of volume averaged boiling.

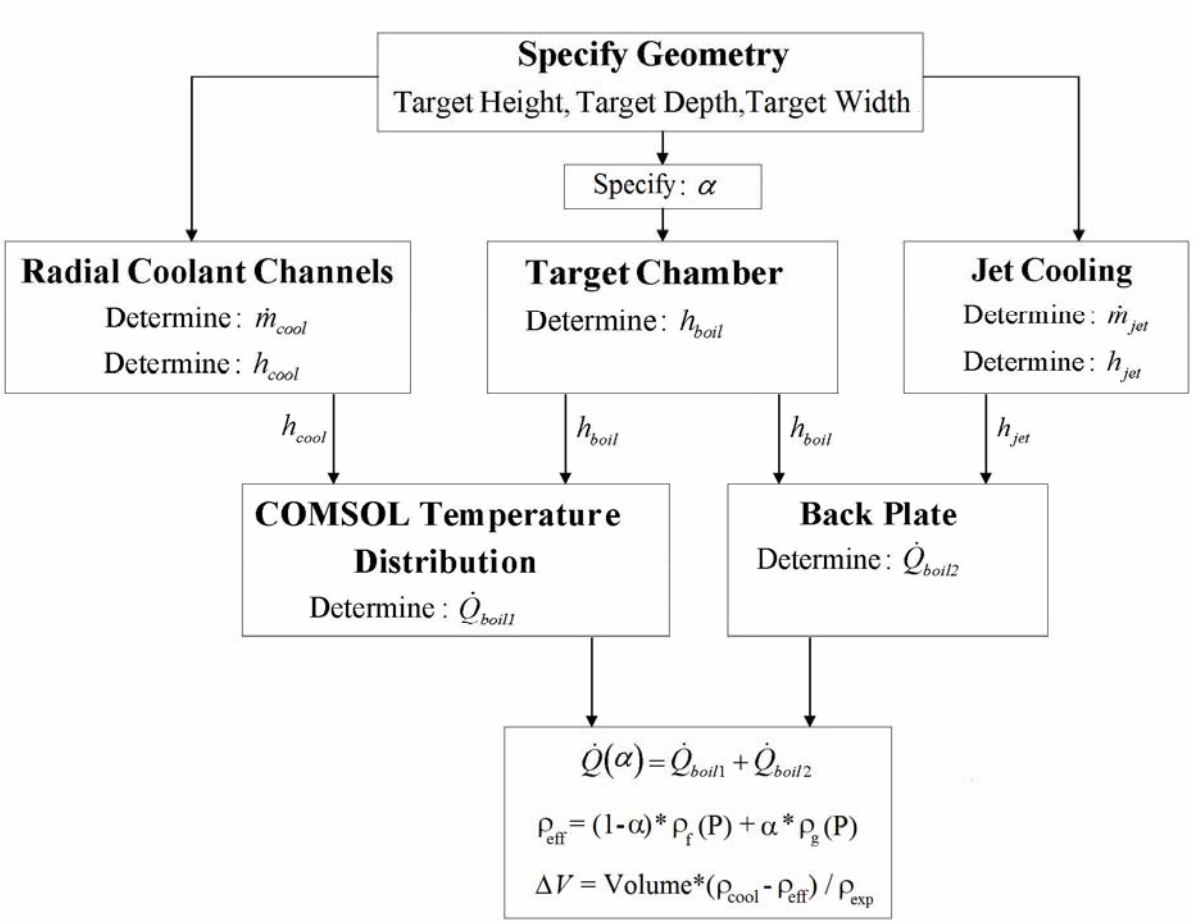

Figure 12: Flow Chart for Modified FORTRAN Solution of Heat Input

Before operation, the target chamber is filled with room temperature water and brought to the desired operating pressure. During operation, the cyclotron beam heats the target water, causing the temperature in the target chamber to rise to the saturation temperature. After reaching the saturation temperature, volumetric boiling can occur

throughout the target chamber. Some amount of water volume is expelled from the target due to thermal expansion as the water is heated from room temperature to saturation. As more heat is deposited in the target, vapor forms in the chamber and additional water is expelled. The total volume expelled (ΔV_{exp}) is the sum of the volume expelled due to thermal expansion (ΔV_{th}) and the volume expelled as a result of boiling (ΔV_{boil}).

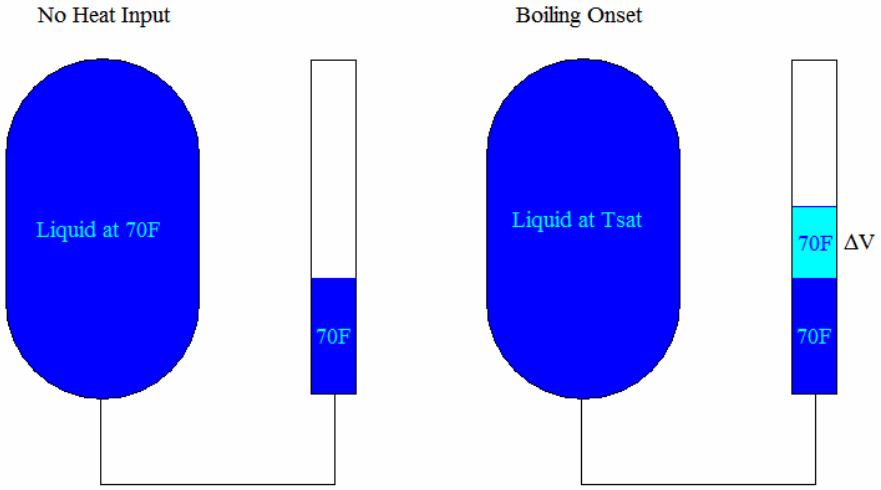

Figure 13: Water Volume Expelled due to Thermal Expansion

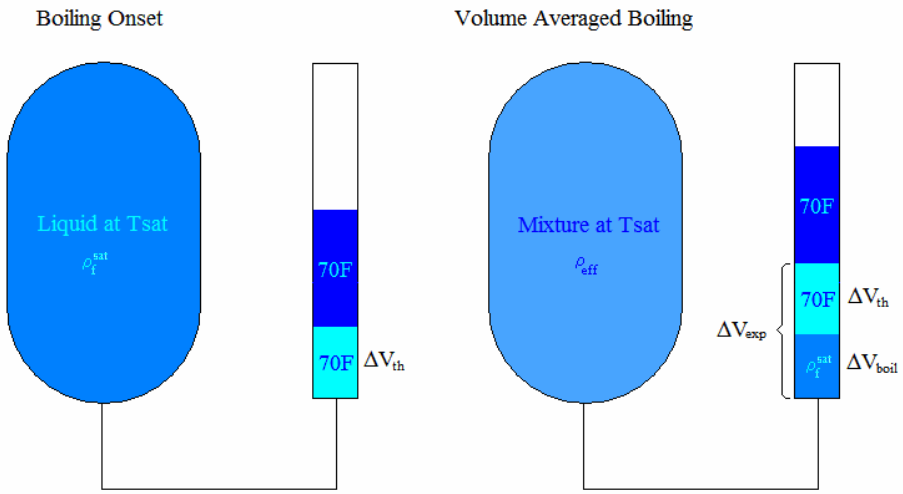

Figure 14: Water Volume Expelled due to Boiling

The volume expelled as a result of thermal expansion can be determined by taking the ratio of the change in mass within the target chamber to the initial density of the water before heating.

$$\Delta V_{th} = \frac{\Delta m}{\rho_{cool}} = \frac{V_T \rho_{cool} - V_T \rho_f^{sat}}{\rho_{cool}} = V_T \left(\frac{\rho_{cool} - \rho_f^{sat}}{\rho_{cool}} \right) \tag{1}$$

The total amount of water expelled as a result of boiling can be calculated in a similar fashion.

$$\Delta V_{boil} = \frac{\Delta m}{\rho_f^{sat}} = \frac{V_T \rho_f^{sat} - V_T \rho_{eff}}{\rho_f^{sat}} = V_T \left(\frac{\rho_f^{sat} - \rho_{eff}}{\rho_f^{sat}} \right) \tag{2}$$

Under boiling conditions, the effective density in the target chamber can be determined as a function of the void fraction in the target and the target pressure.

$$\rho_{eff} = (1 - \alpha) \cdot \rho_f^{sat} + \alpha \cdot \rho_g^{sat} \tag{3}$$

The total volume expelled is the sum of contributions from thermal expansion and boiling.

$$\Delta V_{\exp} = \Delta V_{th} + \Delta V_{boil} \tag{4}$$

4.2 Jetting Heat Transfer Coefficient

Different correlations for heat transfer coefficients have been developed for submerged jets. The original thermosyphon model employed a correlation developed by Martin in 1977 due to its applicability over a wide range of Reynolds number. An additional correlation was added to the thermosyphon model to allow for other geometric configurations of the jet under which the Martin correlation is not valid. The following correlation has been

proposed for submerged water jets with $S/d \le 6.2$, $1.67 \le D/d \le 18.75$, and $2000 \le \mathrm{Re} \le 20000$ (Brdlik, 1965). This correlation suggests a Nusselt number of

$$Nu_D = 1.54\,\mathrm{Re}_D^{0.5}\,\mathrm{Pr}^{0.33} \tag{5}$$

The disadvantage to using this correlation is that it is not demonstrated to be valid at high values of the Reynolds number. When using this correlation, the Reynolds number in the jet is monitored to assure it does not exceed the range of validity by a significant margin.

4.3 Condensing Heat Transfer Coefficient

Correlations for condensing heat transfer coefficients have been developed for various liquid conditions. The original thermosyphon model assumed formation of a distinct condensing region and modeled the condensing heat transfer coefficient using a correlation developed for film condensation on a vertical plate. An additional model was considered which assumed formation of a distinct condensing region and employed a condensing heat transfer coefficient developed for laminar condensation within a horizontal tube. Under these conditions, the condensing heat transfer coefficient is given by

$$h_{CD} = F\left[\frac{\rho_f \rho_{fg} g_c k_f{}^3 h'_{fg}}{\mu_f (T_{sat} - T_{wall}) D}\right]^{1/4} \tag{6}$$

Values of the leading coefficient (F) are based on the level of void in the tube, i.e. the condensing height, and have been tabulated (Collier, 1972).

There are two differences between the correlations for condensing heat transfer coefficient, and both result in dramatically higher values for the correlation for film condensation on a vertical plate. The first difference is in the leading coefficient and results

in the film condensation coefficient being greater by a factor of 2 to 20, depending on the condensing height. The second difference is that the laminar condensation coefficient has the tube diameter, i.e. the chamber width, in the denominator rather than the condensing height. This results in the film condensation coefficient being greater by a factor ranging from 1.2 to 2.8. The disparity between the two correlations is greatest for small values of the condensing height.

4.4 Fin Analysis

Fins can be used to significantly increase surface area for heat transfer without significantly increasing the effective conduction distance. For certain geometries, addition of fins can greatly improve heat removal capability. Effectiveness of adding fins was investigated to gain additional heat removal margin, particularly for targets designed for higher power cyclotrons. Common fin shapes are rectangular and triangular, as shown in Figure 15.

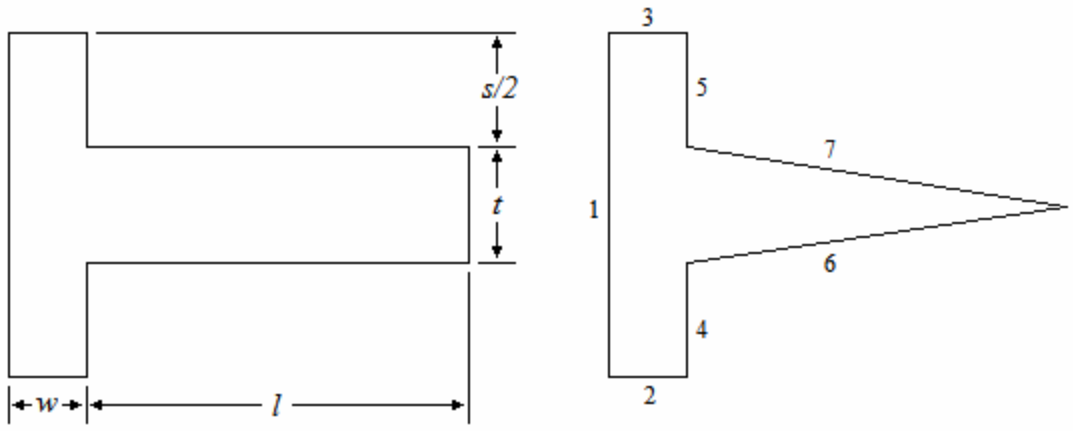

Figure 15: Rectangular and Triangular Fin Dimensions

Additional heat transfer gained by adding fins was calculated using a COMSOL Multiphysics heat transfer model. Both rectangular and triangular fins were investigated for a range of fin lengths (*l*), fin widths (*t*), and fin-to-fin spacings (*s*). All cases considered a wall thickness of 0.02". Addition of fins was examined for the coolant side of the jet, as well as for the inside surface of the target chamber. A representative boiling heat transfer coefficient of 1500 Btu/hr-ft^2-F at 467.01°F, saturation temperature at 500 psi, was selected based on prior modeling results. A representative jetting heat transfer coefficient of 11900 Btu/hr-ft^2-F at 60°F was selected, also based on prior modeling results. The total heat transfer rate per area of the un-finned side was divided by the heat transfer rate achieved with no finning to determine the enhancement in heat transfer rate for each fin condition.

Table 2: Relative Increase in Heat Flux due to Addition of Fins

				Fins on Jet Side		Fins on Boiling Side	
w (in)	s (in)	t (in)	l (in)	Rectangular	Triangular	Rectangular	Triangular
0.020	0.060	0.030	0.125	1.013	1.012	**1.686**	1.605
			0.075	1.012	1.132	1.618	1.518
			0.05	1.012	1.131	1.524	1.410
		0.040	0.125	1.008	1.007	1.672	1.580
			0.075	1.008	1.006	1.587	1.474
			0.05	1.007	1.005	1.486	1.354
		0.050	0.125	1.003	1.002	1.644	1.544
			0.075	1.003	1.002	1.552	1.426
			0.05	1.003	1.001	1.448	1.302
0.020	0.080	0.030	0.125	1.010	1.010	1.566	1.498
			0.075	1.010	1.009	1.510	1.427
			0.05	1.010	1.008	1.433	1.338
		0.040	0.125	1.007	1.006	1.563	1.485
			0.075	1.006	1.005	1.492	1.397
			0.05	1.006	1.005	1.408	1.296
		0.050	0.125	1.002	1.002	1.548	1.462
			0.075	1.002	1.001	1.468	1.361
			0.05	1.002	1.001	1.381	1.255
0.020	0.100	0.030	0.125	1.009	1.008	1.481	1.423
			0.075	1.009	1.008	1.433	1.362
			0.05	1.008	1.007	1.366	1.287
		0.040	0.125	1.006	1.005	1.485	1.417
			0.075	1.005	1.005	1.425	1.341
			0.05	1.005	1.004	1.351	1.255
		0.050	0.125	1.002	1.001	1.477	1.401
			0.075	1.002	1.001	1.406	1.314
			0.05	1.002	1.001	1.331	1.222

Higher heat flux values were achieved by using rectangular fins, as a result of greater surface area when compared to triangular fins of the same length. Placement of fins on the jet coolant side of the system never resulted in improvement in heat transfer greater than 1.3%. Placement of fins on the inside of the target chamber, or boiling side, resulted in increased heat flux of up to 68.6%, due to the relatively low thermal resistance on the jet back.

In general, the highest heat flux is achieved by maximizing the surface area for heat transfer; this is achieved by using rectangular fins, maximizing fin length, and minimizing fin width and spacing. Heat flux is significantly higher when the fins are located on the target chamber side, rather than the jet side, due to the substantially lower heat transfer coefficient.

4.5 Thermal Resistance

A plot of the temperature distribution in a representative thermosyphon target along the axial and radial directions can be used to identify regions of high thermal resistance. In Figures 16 and 17, the temperature drop observed at the interface between the target chamber and the target body is more than six times greater than the temperature drop at the interface between the target body and the coolant system. This behavior is observed for both the jet cooling on the target back and the radial cooling. These figures clearly illustrate that the magnitude of thermal resistance is greatest on the inside of the target chamber, and that reducing this resistance could result in a large improvement in target performance.

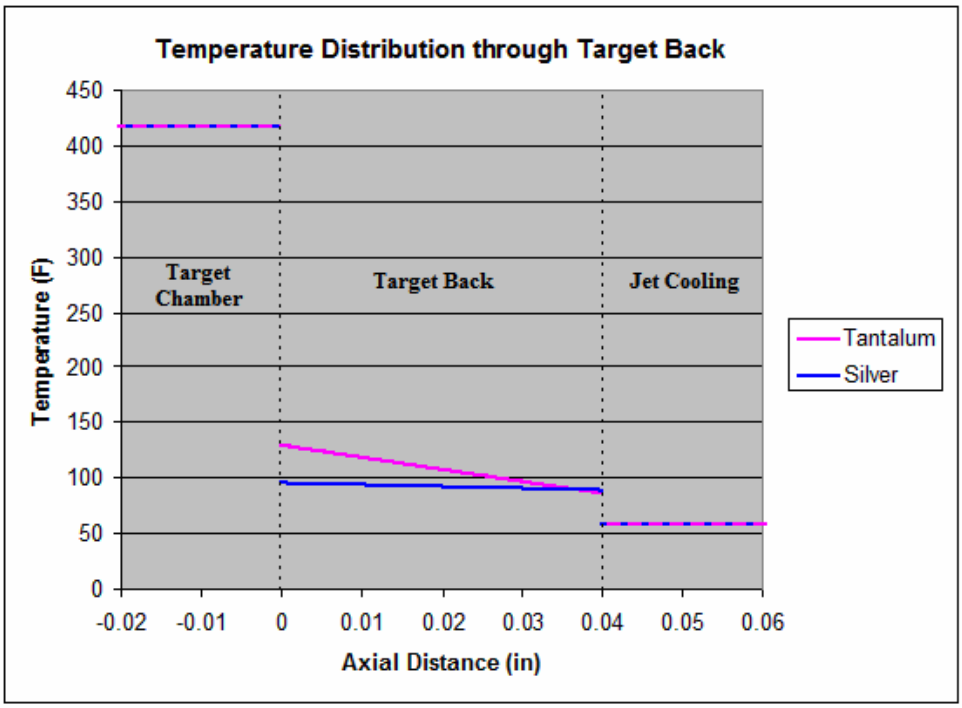

Figure 16: Temperature Distribution in Axial Direction

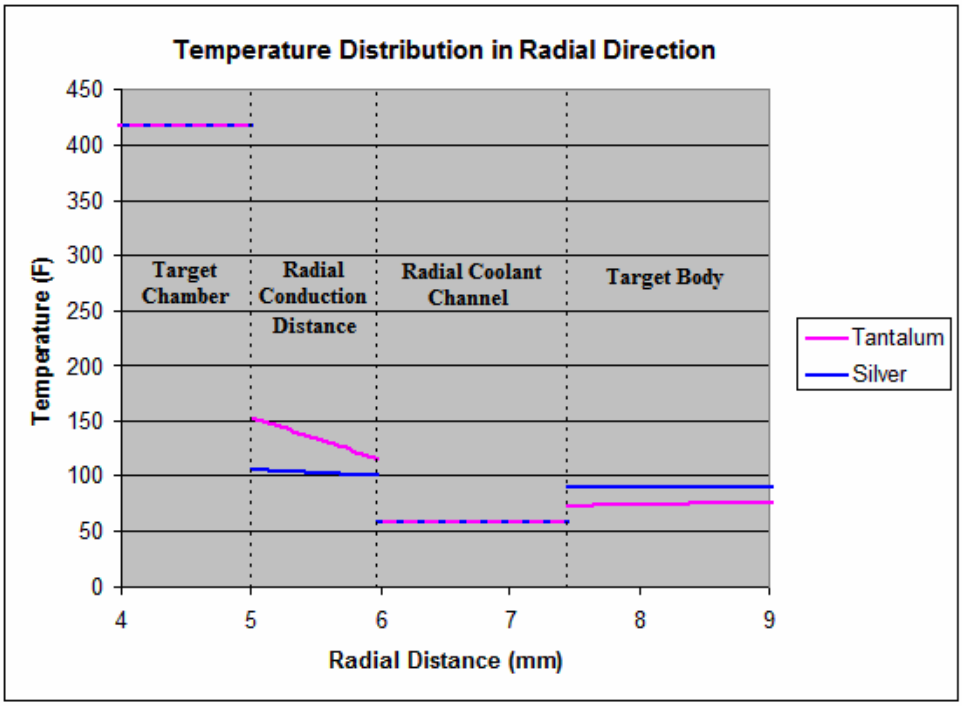

Figure 17: Temperature Distribution in Radial Direction

Chapter 5

Duke University Medical Center Targetry

5.1 Overview

The Duke University Medical Center houses a cyclotron which is used to produce the ^{18}F radioisotope via the $^{18}O(p,n)^{18}F$ reaction for PET imaging. The Duke cyclotron is typically operated below 550W with a maximum capacity of roughly 1000W.

The Duke University Medical Center cyclotron uses batch boiling water targets to produce the ^{18}F. Two target styles are used at the Duke cyclotron, boiling targets originally designed by CTI Cyclotron Systems and thermosyphon boiling targets, developed by Bruce Technologies, Inc. Advances in thermosyphon target design have allowed for production of higher ^{18}F yields in reduced time, while maintaining small target chamber volumes. Modeling and testing of sixth generation thermosyphon targets is investigated in this work.

5.2 Validation of Coolant Mass Flow Rate

Coolant mass flow rate for both the radial and jet cooling systems is needed to predict thermosyphon performance. For evaluation of potential new targets, for which there are no available experimental measurements of mass flow rate, coolant mass flow rates can be estimated using characteristic forms losses. After target construction, the coolant mass flow rates are measured directly during experiments. These measured flow rates are then used in the computer model to predict target performance under the experimental conditions. This allows for direct comparison between predicted performance and experimental observations

which can be used for model validation. In the future, it may be possible to obtain more accurate estimates for coolant mass flow rates using CFD models.

Coolant mass flow rate in both the radial and jet cooling systems was measured as a function of pressure loss for a thermosyphon target with 10 radial coolant channels of diameter 0.136". Coolant flow rates were also predicted using the characteristic forms loss equations over the same range of pressures. The observed flow rate data was used to validate the results of the thermosyphon computer model.

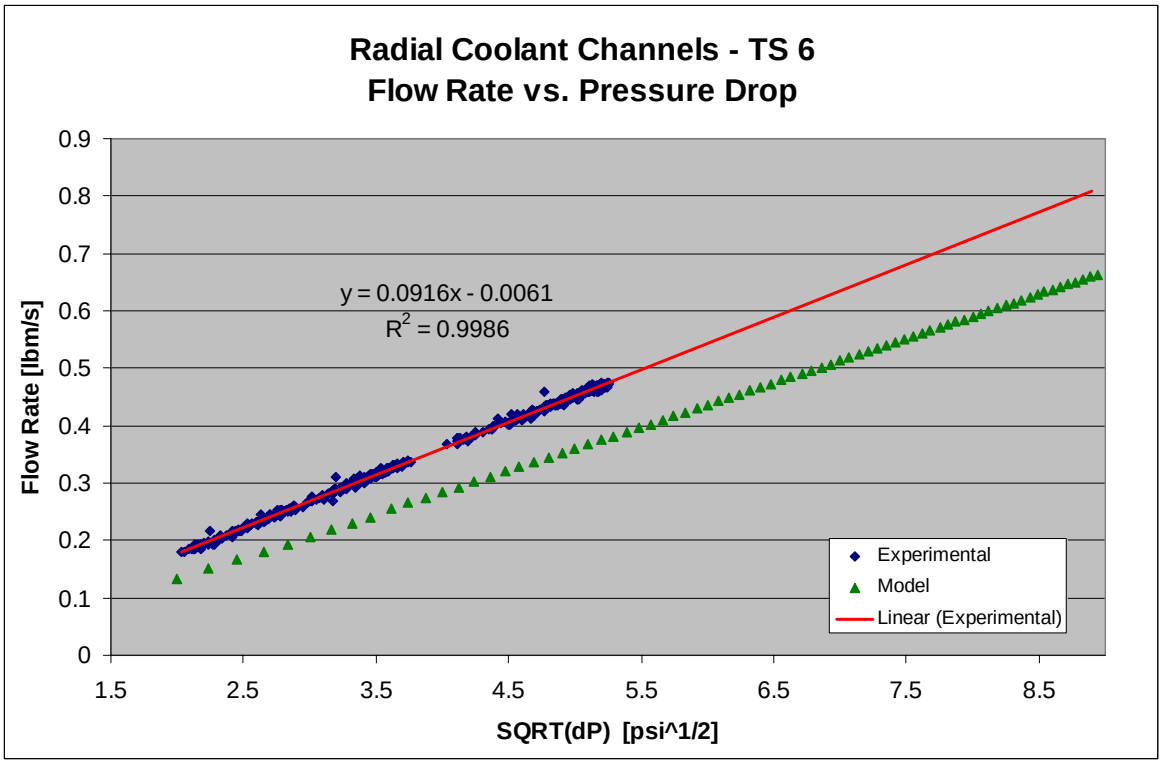

Figure 18: Experimental and Modeled Radial Coolant Flow

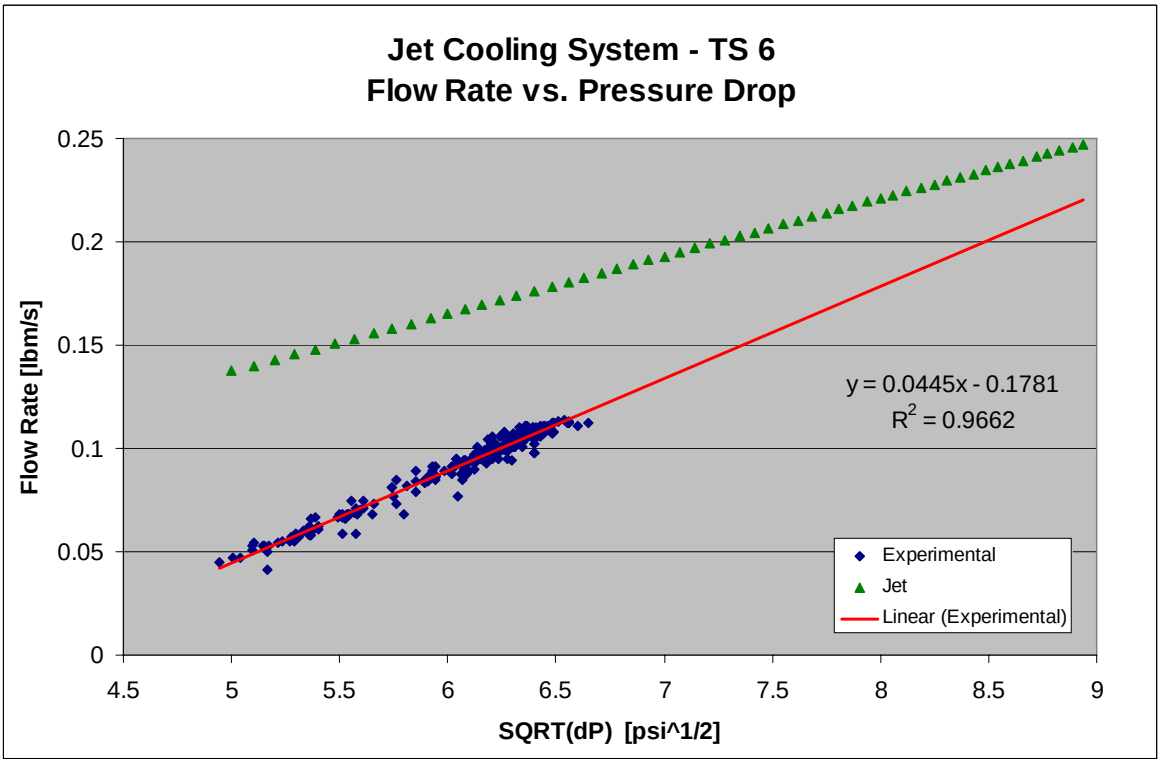

Figure 19: Experimental and Modeled Jet Coolant Flow

Under typical operating conditions, $\Delta P = 71 psi$, the forms loss model under predicts the radial coolant mass flow rate by 18.6% and over estimates the jet coolant mass flow rate by 18.3%. Agreement within 20% is good considering the simplicity of the forms loss model. The target heat capacity was estimated using the model for several boiling conditions for both experimental and model-estimated coolant flow rates.

Table 3: Target Geometry for Coolant Flow Experiment

Height (mm)	Width (mm)	Depth (mm)	Back Thickness (in)	Volume (cc)	# of Channels
15	10	15	0.04	1.93	10

Table 4: Heat Input Predictions for 400 psi Operating Pressure and 2.5cm Condensing Height

Coolant Flow Rate	$\dot{Q}$ (W)	$\dot{m}_{rad}$ (lbm/hr)	$\dot{m}_{jet}$ (lbm/hr)	F_{rad}	F_{jet}	h_{rad} (Btu/hr-ft^2-F)	h_{jet} (Btu/hr-ft^2-F)
Model	1169	2244	838	0.796	0.204	2357	18832
Experimental	1208	2757	709	0.804	0.196	2778	16812
Relative Error	***-3.25%***	*-18.6 %*	*18.3 %*	*-0.98 %*	*4.0 %*	*-15.2 %*	*12.0 %*

Under conditions of distinct boiling and condensing regions in the target chamber, with a condensing height of 2.5cm and operating pressure of 400 psi, the predicted heat input calculated using coolant flow rates determined by the characteristic forms loss technique is less than that calculated using the experimental correlations for the coolant flow rates by 3.25%. Despite errors of roughly 18% in each of the coolant flow rates, model predictions for total heat input are very similar, for these operating conditions. The characteristic forms loss technique, under these conditions, under predicts the thermal performance of the target which is conservative.

Table 5: Heat Input Predictions for 400 psi Operating Pressure for Volume Averaged Boiling Conditions

	Predicted Heat Input : $\dot{Q}$ (W)			
Coolant Flow Rate	$\alpha = 0.05$	$\alpha = 0.075$	$\alpha = 0.1$	$\alpha = 0.125$
Model	701	755	795	827
Experimental	714	770	812	846
Relative Error	*-1.82%*	*-1.95%*	*-2.09%*	*-2.25%*

Under conditions of volume averaged boiling, with low void fraction and operating pressure of 400 psi, the predicted heat input calculated using the coolant flow rates determined by the characteristic forms loss technique is conservative and under predicts the other method by less than 2.25%. These results demonstrate that predicted target performance based on handbook models of coolant mass flow rate give reasonable results.

5.3 Model Evaluation of Potential Target Designs

Four target designs were considered for the Duke cyclotron which featured different radial coolant channel configurations. Each design featured a tantalum target chamber with dimensions of 15mm height, 10mm width, and 15mm depth. Back thicknesses of 0.04" and 0.02" were considered for each design for an operating pressure of 300 psi. Thermal performance was predicted for each target for identical boiling conditions in the target chamber. These predictions were used to evaluate the relative effectiveness of each cooling configuration.

Earlier studies indicate that radial cooling is optimized by closely spaced, small-diameter cooling channels with minimum conduction distance between the channels and the wall of the target chamber (Peeples, 2006). An EDM target design was proposed with a very aggressive radial cooling configuration. Designs featuring staggered and paired coolant channels were also proposed. These designs are less aggressive but allow for simpler manufacture of the piping connections to the exit manifold. The fourth design featured large coolant channels with a single channel per return path to the exit manifold. Designs which feature larger diameter holes at wider spacing can be manufactured more easily at lower cost, so it is important to understand the reduction in target performance associated with using a less optimal cooling configuration.

EDM
30 Channels at 0.040” Diameter

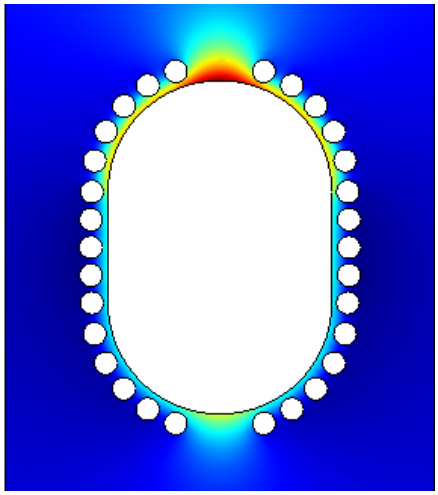

Staggered
30 Channels at 0.040” Diameter

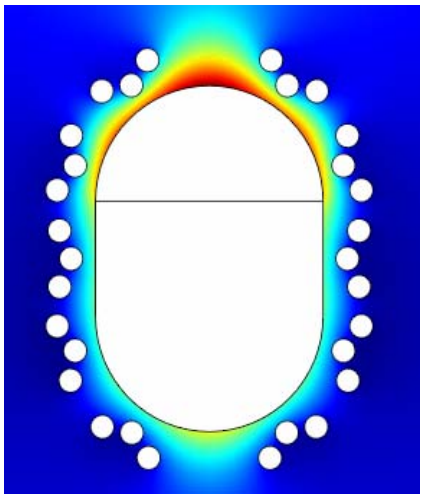

Paired
20 Channels at 0.055” Diameter

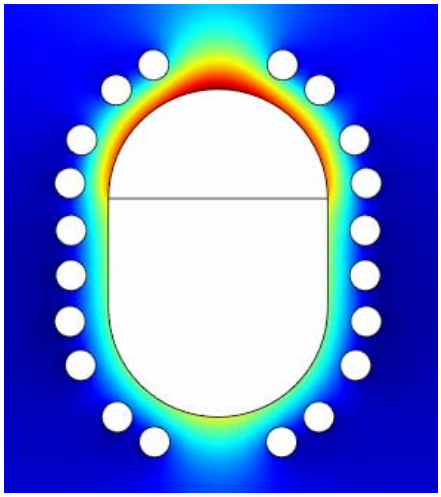

Large Channel
10 Channels at 0.136” Diameter

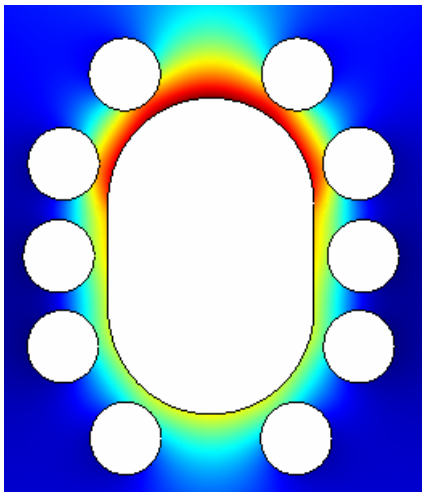

Figure 20: COMSOL Radial Temperature Profiles for Proposed Duke Targets

Table 6: Relative Heat Input for Proposed Duke Targets

H_{CD} (mm)	l_{back} (in)	Design	h_{rad} (Btu/hr-ft^2)	α	Relative Heat Input
5.0	0.02	EDM	7608.3	0.4956	1.40
		Staggered	7608.3	0.4742	1.27
		Paired	6152.1	0.4608	1.20
		Large Channel	2208.5	0.4207	1.00
	0.04	EDM	7608.3	0.4922	1.41
		Staggered	7608.3	0.4703	1.28
		Paired	6152.1	0.4567	1.20
		Large Channel	2208.5	0.4156	1.00
2.5	0.02	EDM	7608.3	0.4205	1.40
		Staggered	7608.3	0.3941	1.27
		Paired	6152.1	0.3791	1.20
		Large Channel	2208.5	0.3361	1.00
	0.04	EDM	7608.3	0.4179	1.41
		Staggered	7608.3	0.3912	1.28
		Paired	6152.1	0.3760	1.20
		Large Channel	2208.5	0.3324	1.00

Relative heat input values were determined for the four designs, using the model, for condensing heights of 5.0 and 2.5 mm. The heat input ratios indicate the relative heat removal capacity of each radial coolant configuration. The large channel design is most easily fabricated, but it has the lowest heat removal capacity of the four designs. Simulations indicated a 20% increase in heat removal capacity for the paired design, a 27% increase in heat removal capacity for the staggered design, and a 40% increase in heat removal capacity for the EDM design. Heat transfer is limited by the conduction distance and coolant flow rate associated with each design. Accordingly, the relative effectiveness of each design should be fairly independent of the assumed boiling conditions in the target chamber.

5.4 Sight Tube Data and Analysis

Both the large channel and paired targets, each with 0.04” back thickness, were constructed. Due to an error at the machine shop, the paired target was constructed with 0.04” diameter coolant channels rather than the 0.055” diameter channels originally modeled.

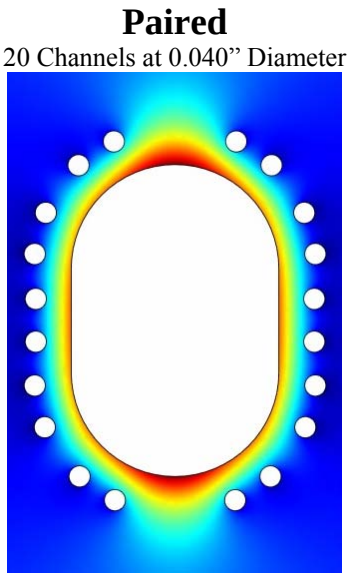

Figure 21: COMSOL Radial Temperature Profile for Paired Target

Experimental data was collected at the Duke University Medical cyclotron for a range of heat input values and operating pressures. Coolant temperature and pressure were recorded at the inlet and outlet of both the radial and jet cooling systems. The mass flow rate in each system was also measured. From these measurements, the partitioning of the heat removal between the radial and jet cooling systems could be estimated. Displaced water volume into the sight tube during operation was observed using a video camera. During operation at constant beam power, or heat input, the displaced water volume in the sight tube oscillates between a minimum and maximum value as a result of pressure oscillations in the

target chamber. The minimum and maximum observed at each heat input was recorded and compared to values predicted using the thermosyphon computer models of each target.

Under normal operating conditions, both targets were able to remove the heat generated by the beam with no indication of beam penetration. Operation of the paired target under normal operating conditions is illustrated in Figure 22.

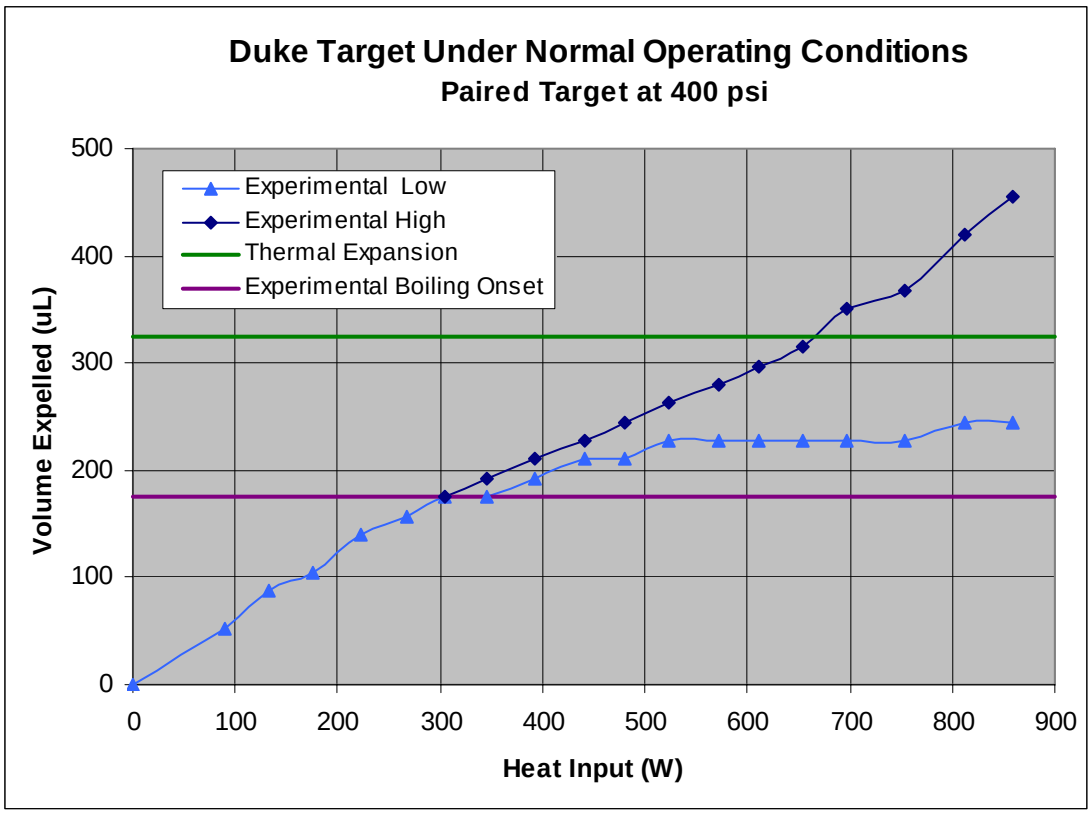

Figure 22: Duke Paired Target under Normal Operating Conditions

In an attempt to observe target operation approaching the target thermal limit, experiments were conducted where valves were used to reduce the coolant flow in both the radial and jet cooling systems. For the large channel target, under conditions of reduced flow, the radial coolant mass flow rate was 0.36 lbm/s and the jet coolant mass flow rate was

0.07 lbm/s. For the paired target, under conditions of reduced flow, the radial coolant mass flow rate was 0.21 lbm/s and the jet coolant mass flow rate was 0.08 lbm/s.

For some operating conditions, it is predicted that the target may operate under volume averaged boiling conditions. Under these conditions, the appropriate thermal limit is predicted to be the heat input that results in average void in the target low enough to allow beam penetration. For 22 MeV protons and 15mm depth, this limit should correspond to an average void fraction of 60%. The measured coolant flow rates were input into the thermosyphon computer model for volume averaged boiling to predict displaced water volume from the target chamber as a function of heat input.

Table 7: Experimental Results for Large Channel Target

Prz (psi)	$\dot{Q}$ (W)	Displaced Low (μL)	Displaced High (μL)	F_{rad}	F_{jet}	Boiling Condition
200	0	0.0				
200	88	70.0		0.87	0.13	
200	132	105.0		0.88	0.12	
200	176	122.5		0.89	0.11	
200	220	157.5	157.5	0.90	0.10	Boiling Onset
200	264	157.5	192.5	0.90	0.10	
200	308	157.5	210.0	0.91	0.09	
200	352	175.0	227.5	0.90	0.10	
200	396	175.0	245.0	0.91	0.09	
200	440	175.0	280.0	0.91	0.09	
200	484	175.0	350.0	0.91	0.09	
200	528	175.0	420.0	0.91	0.09	
200	572	52.5	892.5	0.91	0.09	Classic Penetration
200	616	52.5	962.5	0.91	0.09	Classic Penetration
300	0	0.0				
300	88	52.5		0.88	0.12	
300	132	87.5		0.91	0.09	
300	176	122.5		0.90	0.10	
300	220	157.5	157.5	0.90	0.10	Boiling Onset
300	264	175.0	175.0	0.90	0.10	
300	308	192.5	210.0	0.90	0.10	
300	352	192.5	227.5	0.90	0.10	
300	396	192.5	262.5	0.91	0.09	
300	440	192.5	280.0	0.91	0.09	
300	484	210.0	297.5	0.91	0.09	
300	528	192.5	332.5	0.91	0.09	
300	572	192.5	402.5	0.91	0.09	
300	616	192.5	472.5	0.91	0.09	
300	660	52.5	892.5	0.91	0.09	Classic Penetration

Table 8: Experimental Results for Large Channel Target

Prz (psi)	$\dot{Q}$ (W)	Displaced Low (μL)	Displaced High (μL)	F_{rad}	F_{jet}	Boiling Condition
400	0	0.0				
400	44	17.5		0.86	0.14	
400	88	52.5		0.88	0.12	
400	132	87.5		0.92	0.08	
400	176	122.5		0.89	0.11	
400	220	157.5	157.5	0.91	0.09	Boiling Onset
400	264	175.0	175.0	0.91	0.09	
400	308	192.5	192.5	0.92	0.08	
400	352	192.5	210.0	0.91	0.09	
400	396	210.0	227.5	0.91	0.09	
400	440	210.0	245.0	0.92	0.08	
400	484	210.0	280.0	0.91	0.09	
400	528	227.5	297.5	0.91	0.09	
400	572	227.5	315.0	0.92	0.08	
400	616	227.5	437.5	0.91	0.09	
400	660	192.5	507.5	0.91	0.09	

Table 9: Volume Averaged Boiling Model Predictions for Large Channel Target

Prz (psi)	$\dot{Q}$ (W)	ΔV_{exp} (μL)	α	F_{rad}	F_{jet}
200	174	245.1	0	0.82	0.18
200	475	286.9	0.025	0.80	0.20
200	538	328.6	0.05	0.80	0.20
200	576	370.3	0.075	0.79	0.21
200	604	412.1	0.1	0.79	0.21
200	626	453.8	0.125	0.79	0.21
200	645	495.5	0.15	0.79	0.21
200	661	537.3	0.175	0.79	0.21
200	674	579.0	0.2	0.79	0.21
200	687	620.7	0.225	0.79	0.21
200	698	662.5	0.25	0.79	0.21
200	708	704.2	0.275	0.79	0.21
200	717	745.9	0.3	0.78	0.22
200	725	787.7	0.325	0.78	0.22
200	733	829.4	0.35	0.78	0.22
200	741	871.1	0.375	0.78	0.22
200	748	912.9	0.4	0.78	0.22
200	754	954.6	0.425	0.78	0.22
200	760	996.3	0.45	0.78	0.22
200	766	1038.1	0.475	0.78	0.22
200	772	1079.8	0.5	0.78	0.22

Table 10: Volume Averaged Boiling Model Predictions for Large Channel Target

Prz (psi)	$\dot{Q}$ (W)	ΔV_{exp} (μL)	α	F_{rad}	F_{jet}
300	194	290.5	0	0.82	0.18
300	525	330.9	0.025	0.80	0.20
300	594	371.3	0.05	0.80	0.20
300	637	411.8	0.075	0.79	0.21
300	668	452.2	0.1	0.79	0.21
300	693	492.7	0.125	0.79	0.21
300	713	533.1	0.15	0.79	0.21
300	731	573.6	0.175	0.79	0.21
300	746	614.0	0.2	0.79	0.21
300	760	654.4	0.225	0.79	0.21
300	772	694.9	0.25	0.79	0.21
300	783	735.3	0.275	0.79	0.21
300	793	775.8	0.3	0.79	0.22
300	803	816.2	0.325	0.78	0.22
300	812	856.7	0.35	0.78	0.22
300	820	897.1	0.375	0.78	0.22
300	827	937.5	0.4	0.78	0.22
300	835	978.0	0.425	0.78	0.22
300	842	1018.4	0.45	0.78	0.22
300	848	1058.9	0.475	0.78	0.22
300	854	1099.3	0.5	0.78	0.22
400	210	327.7	0	0.82	0.18
400	563	367.1	0.025	0.80	0.20
400	637	406.4	0.05	0.80	0.20
400	682	445.8	0.075	0.79	0.21
400	716	485.1	0.1	0.79	0.21
400	743	524.5	0.125	0.79	0.21
400	765	563.8	0.15	0.79	0.21
400	784	603.2	0.175	0.79	0.21
400	800	642.5	0.2	0.79	0.21
400	815	681.9	0.225	0.79	0.21
400	828	721.2	0.25	0.79	0.21
400	840	760.6	0.275	0.79	0.21
400	851	799.9	0.3	0.79	0.21
400	861	839.3	0.325	0.78	0.22
400	871	878.6	0.35	0.78	0.22
400	880	918.0	0.375	0.78	0.22
400	888	957.3	0.4	0.78	0.22
400	896	996.7	0.425	0.78	0.22
400	903	1036.0	0.45	0.78	0.22
400	910	1075.4	0.475	0.78	0.22
400	917	1114.7	0.5	0.78	0.22

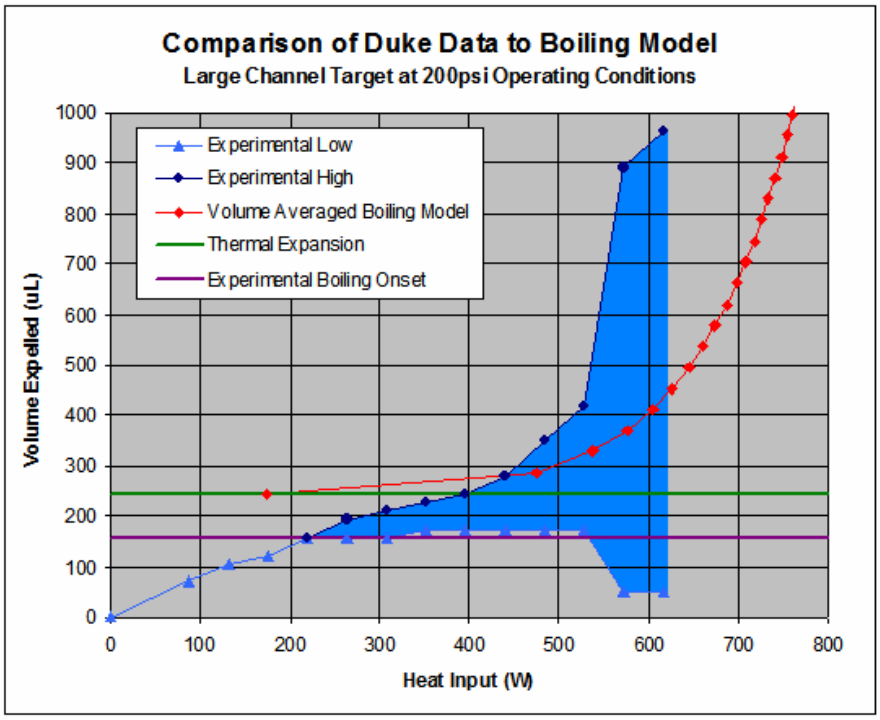

Figure 23: Comparison of Duke Data to Boiling Model for Large Channel Target at 200 psi

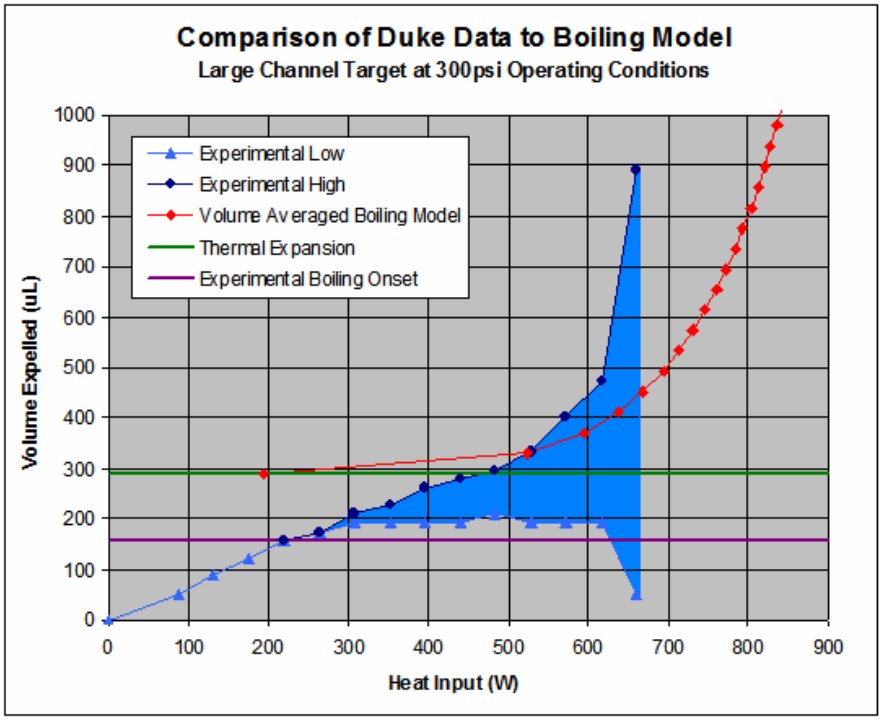

Figure 24: Comparison of Duke Data to Boiling Model for Large Channel Target at 300 psi

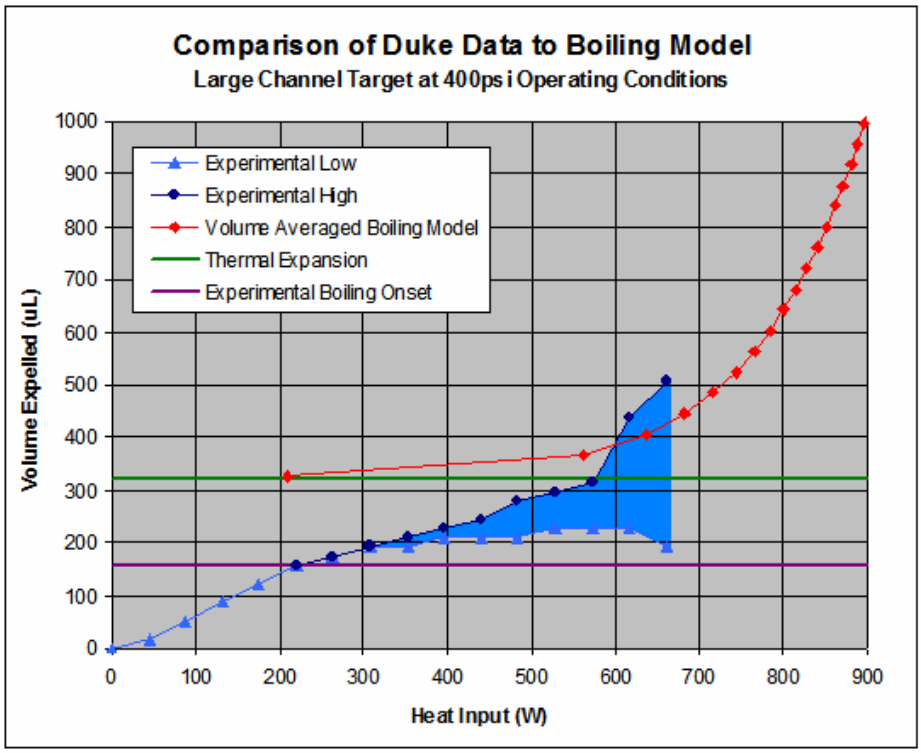

Figure 25: Comparison of Duke Data to Boiling Model for Large Channel Target at 400 psi

Table 11: Experimental Results for Paired Target

Prz (psi)	$\dot{Q}$ (W)	Displaced Low (μL)	Displaced High (μL)	F_{rad}	F_{jet}	Boiling Condition
300	0	0.0				
300	94	70.0		0.83	0.17	
300	129	105.0		0.86	0.14	
300	165	122.5		0.87	0.13	
300	214	140.0		0.88	0.12	
300	261	175.0		0.89	0.11	
300	332	192.5	192.5	0.89	0.11	Boiling Onset
300	366	210.0	210.0	0.89	0.11	
300	394	210.0	245.0	0.88	0.12	
300	445	210.0	262.5	0.89	0.11	
300	471	210.0	280.0	0.89	0.11	
300	518	227.5	297.5	0.90	0.10	
300	583	227.5	315.0	0.89	0.11	
300	666	245.0	385.0	0.90	0.10	
300	706	210.0	385.0	0.90	0.10	
300	754	210.0	455.0	0.90	0.10	
300	794	210.0	805.0	0.89	0.11	
400	0	0.0				
400	89	52.5		0.90	0.10	
400	133	87.5		0.87	0.13	
400	175	105.0		0.87	0.13	
400	222	140.0		0.89	0.11	
400	267	157.5	157.5	0.89	0.11	Boiling Onset
400	304	175.0	175.0	0.89	0.11	
400	346	192.5	210.0	0.90	0.10	
400	393	210.0	227.5	0.90	0.10	
400	441	227.5	262.5	0.89	0.11	
400	480	227.5	280.0	0.89	0.11	
400	523	227.5	280.0	0.89	0.11	
400	573	227.5	315.0	0.89	0.11	
400	611	227.5	315.0	0.90	0.10	
400	654	245.0	332.5	0.90	0.10	
400	697	245.0	350.0	0.89	0.11	
400	754	210.0	490.0	0.90	0.10	
400	813	210.0	595.0	0.90	0.10	
400	858	140.0	945.0	0.89	0.11	Classic Penetration

Table 12: Volume Averaged Boiling Model Predictions for Paired Target

Prz (psi)	$\dot{Q}$ (W)	ΔV (μL)	α	F_{rad}	F_{jet}
300	202	290.5	0	0.83	0.17
300	582	330.9	0.025	0.82	0.18
300	668	371.3	0.05	0.82	0.18
300	722	411.8	0.075	0.82	0.18
300	762	452.2	0.1	0.82	0.18
300	794	492.7	0.125	0.82	0.18
300	820	533.1	0.15	0.82	0.18
300	843	573.6	0.175	0.82	0.18
300	864	614.0	0.2	0.81	0.19
300	882	654.4	0.225	0.81	0.19
300	898	694.9	0.25	0.81	0.19
300	913	735.3	0.275	0.81	0.19
300	927	775.8	0.3	0.81	0.19
300	940	816.2	0.325	0.81	0.19
300	952	856.7	0.35	0.81	0.19
300	963	897.1	0.375	0.81	0.19
300	974	937.5	0.4	0.81	0.19
300	984	978.0	0.425	0.81	0.19
300	993	1018.4	0.45	0.81	0.19
300	1002	1058.9	0.475	0.81	0.19
300	1011	1099.3	0.5	0.81	0.19
400	218	327.7	0	0.83	0.17
400	624	367.1	0.025	0.82	0.18
400	715	406.4	0.05	0.82	0.18
400	773	445.8	0.075	0.82	0.18
400	816	485.1	0.1	0.82	0.18
400	850	524.5	0.125	0.82	0.18
400	879	563.8	0.15	0.82	0.18
400	904	603.2	0.175	0.82	0.18
400	926	642.5	0.2	0.82	0.19
400	945	681.9	0.225	0.81	0.19
400	963	721.2	0.25	0.81	0.19
400	979	760.6	0.275	0.81	0.19
400	994	799.9	0.3	0.81	0.19
400	1008	839.3	0.325	0.81	0.19
400	1020	878.6	0.35	0.81	0.19
400	1033	918.0	0.375	0.81	0.19
400	1044	957.3	0.4	0.81	0.19
400	1055	996.7	0.425	0.81	0.19
400	1065	1036.0	0.45	0.81	0.19
400	1074	1075.4	0.475	0.81	0.19
400	1084	1114.7	0.5	0.81	0.19

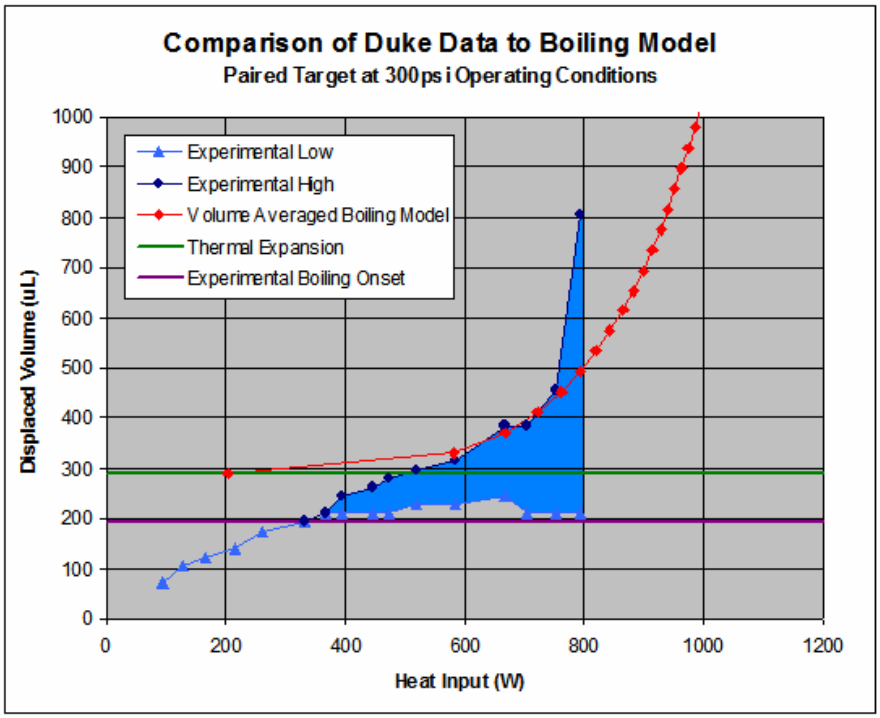

Figure 26: Comparison of Duke Data to Boiling Model for Paired Target at 300 psi

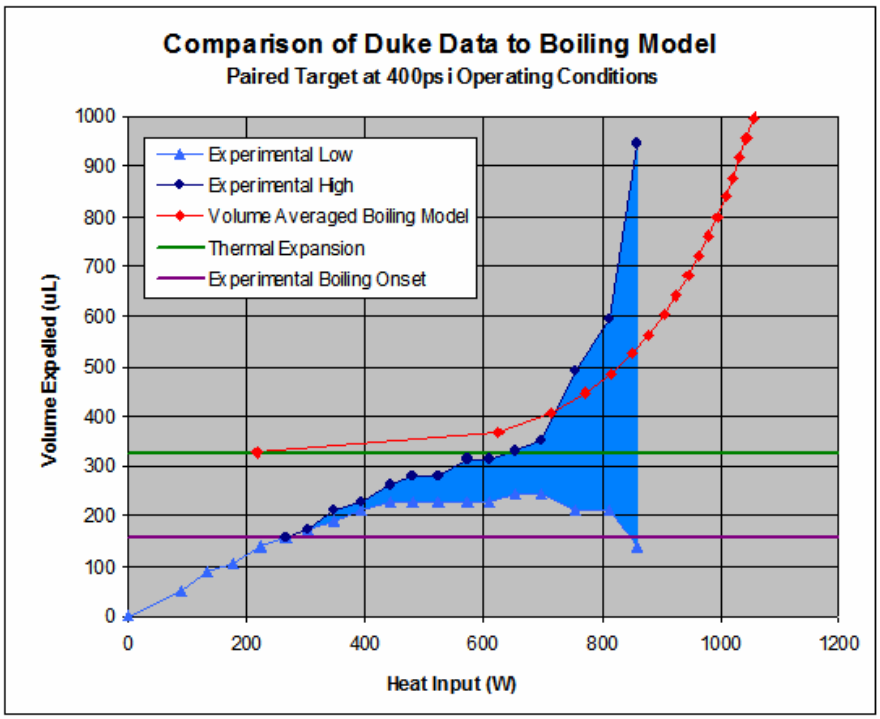

Figure 27: Comparison of Duke Data to Boiling Model for Paired Target at 400 psi

Boiling onset can be estimated from the experimental data by observing when oscillations initiate in the displaced water volume in the sight tube. For both targets, experimental boiling onset occurs at lower volume displacement than is predicted for the thermal expansion process. This suggests that subcooled boiling may be occurring in the target for average target chamber temperatures below the saturation temperature. The volume averaged boiling model cannot predict subcooled boiling, but assumes that volume averaged boiling initiates in the target following the thermal expansion period. Accordingly, there are discrepancies between the model predictions and experimental data at very low values of average void. When the displaced volume exceeds the predicted thermal expansion level, there is a distinct increase in the slope of the displacement level with respect to heat input for all cases. This suggests that the target chamber volume is saturated at this displacement, as the model predicts.

For average void fraction values as low as 2.5 to 5%, the displaced volume predicted by the model passes within the band of displacement observed experimentally. This agreement continues for the duration of the experimental data, corresponding to average void fractions up to 12.5%. Agreement between the model predictions and observed data for displaced water volume as a function of heat input suggests that target boiling conditions resemble volume averaged boiling, and that there is no formation of a distinct condensing region during target operation.

Classic oscillation behavior that suggests beam penetration is observed for the large channel target under 200 and 300 psi operating conditions and for the paired target under 400 psi operating conditions. The corresponding average void fractions predicted by the model under these conditions are well below the expected limiting value of 60%; however, it is the

maximum displacement that should be considered to determine the thermally limiting conditions. Comparison of the chamber conditions at maximum and minimum water displacement can be used to assess the swing in boiling dynamics that occurs under operating and thermally limiting conditions.

Table 13: Observed Thermal Limit for Duke Targets

Target Design	Prz (psi)	$\dot{Q}$ (W)	Maximum Void (%)	Model Average Void (%)	Minimum Level Condition
Large Channel	200	572	38.7	7.2	Subcooled
Large Channel	300	660	37.2	9.3	Subcooled
Paired	400	858	39.2	13.2	Subcooled

The void fraction corresponding to the maximum displacement occurring at the onset of beam penetration is the observed thermal limit for a target operating under these conditions. For the large channel and paired targets the observed thermal limit is between 38.7 and 39.2% average void in the target chamber. This is significantly below the theoretical value of roughly 60%, which suggests that the distribution of void is not uniform in the chamber. The minimum displacement level under penetrating conditions is below the thermal expansion level, which indicates that the bulk temperature of the fluid is below saturation. This further suggests that the void is not uniformly distributed, with a higher concentration of void forming in the path of the beam. The model does a reasonable job of predicting the average displacement level corresponding to the heat input at which beam penetration is observed. The average target void predicted by the model under conditions of beam penetration is between 7.2 and 13.2% for the two targets. As predicted by the model, the paired target is shown to have a higher heat removal capacity than the large channel target.

5.5 Target Yield under Normal Operating Conditions

The paired target, or TS-6, was selected to be a new production target at the Duke facility. The target was operated at power levels consistent with normal operation and yield tests were performed to confirm successful target operation and the absence of beam penetration. The first set of yield tests were performed using a mixture of natural abundance water and ethanol. Proton bombardment of natural abundance water produces Nitrogen-13 through the $^{16}O(p,\alpha)^{13}N$ reaction. The measured activity of recovered ^{13}N can be compared to the theoretical yield to determine if beam penetration has occurred. Yields close to the theoretical saturation yield indicate successful target operation and the absence of beam penetration.

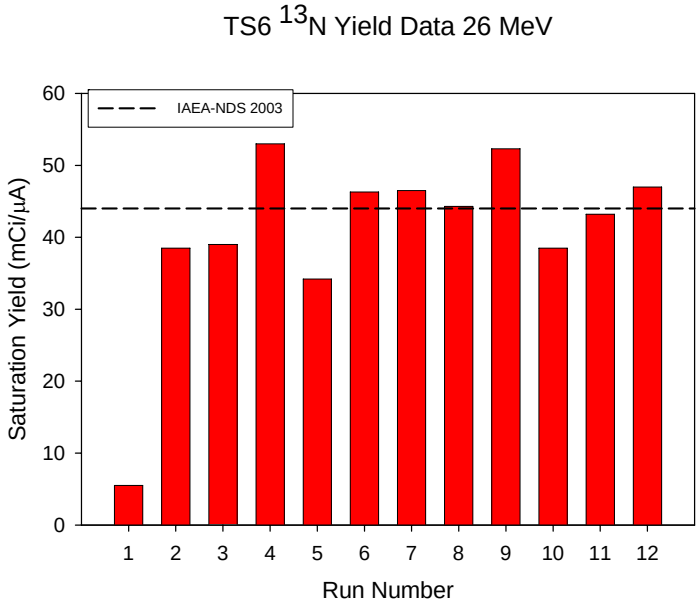

Figure 28: Nitrogen-13 Yield Data (Matthew Stokely 2007)

The first run typically produces low ^{13}N yield, as shown in Figure 28. Eleven additional runs all resulted in ^{13}N yield sufficiently close to the theoretical saturation yield to indicate successful operation without beam penetration.

Additional tests were performed using enriched water, and the measured yield of ^{18}F was compared to the theoretical value. This is consistent with normal operation under production conditions.

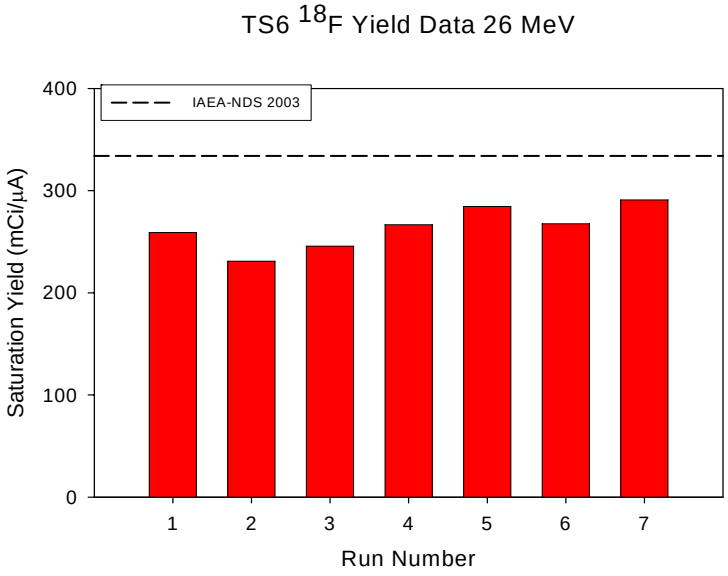

Figure 29: Flourine-18 Yield Data (Matthew Stokely 2007)

Although it is impossible to recover all of the ^{18}F without a target rinse, the measured ^{18}F yield from seven runs were all sufficiently close to the theoretical saturation yield to indicate successful operation without beam penetration.

Additional qualifying tests have been performed which indicate good FDG yields from the TS-6 target (Stokely, 2008). The use of Tantalum target internals and the advanced cooling capabilities of the TS-6 have resulted in more than a factor of 2 improvement in fluoride production capability at the Duke PET facility.

Chapter 6

Wisconsin Medical Cyclotron Targetry

6.1 Overview

The Wisconsin Medical Cyclotron is also used to produce ^{18}F via the $^{18}O(p,n)^{18}F$ reaction, using batch boiling targets. GE boiling targets with back cooling are currently used for production runs at the cyclotron. The Wisconsin Medical Cyclotron has the potential to operate at beam power as high as 2.4 kW. This would far exceed the heat removal capabilities of the GE targets, which can remove roughly 1 kW of heat. For production runs, beam power as high as 1.6 kW is feasible. Thermosyphon targets are capable of operation at such high beam power, while maintaining reasonable target chamber volume. High power thermosyphon targets have been designed using the thermosyphon computer models and tested at the Wisconsin Medical Cyclotron.

6.2 Material Comparison

Tantalum has been demonstrated to have excellent chemical compatibility for the FDG synthesis process, although it suffers from relatively low thermal conductivity, high cost, and is difficult to machine. Silver has been used for target chambers historically due to its high thermal conductivity and reasonable chemical compatibility. Silver is a more attractive material for experimental test work because it is less expensive than tantalum and can be machined more easily and quickly. The reduction in heat removal capacity, as a result

of reduced thermal conductivity, that occurs when replacing a silver target with an identical tantalum target can be estimated using the thermosyphon computer models.

A thermosyphon target with 22.5mm chamber height, 15mm chamber width, 15mm chamber depth, and corresponding chamber volume of 4.3 mL was modeled in both silver and tantalum. This target featured a paired radial coolant channel design with 28 radial channels of 0.055" diameter and a back thickness of 0.04". The predicted heat removal capacity corresponding to a boiling height of 15mm was used to evaluate the penalty for using tantalum.

Table 14: Heat Removal Predictions for Silver and Tantalum Targets at 400 psi

Material	H_B (mm)	α	F_{rad}	F_{jet}	Relative Heat Input
Silver	15.0	0.4502	0.78	0.22	1.00
Tantalum	15.0	0.4045	0.74	0.26	0.83

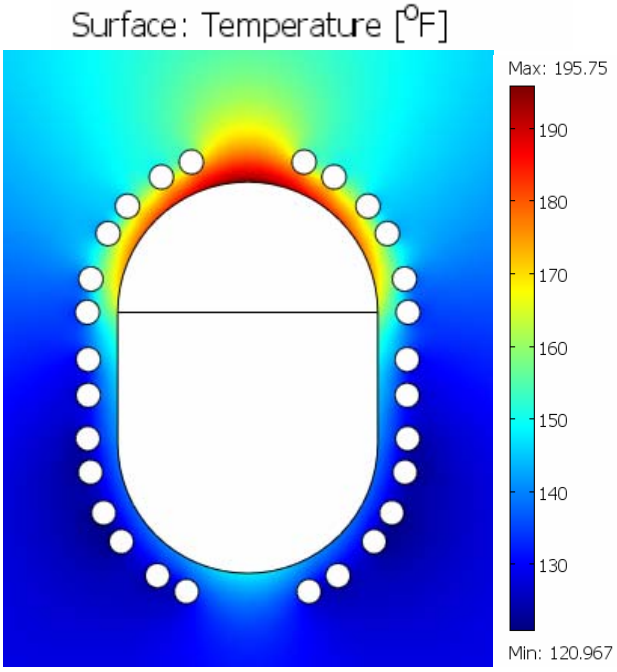

Figure 30: COMSOL Radial Temperature Profile for Silver Target at 400 psi

This simulation indicates a 17% penalty in heat removal capacity for a tantalum target when compared to an identical silver target.

6.3 Model Evaluation of Potential Target Designs

Three target designs were proposed for testing at the Wisconsin Medical Cyclotron which featured different radial coolant channel configurations. Each design featured a silver target with 22.5mm chamber height, 15mm chamber width, 15mm chamber depth, and 0.04" back thickness. The heat input to reduce liquid level in the target to 15mm boiling height was predicted for each target, under the assumption of distinct boiling and condensing regions in the target chamber, and was used to assess the relative heat removal capacity of each design.

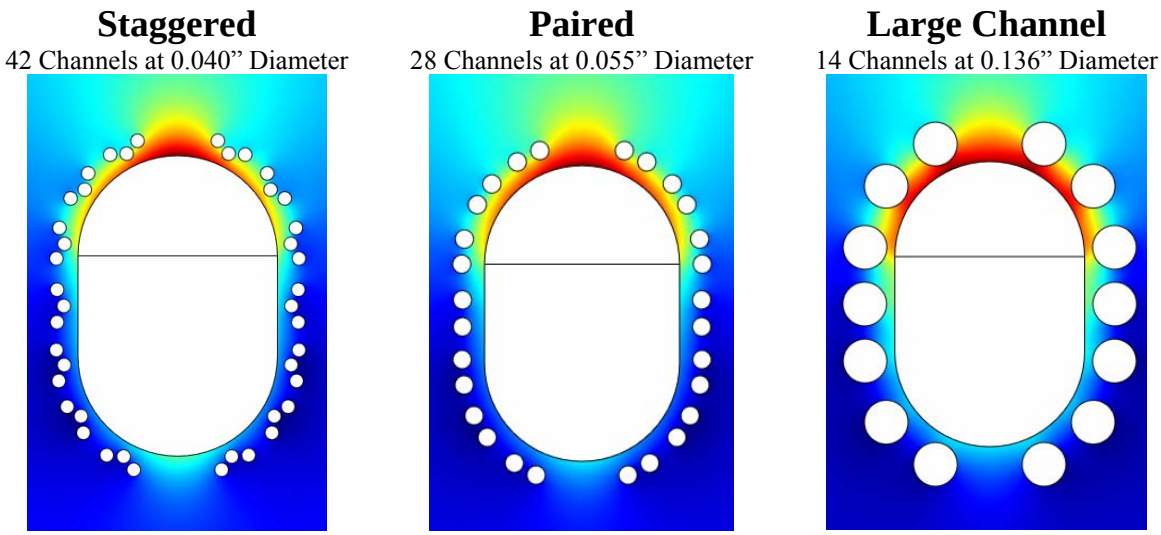

Figure 31: COMSOL Radial Temperature Profiles for Proposed Wisconsin Silver Targets

Table 15: Relative Heat Input for Proposed Wisconsin Silver Targets

Design	H_B (mm)	l_{back} (in)	h_{rad} (Btu/hr-ft^2)	α	Relative Heat Input
Staggered	15.0	0.04	6060	0.4557	1.26
Paired	15.0	0.04	4824	0.4502	1.23
Large Channel	15.0	0.04	1692	0.4082	1.00

Relative heat input values were determined for the three designs under 400 psi operating conditions for a boiling height of 15.0 mm. As indicated by prior tests, the large channel design has the lowest heat removal capacity of the three designs. Simulations indicated a 23% increase in heat removal capacity for the paired design and a 26% increase in heat removal capacity for the staggered design. No EDM design was considered for this testing, because quick target construction time was a primary goal.

6.4 Sight Tube Data and Analysis for Silver Test Target

The silver target with paired radial coolant channels was constructed for testing at the Wisconsin Medical Cyclotron. Experimental data was collected for a range of heat input values at an operating pressure of 400psi. Coolant mass flow rate was measured in both the radial coolant channels and the jet cooling system. The radial coolant mass flow rate was 0.255 lbm/s, and the jet coolant mass flow rate was 0.338 lbm/s. These flow rates were lower than expected due to non-ideal connections to the pressure manifolds. Displaced water volume into the sight tube during operation over a range of heat inputs was observed using a video camera. The minimum and maximum displacement observed during operation at each heat input was recorded and compared to values predicted using the thermosyphon computer models.

Table 16: Experimental Results for Paired Silver Target at 400 psi (Matthew Stokely 2007)

$\dot{Q}$ (W)	I (μA)	Displaced Low (μL)	Displaced High (μL)
80	5	59.4	59.4
160	10	118.8	118.8
240	15	178.2	178.2
320	20	237.6	237.6
400	25	297.0	297.0
480	30	356.4	356.4
560	35	415.8	475.2
640	40	475.2	534.6
720	45	475.2	534.6
800	50	475.2	594.0
960	60	534.6	653.4
1120	70	653.4	772.1
1280	80	712.8	1187.9
1440	90	950.3	1900.7
1600	100	1306.7	2494.6
1760	110	1663.1	3088.6
1760	110	1722.5	3029.2
1920	120	2197.6	3207.4
2000	125	2375.8	3266.8

The cyclotron beam was re-tuned after reaching a beam current of 110 μA. The sight tube level was recorded before and after the re-tuning. Observations at 120 and 125 μA were recorded after the re-tuning.

Table 17: Volume Averaged Boiling Model Predictions for Paired Silver Target at 400 psi

$\dot{Q}$ (W)	I (μA)	ΔV_{exp} (μL)	α
368	23.0	737.4	0
997	62.3	844.1	0.025
1154	72.1	950.7	0.05
1255	78.4	1057.4	0.075
1330	83.1	1164.1	0.1
1391	86.9	1270.8	0.125
1443	90.2	1377.4	0.15
1487	92.9	1484.1	0.175
1527	95.4	1590.8	0.2
1562	97.6	1697.4	0.225
1594	99.6	1804.1	0.25
1624	101.5	1910.8	0.275
1651	103.2	2017.5	0.3
1676	104.8	2124.1	0.325
1700	106.3	2230.8	0.35
1722	107.6	2337.5	0.375
1743	108.9	2444.1	0.4
1763	110.2	2550.8	0.425
1782	111.4	2657.5	0.45
1800	112.5	2764.1	0.475
1817	113.6	2870.8	0.5
1833	114.6	2977.5	0.525
1849	115.6	3084.2	0.55
1864	116.5	3190.8	0.575
1879	117.4	3297.5	0.6
1893	118.3	3404.2	0.625
1906	119.1	3510.8	0.65
1919	119.9	3617.5	0.675
1932	120.8	3724.2	0.7
1944	121.5	3830.9	0.725
1956	122.3	3937.5	0.75
1967	122.9	4044.2	0.775
1979	123.7	4150.9	0.8
1990	124.4	4257.5	0.825
2000	125.0	4364.2	0.85
2011	125.7	4470.9	0.875
2021	126.3	4577.6	0.9

Table 18: Vertical Plate Condensation Model Predictions for Paired Silver Target at 400 psi

H_{CD} (mm)	$\dot{Q}$ (W)	I (μA)	ΔV_{exp} (μL)	α
0.5	1642	102.6	1361	0.1709
1	1710	106.9	1496	0.2003
1.5	1755	109.7	1609	0.2215
2	1789	111.8	1713	0.2387
2.5	1817	113.6	1813	0.2536
3	1840	115.0	1907	0.2666
3.5	1861	116.3	2001	0.2786
4	1879	117.4	2092	0.2895
4.5	1895	118.4	2182	0.3000
5	1909	119.3	2270	0.3095
5.5	1923	120.2	2356	0.3187
6	1935	120.9	2441	0.3275
6.5	1945	121.6	2524	0.3358
7	1955	122.2	2604	0.3437
7.5	1964	122.8	2683	0.3512

Table 19: Horizontal Tube Condensation Model Predictions for Paired Silver Target at 400 psi

H_{CD} (mm)	$\dot{Q}$ (W)	I (μA)	ΔV_{exp} (μL)	α
0.5	1202	75.1	968	0.0591
1	1286	80.4	1087	0.0827
1.5	1337	83.6	1197	0.1011
2	1374	85.9	1303	0.1168
2.5	1403	87.7	1407	0.1309
3	1427	89.2	1511	0.1440
3.5	1447	90.4	1614	0.1561
4	1465	91.6	1717	0.1676
4.5	1480	92.5	1818	0.1785
5	1493	93.3	1919	0.1889
5.5	1504	94.0	2018	0.1989
6	1514	94.6	2115	0.2084
6.5	1522	95.1	2211	0.2176
7	1529	95.6	2306	0.2266
7.5	1536	96.0	2398	0.2354

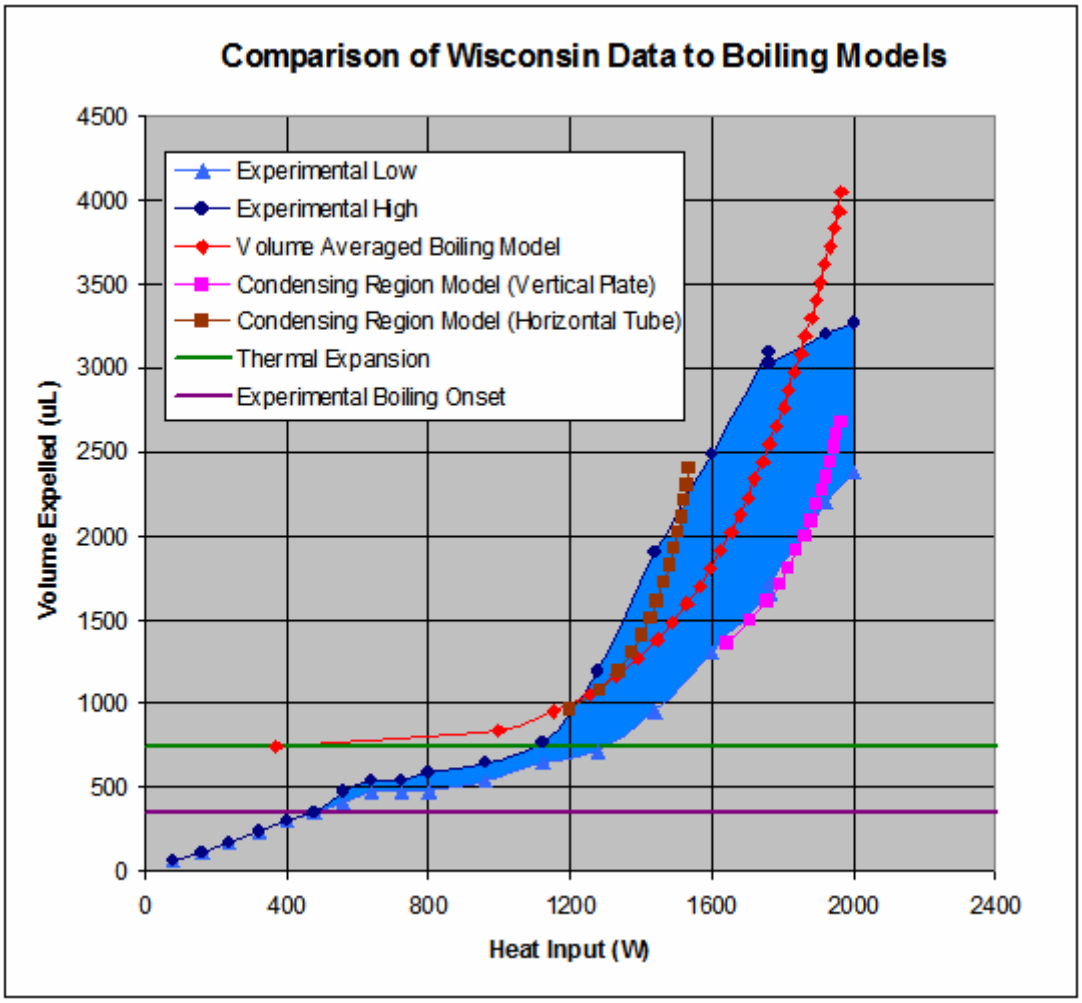

Figure 32: Comparison of Wisconsin Data to Boiling Models for Paired Silver Target at 400 psi

As with the Duke sight tube data, oscillations were observed in the displaced water volume at displacements less than that predicted for thermal expansion. This behavior, which suggests that subcooled boiling is occurring in the target, cannot be captured by the thermosyphon computer models. For heat inputs between 1280W and 1760W, the displaced volume predicted by the volume averaged boiling model passes within the band of displacement observed experimentally. This region corresponds to average void fractions between 7.5 and 42.5%. The classic two-region model was also used to predict target

performance, using both the film condensation on a vertical plate (Vertical Plate) and laminar condensation within a horizontal tube (Horizontal Tube) correlations for the condensing heat transfer coefficient. Neither version of the two-region model was able to adequately describe the boiling conditions observed over the range of experimental data.

For heat input above 1760W, there is a pronounced difference in the slope of the observed upper displacement level, and agreement between the data and the volume averaged boiling model breaks down. As with the Duke data, there is a distinct increase in the slope of the volume displacement with respect to heat input observed for displacements above the predicted thermal expansion level, suggesting that the target has reached saturation conditions.

The distinct change in slope in the upper displacement level observed for heat inputs above 1760W is most likely a result of the onset of beam penetration. Beam penetration would result in some heat being deposited in the back wall of the target. This would effectively cause the upper displacement to level off, as any additional increases in the beam would be deposited in the back wall. Yield data could not be collected for this target in the region where beam penetration appears evident; however, limited yield data was collected from another target which supports the conclusion that some beam penetration may be responsible for the change in the observed sight tube behavior.

6.5 Sight Tube Data Analysis for Modified Silver Test Target

A second silver target was fabricated and tested at the Wisconsin Medical Cyclotron. This target featured reduced target chamber dimensions and serial connection between the jet and radial cooling systems. The second target had a modified target back which resulted in water jetting through a slit onto a series of finned channels on the target back before entering the radial coolant channels. The modified design reduced conduction distance through the back of the target, but it resulted in strong non-uniformity in the flow through the radial coolant channels. The modified test target featured a silver target chamber with dimensions of 20.25mm height, 13.5mm width, and 13.5mm depth and 28 radial coolant channels of 0.055" diameter. Sight tube data at 250 and 400 psi was collected over a range of heat input values.

No appropriate jetting heat transfer coefficient for the modified back was available in the literature, so the thermosyphon computer models could not be used directly to predict target performance. However, information about boiling conditions in the target and the target thermal limit could still be inferred from the sight tube and yield data collected.

Table 20: Experimental Results for Modified Silver Test Target at 250psi (Matthew Stokely 2007)

$\dot{Q}$ (W)	I (μA)	Displaced Low (μL)	Displaced High (μL)
0	0	0.0	
800	50	395.2	642.2
1200	75	963.3	1580.8
1360	85	1210.3	2000.7
1440	90	1383.2	2074.8
1520	95	1556.1	2124.2
1600	100	1753.7	2198.3
800	50	345.8	494.0
1600	100	1753.7	2247.7
1680	105	1951.3	2247.7
1760	110	2000.7	2247.7
1920	120	2050.1	2272.4
1920	120	2050.1	2297.1
2000	125	2099.5	2272.4
2080	130	2148.9	2297.1
2160	135	2198.3	2346.5
2240	140	2247.7	2395.9
2320	145	2247.7	2395.9

The sight tube data under 250 psi operating conditions was collected over two days.

Table 21: Experimental Results for Modified Silver Test Target at 400psi (Matthew Stokely 2007)

$\dot{Q}$ (W)	I (μA)	Displaced Low (μL)	Displaced High (μL)
0	0	0.0	
160	10	98.8	
320	20	222.3	
432	27	296.4	
480	30	271.7	321.1
640	40	345.8	395.2
800	50	370.5	419.9
960	60	444.6	518.7
1120	70	419.9	1136.2
1200	75	494.0	1358.5
1280	80	494.0	1580.8
1360	85	642.2	1778.4
1440	90	741.0	2025.4
1520	95	1037.4	2148.9
1600	100	1284.4	2272.4
1680	105	1407.9	2346.5
1760	110	1531.4	2346.5
1840	115	1729.0	2395.9
1920	120	1901.9	2395.9

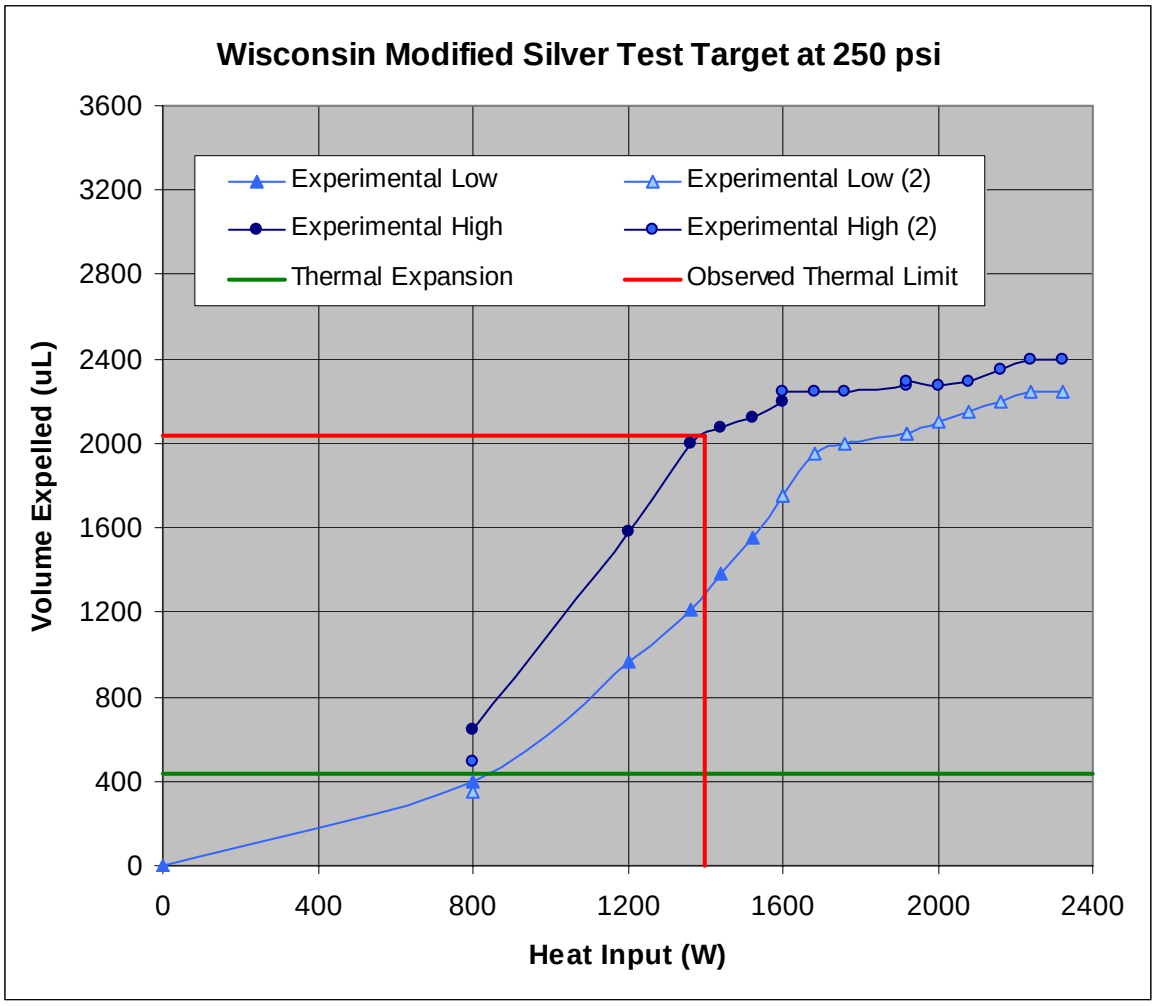

Figure 33: Wisconsin Modified Silver Test Target at 250 psi

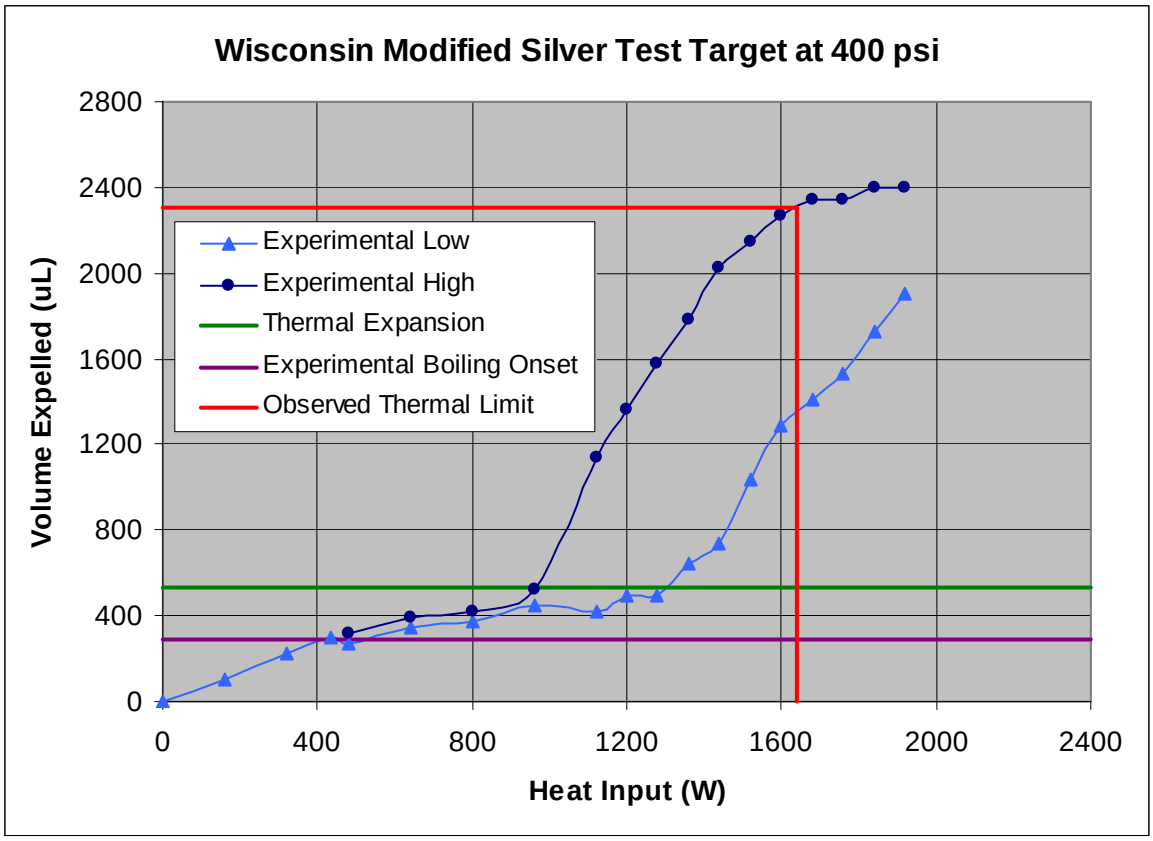

Figure 34: Wisconsin Modified Silver Test Target at 400 psi

The general behavior of the sight tube data observed for the modified silver test target under 250 and 400 psi operating conditions is consistent with the observations from the larger silver target. Under 400 psi operating conditions, the modified silver test target has observed oscillation behavior consistent with subcooled boiling. There is also a distinct increase in the slope of the volume displacement with respect to heat input observed for displacements above the predicted thermal expansion level, consistent with reaching saturation conditions.

Under 250 psi operating conditions, there is a pronounced difference in the slope of the observed upper displacement level for heat input above 1400W. A similar change in the slope of the upper displacement level is observed under 400 psi operating conditions for heat

input above 1640 W. The change in slope of the upper displacement level is most likely a result of the onset of beam penetration, as additional increases in the beam above the thermal limit would be deposited in the back wall.

6.6 Sight Tube and Yield Data Analysis for Modified Tantalum Target

A third target was built and tested at the Wisconsin facility. The new target was geometrically identical to the modified silver test target but featured tantalum internals. Sight tube data and yield data using both natural abundance and enriched water was collected under 250 psi operating conditions. Limited sight tube data was collected under 400 psi operating conditions before rupture of the target window foil resulted in target failure. The sight tube data that was successfully collected at 400 psi was insufficient to provide meaningful sight tube analysis.

Table 22: Experimental Results for Modified Tantalum Target at 250psi (Matthew Stokely 2007)

$\dot{Q}$ (W)	I (μA)	Displaced Low (μL)	Displaced High (μL)
0	0	0.0	
160	10	118.8	
320	20	213.8	
480	30	308.9	332.6
640	40	332.6	380.1
640	40	356.4	427.6
800	50	403.9	641.5
960	60	641.5	1069.1
1120	70	879.1	1639.3
1280	80	1211.7	2043.2
1280	80	1235.4	2114.5
1440	90	1591.8	2304.6
1600	100	1805.6	2470.9
1680	105	1948.2	2494.6
1760	110	2067.0	2518.4
1840	115	2114.5	2518.4
1920	120	2185.8	2565.9
2000	125	2304.6	2589.7
2080	130	2304.6	2565.9
2160	135	2352.1	2589.7

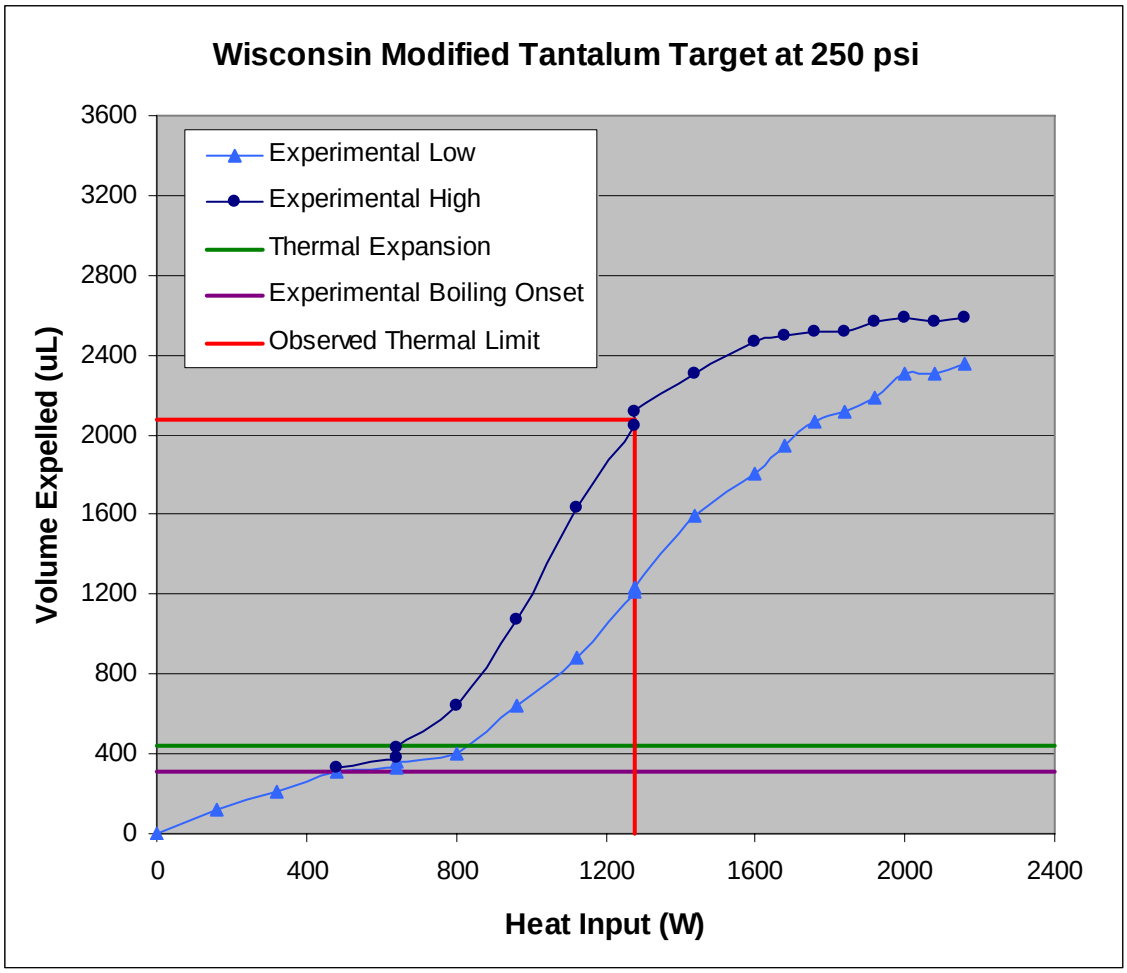

Figure 35: Wisconsin Modified Tantalum Target at 250 psi

The general behavior of the sight tube data observed for the modified tantalum target is consistent with observations from other Wisconsin targets. Oscillations initiate below the thermal expansion level, consistent with subcooled boiling. Once again, there is a distinct increase in the slope of the volume displacement with respect to heat input observed for displacements above the predicted thermal expansion level, consistent with reaching saturation conditions. A pronounced difference in the slope of the upper displacement level is observed for heat input above 1280W, most likely due to the onset of beam penetration.

Yield data was collected for the modified tantalum target using both natural abundance and enriched water over a period of six days. All of the yield tests were performed under 250 psi operating conditions, and the combined yield results for each set of tests are presented as a function of beam power.

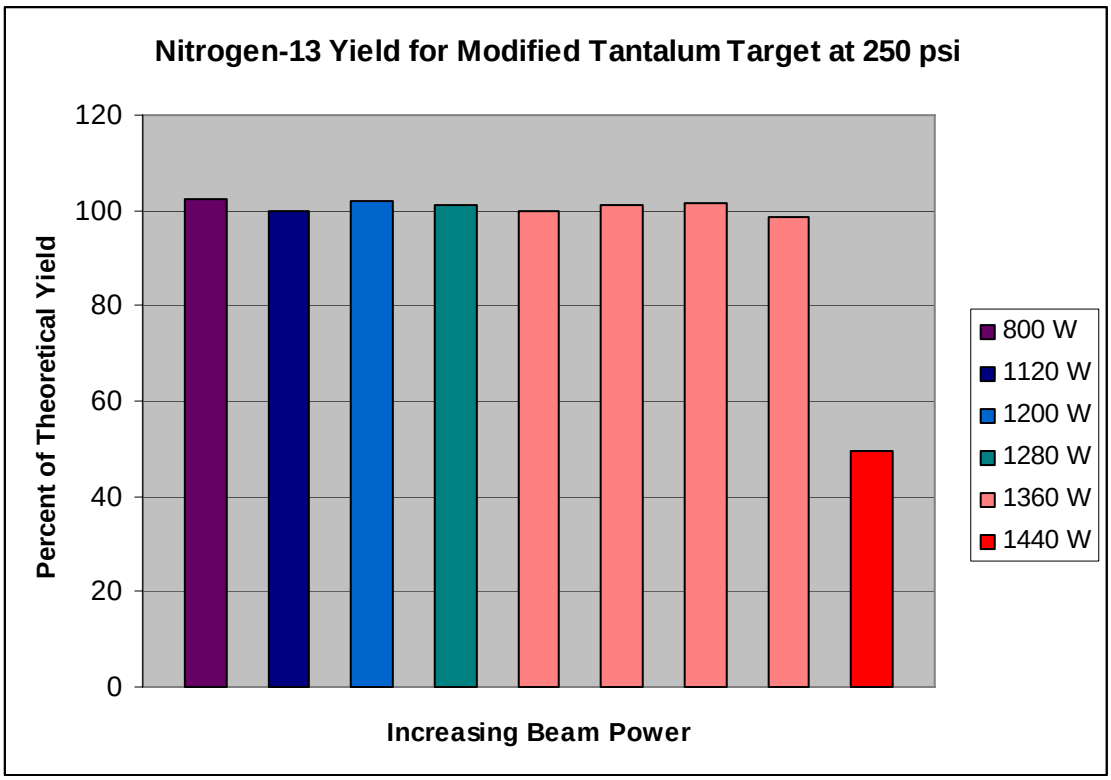

Figure 36: Nitrogen-13 Yield Data (Matthew Stokely 2008)

High ^{13}N yields for beam power between 800 and 1360 W suggest target operation with no beam penetration. At 1440 W, a pronounced decrease in the ^{13}N yield was observed, suggesting beam penetration. This is consistent with the observed sight tube data, but suggests a slightly higher thermal limit of roughly 1360 W. Yield measurements can be inaccurate if radioactive material is trapped in the target or if residual radiation from a

previous run is released with the new yield. Although the low yield suggests beam penetration, additional yield measurements are needed to ensure statistical accuracy.

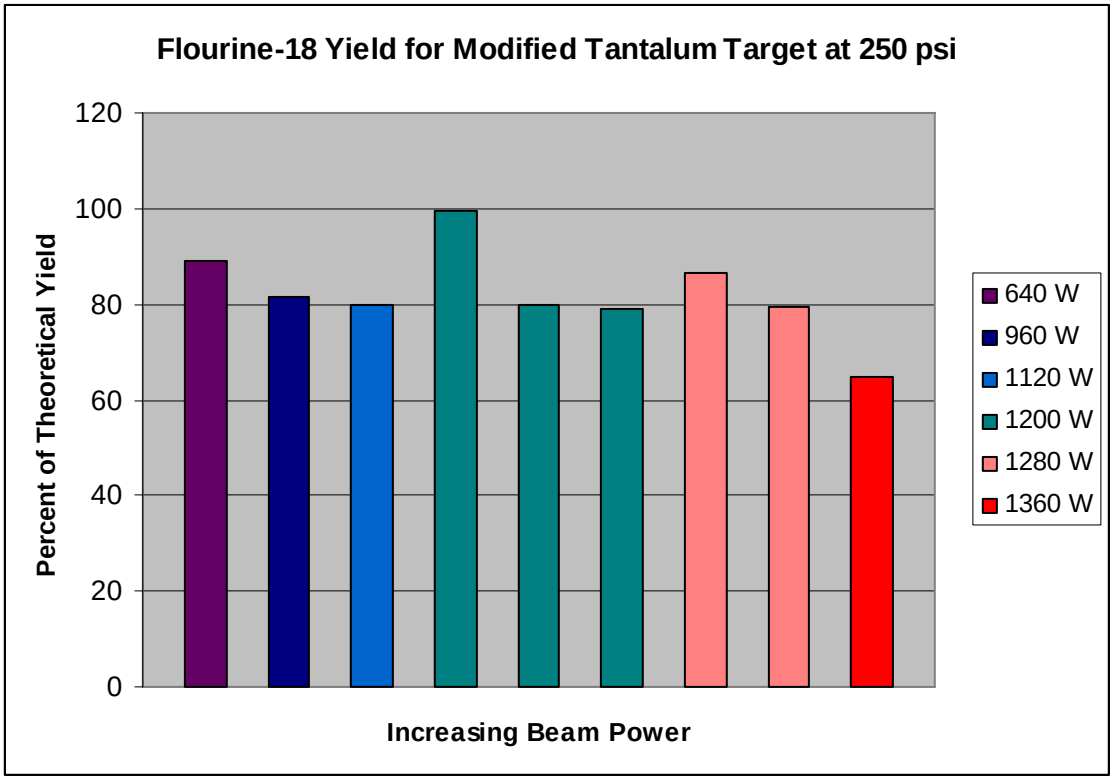

Figure 37: Flourine-18 Yield Data (Matthew Stokely 2008)

Flourine-18 yield was measured using enriched water for beam power between 640 and 1360 W. The yield measurements between 640 and 1280 W are all around 80% of the theoretical saturation yield, which is consistent with target operation with no beam penetration. A slight decrease was observed in the percent yield for 1360 W beam power. This decrease could be due to the onset of beam penetration, consistent with a thermal limit of 1280 W, or it could be due to fluorine trapping. Once again, more yield measurements are needed to ensure statistical accuracy.

6.7 Material Comparison for Modified Test Target

Sight tube data was collected at 250 psi for both the silver and tantalum versions of the modified test target. This allows for a direct material comparison of average volume displacement, or corresponding target void, as a function of heat input.

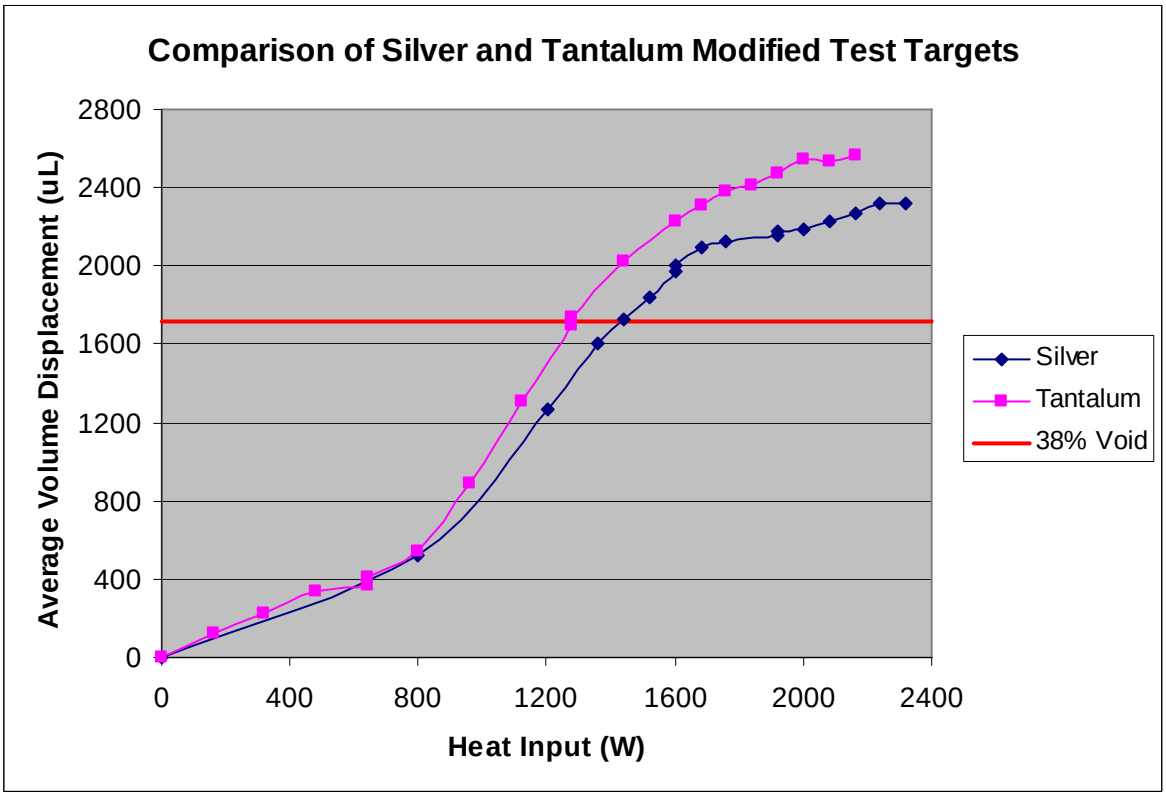

Figure 38: Comparison of Silver and Tantalum Modified Test Targets

Under 250 psi operating conditions, heat inputs of 1280 W for the tantalum target and 1460 W for the silver target resulted in 38% average void in the target chamber. This indicates a penalty of 11% in heat removal capacity for the tantalum target. A 17% penalty was predicted using the thermosyphon computer models for a larger target operating under two-region boiling conditions. The reduced penalty is most likely due to the reduction in the conduction distance which was implemented for the smaller target.

6.8 Observed Thermal Limit for Wisconsin Targets

Changes in the sight tube data which suggest the onset of beam penetration have been identified for three Wisconsin targets. Target performance and integrity suffer when beam penetration occurs, so this point represents the effective thermal limit of each target. If the thermally limiting condition, i.e. maximum tolerable void fraction in the target chamber, can be identified, it may be possible to predict the maximum available performance of new targets using the computer models. The maximum volume displacement at the observed thermal limit can be used to infer the maximum void fraction in the target to result in the thermally limiting condition. The volume averaged boiling model has been shown to predict thermal performance as a function of heat input well, for targets of this size. Accordingly, identification of the observed fluctuations in the target chamber at the thermal limit, maximum and average void fraction, can be used to predict the thermal limit of targets using the results of the volume averaged boiling computer model. A comparison of the observed limiting void to the theoretical void limit, based on the range of protons in water, can provide some insight into the degree of non-uniformity in the void distribution.

Table 23: Observed Thermal Limit for Wisconsin Targets

Target Width (mm)	Target Material	Prz (psi)	$\dot{Q}$ (W)	Maximum Void (%)	Theoretical Void Limit (%)	Minimum Void (%)	Average Void (%)	Model Void (%)
15	Silver	400	1760	54.4	79.1	22.4	38.4	42.5
13.5	Silver	250	1400	51.0	76.7	27.3	39.2	-
13.5	Silver	400	1640	57.0	76.3	26.0	41.5	-
13.5	Tantalum	250	1280	52.3	76.7	25.0	38.7	-

In general, the maximum heat input to result in the thermal limit is expected to increase with pressure and to be higher for silver than tantalum. The observed limits for the three Wisconsin targets are consistent with these predictions. The observed thermal limit for

the three Wisconsin targets corresponds to maximum void in the target chamber between 51 and 57%. This is significantly below the theoretical value of roughly 76%, which suggests that the distribution of void is not uniform in the chamber. The minimum displacement level under penetrating conditions corresponds to a smaller amount of void, and the targets are shown to oscillate over a range of more than 25% at the thermal limit. For the 15 mm silver target, the model does a reasonable job of predicting the average displacement level corresponding to the heat input at which beam penetration is observed. The average void fraction predicted by the model at the thermal limit is greater than the observed average void fraction by 4% void.

6.9 Critical Heat Flux

Critical heat flux on the window foil during target operation should be avoided, as it could result in foil rupture or sputtering of contaminants off of the foil into the product water. In prior work, critical heat flux and maximum window temperature in the front foil during normal operation were predicted for Duke targets and shown to fall well below the level at which window failure is predicted (Peeples, 2006). Due to the increased beam diameter, lower beam energy, and greater available beam power, similar analysis must be performed for the Wisconsin targets.

Correlations have been developed for predicting critical heat flux for pool boiling on vertical surfaces (Lienhard, 1973). For a vertical plate with one side insulated, a critical heat flux correlation is

$$\frac{q''_{crit}}{q''_{\max z}} = \begin{cases} 0.9 & 5.86 < Bo \\ \dfrac{1.4}{(H')^{1/4}} & 0.15 < Bo < 5.86 \end{cases} \tag{1}$$

The Bond number, a ratio of the gravitational forces to the surface tension, is given by

$$Bo \equiv \frac{g(\rho_f - \rho_g)L^2}{g_c \sigma} \tag{2}$$

The Zuber-Kutateladze correlation for critical heat flux on a flat plate is

$$q''_{\max z} \equiv \frac{\pi}{24} h_{fg} \rho_g^{1/2} \left[\sigma g g_c (\rho_f - \rho_g)\right]^{1/4} \tag{3}$$

Critical heat flux values can be calculated for saturated water conditions at pressures between 250 psi and 500 psi.

Table 24: Critical Heat Flux

Pressure (psi)	q''_{crit} (Btu/hr-ft^2)	q''_{crit} (W/cm^2)
250	891315	281
300	932684	294
400	1008577	318
500	1059113	334

At the Wisconsin Medical Cyclotron, protons with initial energy of 16.5 MeV strike the window foil and deposit energy in the foil as they pass through. Window foils used for Wisconsin targets are typically Havar with 0.002" thickness. The Wisconsin beam shape at the surface of the window foil has been observed experimentally and can be approximated as roughly circular with a diameter of 14 mm. Energy deposition in the window foil can be estimated using SRIM (Matthew Stokely 2008).

Table 25: Heat Generation in 0.002" Havar Foil (Matthew Stokely 2008)

E (MeV)	$\frac{\partial E}{\partial x}$ (MeV/mm)	$\frac{q}{\mu A}$ (W/μA)	$\frac{q''_{avg}}{I}$ (W/cm^2- μA)	$\frac{q'''_{avg}}{I}$ (W/cm^3- μA)
16	16.38	0.832	0.541	106.4

For a production run, the maximum feasible operating beam current is 100 μA. For experimental testing and target characterization, beam currents as high as 150 μA are achievable. Average heat flux in the window foil can be calculated for these beam currents. The beam is not uniform, so maximum heat flux is expected to exceed the average heat flux value by some peak to average ratio. This ratio has been estimated to be roughly 2.5 for the Duke cyclotron. Insufficient data has been collected to predict the peak to average ratio for the Wisconsin cyclotron, but it is expected to be no greater than that of the Duke machine. The critical peak to average ratio (R_{pta}^{crit}) that would result in critical heat flux on the window foil can be determined and compared to the assumed value of 2.5.

Table 26: Critical Peak to Average Ratio for Wisconsin Targets

Pressure (psi)	$q''_{avg}(100\,\mu A)$ (W/cm^2)	$q''_{avg}(150\,\mu A)$ (W/cm^2)	q''_{crit} (W/cm^2)	$R_{pta}^{crit}(100\,\mu A)$	$R_{pta}^{crit}(150\,\mu A)$
250	54.1	81.2	281	5.2	3.5
300	54.1	81.2	294	5.4	3.6
400	54.1	81.2	318	5.9	3.9
500	54.1	81.2	334	6.2	4.1

Critical peak to average ratios between 5 and 6 indicate that heat flux in the target window is not expected to exceed the critical heat flux under normal operating conditions. During experimental tests at low pressure, the critical peak to average ratio is as low as 3.5, suggesting that critical heat flux could be an issue.

The same analysis can be used to assess the potential to undergo critical heat flux for cyclotron beams of similar size for both Havar and tantalum window foils with reasonable thicknesses of 0.001" and 0.002" for a range of proton energies.

Table 27: Critical Peak to Average Ratios at 100 μA, 250 psi

E (MeV)	0.001" Tantalum	0.002" Tantalum	0.001" Havar	0.002" Havar
30	11.8	5.9	17.2	8.6
25	10.3	5.2	14.9	7.5
16	7.6	3.8	10.4	5.2
12	6.2	3.1	8.6	4.3
8	4.8	2.4	6.4	3.2

Table 28: Critical Peak to Average Ratios at 150 μA, 250 psi

E (MeV)	0.001" Tantalum	0.002" Tantalum	0.001" Havar	0.002" Havar
30	7.8	3.9	11.4	5.7
25	6.9	3.4	10.0	5.0
16	5.0	2.5	6.9	3.5
12	4.1	2.1	5.7	2.9
8	3.2	1.6	4.2	2.1

Table 29: Critical Peak to Average Ratios at 100 μA, 400 psi

E (MeV)	0.001" Tantalum	0.002" Tantalum	0.001" Havar	0.002" Havar
30	13.3	6.7	19.4	9.7
25	11.7	5.8	16.9	8.4
16	8.6	4.3	11.8	5.9
12	7.0	3.5	9.7	4.8
8	5.4	2.7	7.2	3.6

Table 30: Critical Peak to Average Ratios at 150 μA, 400 psi

E (MeV)	0.001" Tantalum	0.002" Tantalum	0.001" Havar	0.002" Havar
30	8.9	4.4	12.9	6.5
25	7.8	3.9	11.3	5.6
16	5.7	2.9	7.8	3.9
12	4.7	2.3	6.5	3.2
8	3.6	1.8	4.8	2.4

In general, tantalum foils must be supported by a shadow grid, so 0.001" thickness is reasonable. For Havar foils, 0.002" thickness may be required for larger windows. These results indicate that critical heat flux could become an issue for 16 MeV cyclotrons for around 150 μA on Havar. For 8 MeV cyclotrons, critical heat flux could become an issue around 100 μA on Havar and 150 μA on Tantalum.

Chapter 7

Potential Design Enhancements for Future Targets

7.1 Evaluation of Turbulent Boiling Target Designs

Thermosyphon targets were intended to operate in a two-region boiling mode, with formation of a distinct condensing region in the top of the target chamber. For this reason, target chambers were designed with heights significantly greater than the beam width, in order to accommodate the condensing region without leading to beam penetration. Experimental testing has indicated that test targets of the size of interest, operating at the available beam power, operate in a turbulent boiling mode without transitioning to a two-region boiling mode. Under these conditions, there is no clear advantage to designing target chambers with greater height than width. A target chamber can be designed with a circular chamber cross-section, rather than the oblong style currently favored, that maintains the same available surface area for cooling with a reduced target volume and increased depth. Target chamber designs with circular cross-sections also offer mechanical advantages and are more easily fabricated.

The silver test target with 15 mm chamber width was the only Wisconsin test target that appeared to have thermal capacity high enough for operation at the highest feasible beam power for production. Accordingly, its chamber size was used as a reference to investigate the potential advantage of cylindrical target chambers. Three target designs were proposed for modeling in tantalum, each with the same target chamber surface area for cooling,

conduction distance, and style of radial coolant channels. The turbulent boiling computer model was used to predict average void fraction in the target chamber as a function of heat input for each target, assuming parallel cooling lines with 71 psi pressure header and use of an optimized jet.

Table 31: Geometry Comparison for Equivalent Surface Area Targets

Design	Height (mm)	Width (mm)	Depth (mm)	Back Th. (in)	Volume (cc)
Original	22.5	15	15	0.04	4.34
Cylinder	17	17	18.6	0.04	4.22
Cylinder	15	15	22.2	0.04	3.92

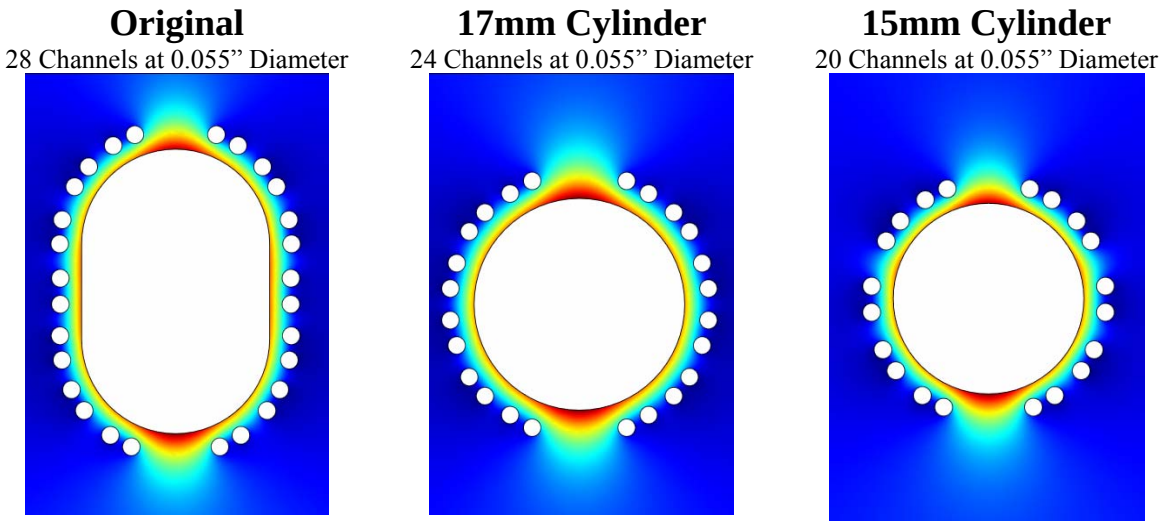

Figure 39: COMSOL Radial Temperature Profiles for Equivalent Surface Area Targets

Table 32: Volume Averaged Boiling Model Predictions for Original Target at 400 psi

$\dot{Q}$ (W)	I (μA)	ΔV_{exp} (μL)	α
365	22.8	737.4	0
973	60.8	844.1	0.025
1122	70.1	950.7	0.05
1217	76.1	1057.4	0.075
1289	80.6	1164.1	0.1
1346	84.1	1270.8	0.125
1394	87.1	1377.4	0.15
1436	89.8	1484.1	0.175
1472	92.0	1590.8	0.2
1505	94.1	1697.4	0.225
1535	95.9	1804.1	0.25
1563	97.7	1910.8	0.275
1588	99.3	2017.5	0.3
1611	100.7	2124.1	0.325
1633	102.1	2230.8	0.35
1654	103.4	2337.5	0.375
1673	104.6	2444.1	0.4
1692	105.8	2550.8	0.425
1709	106.8	2657.5	0.45
1726	107.9	2764.1	0.475
1741	108.8	2870.8	0.5
1757	109.8	2977.5	0.525
1771	110.7	3084.2	0.55
1785	111.6	3190.8	0.575
1798	112.4	3297.5	0.6
1811	113.2	3404.2	0.625
1824	114.0	3510.8	0.65
1836	114.8	3617.5	0.675
1847	115.4	3724.2	0.7
1859	116.2	3830.9	0.725
1869	116.8	3937.5	0.75
1880	117.5	4044.2	0.775
1890	118.1	4150.9	0.8
1900	118.8	4257.5	0.825
1910	119.4	4364.2	0.85
1919	119.9	4470.9	0.875
1929	120.6	4577.6	0.9

Table 33: Volume Averaged Boiling Model Predictions for 17mm Cylinder Target at 400 psi

$\dot{Q}$ (W)	I (μA)	ΔV_{exp} (μL)	α
363	22.7	718.0	0
1020	63.8	821.9	0.025
1173	73.3	925.7	0.05
1270	79.4	1029.6	0.075
1342	83.9	1133.5	0.1
1400	87.5	1237.3	0.125
1448	90.5	1341.2	0.15
1490	93.1	1445.1	0.175
1527	95.4	1548.9	0.2
1560	97.5	1652.8	0.225
1590	99.4	1756.7	0.25
1617	101.1	1860.5	0.275
1642	102.6	1964.4	0.3
1666	104.1	2068.2	0.325
1688	105.5	2172.1	0.35
1708	106.8	2276.0	0.375
1727	107.9	2379.8	0.4
1746	109.1	2483.7	0.425
1763	110.2	2587.6	0.45
1779	111.2	2691.4	0.475
1795	112.2	2795.3	0.5
1810	113.1	2899.2	0.525
1824	114.0	3003.0	0.55
1838	114.9	3106.9	0.575
1851	115.7	3210.8	0.6
1864	116.5	3314.6	0.625
1876	117.3	3418.5	0.65
1888	118.0	3522.4	0.675
1900	118.8	3626.2	0.7
1911	119.4	3730.1	0.725
1922	120.1	3833.9	0.75
1932	120.8	3937.8	0.775
1942	121.4	4041.7	0.8
1952	122.0	4145.5	0.825
1962	122.6	4249.4	0.85
1971	123.2	4353.3	0.875
1980	123.8	4457.1	0.9

Table 34: Volume Averaged Boiling Model Predictions for 15mm Cylinder Target at 400 psi

$\dot{Q}$ (W)	I (μA)	ΔV_{exp} (μL)	α
365	22.8	665.6	0
1065	66.6	761.9	0.025
1226	76.6	858.2	0.05
1329	83.1	954.5	0.075
1406	87.9	1050.8	0.1
1467	91.7	1147.1	0.125
1519	94.9	1243.4	0.15
1564	97.8	1339.7	0.175
1603	100.2	1435.9	0.2
1638	102.4	1532.2	0.225
1670	104.4	1628.5	0.25
1700	106.3	1724.8	0.275
1726	107.9	1821.1	0.3
1752	109.5	1917.4	0.325
1775	110.9	2013.7	0.35
1797	112.3	2110.0	0.375
1818	113.6	2206.3	0.4
1837	114.8	2302.5	0.425
1856	116.0	2398.8	0.45
1873	117.1	2495.1	0.475
1890	118.1	2591.4	0.5
1906	119.1	2687.7	0.525
1922	120.1	2784.0	0.55
1936	121.0	2880.3	0.575
1951	121.9	2976.6	0.6
1964	122.8	3072.9	0.625
1978	123.6	3169.1	0.65
1990	124.4	3265.4	0.675
2003	125.2	3361.7	0.7
2015	125.9	3458.0	0.725
2026	126.6	3554.3	0.75
2037	127.3	3650.6	0.775
2048	128.0	3746.9	0.8
2059	128.7	3843.2	0.825
2069	129.3	3939.5	0.85
2079	129.9	4035.7	0.875
2089	130.6	4132.0	0.9

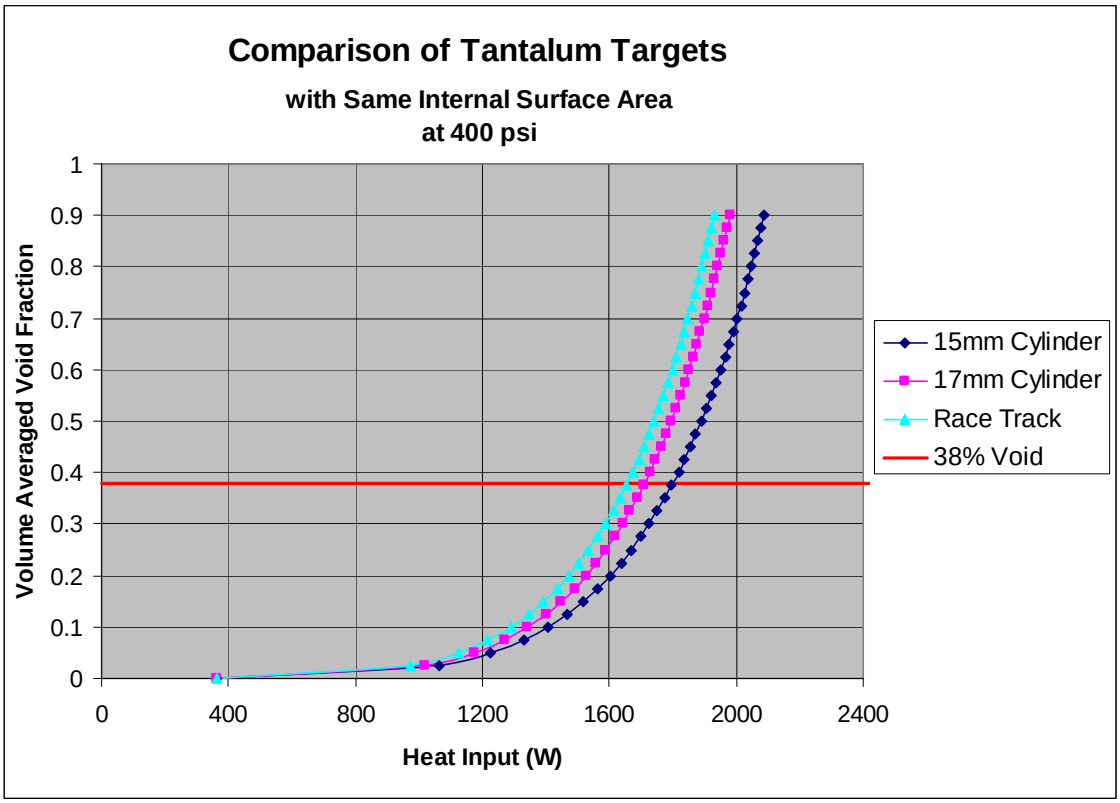

Figure 40: Thermal Performance Predictions for Equivalent Surface Area Targets

The cylindrical targets are shown to dissipate the same heat inputs with lower average void in the target chambers, indicating higher thermal limits. The cylindrical targets also have greater depth, which should also result in higher thermal limits. For these targets, the conduction distance in the radial direction is less than the conduction distance through the back of the target. As a result, the 15 mm cylindrical target out performs the 17 mm target because more of its surface area for heat transfer is located along the radial direction. Experimental tests with targets having 15mm and 13.5mm depths were observed to have thermal limits corresponding to average void fraction of roughly 38%. If this behavior holds, all three targets are predicted to have thermal limits above the highest feasible normal operation beam power at the Wisconsin Medical Cyclotron of 1.6 kW.

7.2 Material Comparison for Cylindrical Target

Initial modeling results indicated that cylindrical targets may offer enhanced thermal performance over the traditional race track design. A diameter of 17mm was selected for further investigation because it offers an advantage over the classic design while still maintaining a large cross-section for bubble dispersion. The radial coolant configuration was improved from the previous model to feature 4 additional coolant channels and a reduced radial conduction distance. An aluminum test target is currently being fabricated for testing at the Wisconsin facility, using the alloy Aluminum 6061 Temper-T6. Aluminum is unsuitable for a production target because it traps fluorine, but it can be used as a test target to observe thermal performance and to perform Nitrogen-13 yield tests. Although Flourine-18 yield tests cannot be performed, aluminum offers some advantages over silver for a test target because it does not activate and does not release mobile contaminants into the piping. Average void in the target chamber as a function of heat input was predicted for the aluminum test target and for a geometrically identical tantalum target, which would be suitable for production.

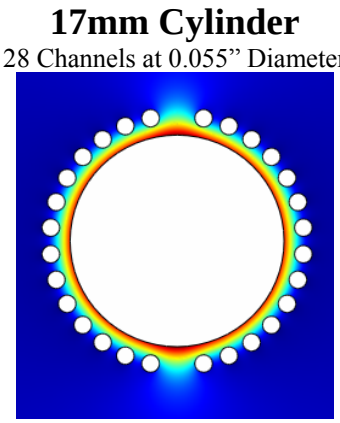

Figure 41: COMSOL Radial Temperature Profile for 17mm Cylindrical Target

Table 35: Volume Averaged Boiling Model Predictions for Aluminum 6061 Target at 400 psi

$\dot{Q}$ (W)	I (μA)	ΔV_{exp} (μL)	α
378	23.6	718.0	0
1142	71.4	821.9	0.025
1337	83.6	925.7	0.05
1464	91.5	1029.6	0.075
1560	97.5	1133.5	0.1
1638	102.4	1237.3	0.125
1705	106.6	1341.2	0.15
1763	110.2	1445.1	0.175
1814	113.4	1548.9	0.2
1861	116.3	1652.8	0.225
1903	118.9	1756.7	0.25
1943	121.4	1860.5	0.275
1979	123.7	1964.4	0.3
2013	125.8	2068.2	0.325
2045	127.8	2172.1	0.35
2075	129.7	2276.0	0.375
2103	131.4	2379.8	0.4
2130	133.1	2483.7	0.425
2156	134.8	2587.6	0.45
2180	136.3	2691.4	0.475
2204	137.8	2795.3	0.5
2226	139.1	2899.2	0.525
2248	140.5	3003.0	0.55
2269	141.8	3106.9	0.575
2289	143.1	3210.8	0.6
2308	144.3	3314.6	0.625
2327	145.4	3418.5	0.65
2345	146.6	3522.4	0.675
2362	147.6	3626.2	0.7
2380	148.8	3730.1	0.725
2396	149.8	3833.9	0.75
2412	150.8	3937.8	0.775
2428	151.8	4041.7	0.8
2443	152.7	4145.5	0.825
2458	153.6	4249.4	0.85
2473	154.6	4353.3	0.875
2487	155.4	4457.1	0.9

Table 36: Volume Averaged Boiling Model Predictions for Tantalum Target at 400 psi

$\dot{Q}$ (W)	I (μA)	ΔV_{exp} (μL)	α
370	23.1	718.0	0
1074	67.1	821.9	0.025
1244	77.8	925.7	0.05
1353	84.6	1029.6	0.075
1435	89.7	1133.5	0.1
1502	93.9	1237.3	0.125
1557	97.3	1341.2	0.15
1606	100.4	1445.1	0.175
1648	103.0	1548.9	0.2
1687	105.4	1652.8	0.225
1722	107.6	1756.7	0.25
1754	109.6	1860.5	0.275
1783	111.4	1964.4	0.3
1811	113.2	2068.2	0.325
1836	114.8	2172.1	0.35
1860	116.3	2276.0	0.375
1883	117.7	2379.8	0.4
1905	119.1	2483.7	0.425
1925	120.3	2587.6	0.45
1945	121.6	2691.4	0.475
1964	122.8	2795.3	0.5
1981	123.8	2899.2	0.525
1999	124.9	3003.0	0.55
2015	125.9	3106.9	0.575
2031	126.9	3210.8	0.6
2046	127.9	3314.6	0.625
2061	128.8	3418.5	0.65
2075	129.7	3522.4	0.675
2089	130.6	3626.2	0.7
2102	131.4	3730.1	0.725
2115	132.2	3833.9	0.75
2128	133.0	3937.8	0.775
2140	133.8	4041.7	0.8
2152	134.5	4145.5	0.825
2163	135.2	4249.4	0.85
2175	135.9	4353.3	0.875
2186	136.6	4457.1	0.9

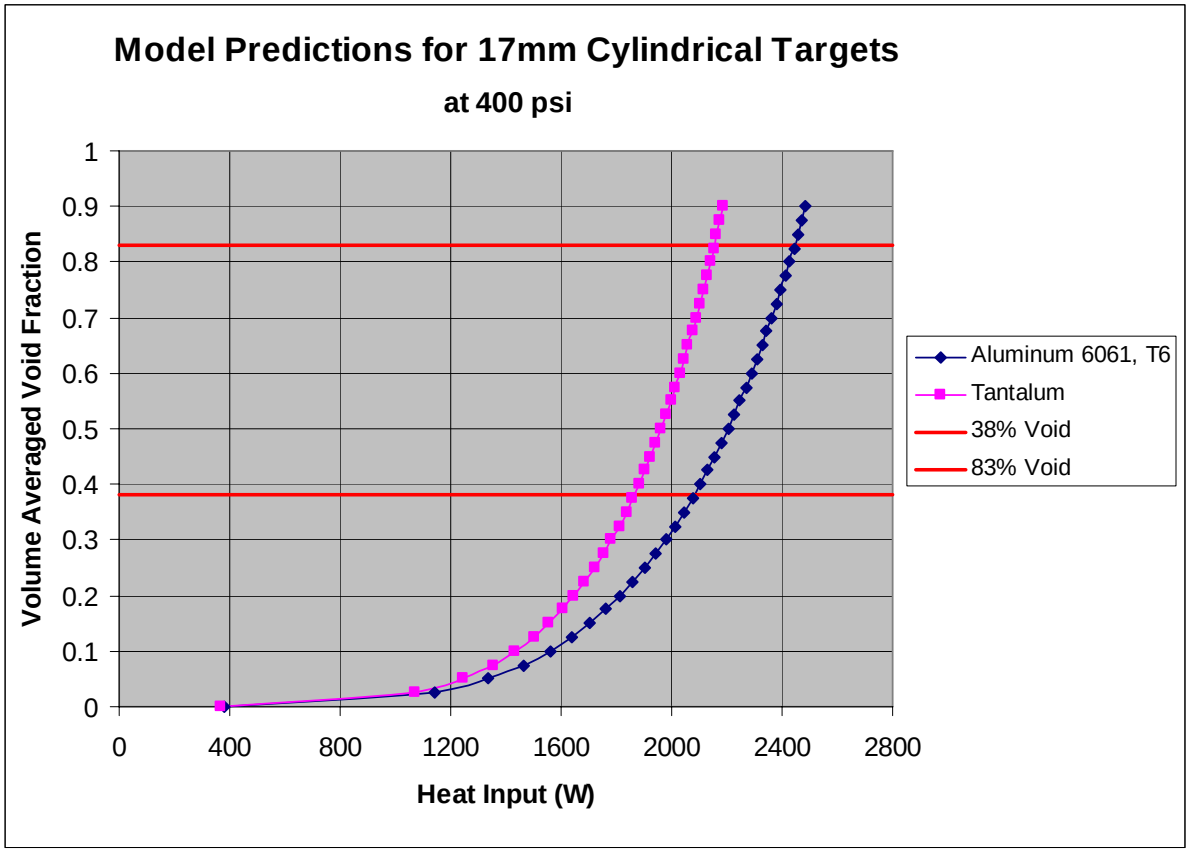

Figure 42: Thermal Performance Predictions for 17mm Cylindrical Targets

Experimental test targets with 15mm and 13.5mm depths were observed to have thermal limits corresponding to average void fraction of roughly 38%. The theoretical void limit for this target is 83%, slightly higher than that of the prior test targets due to increased depth. The thermal limit for the new aluminum test target and for a geometrically identical tantalum production target has been estimated using the computer models, under the somewhat conservative assumption of a 38% average void limit. Under these assumptions, both the aluminum and tantalum 17 mm cylindrical targets are expected to have thermal limits above 1.6 kW, the highest beam power for production. Using the predicted heat input to result in 38% average void in the target chamber, a 10.4% penalty is expected for

replacing the aluminum target with the identical tantalum target. There is a smaller penalty than when silver and tantalum are compared because the difference in the thermal conductivity values is much smaller.

7.3 Assessment of Potential for Operation in Alternate Boiling Modes

Thermosyphon targets were originally intended to operate in a two-region boiling mode, with formation of a distinct condensing region in the top of the target chamber. Evidence suggests that the experimental test targets to date have operated under turbulent boiling conditions without the formation of a distinct condensing region. Now that computer models have been developed to predict target performance for different boiling dynamics, model predictions can be used to assess any potential enhancement in target thermal performance that would exist if two-region boiling conditions could be achieved in a target. If a large benefit is predicted, target chamber size and relative dimensions can be adjusted to try to stimulate two-region boiling in future targets.

Two potential correlations have been proposed for the condensing heat transfer coefficient, developed for film condensation on a vertical plate and laminar condensation within a horizontal tube. No experimental data has been collected to support the selection of which form is appropriate for thermosyphon targets; however, the target geometry is most similar to that associated with the horizontal tube correlation. A sensitivity analysis performed for thermosyphon targets identified the condensing heat transfer coefficient as the most significant factor governing uncertainty in the predicted target performance (Peeples, 2006). The study indicated that performance predictions are much less sensitive to other factors, such as the vapor velocity. Accordingly, thermal performance can be predicted using

each of the two forms of the condensing heat transfer coefficient to indicate the predicted range of uncertainty.

In order to assess any predicted improvement associated with two-region boiling, thermal performance was predicted for a reference target assuming each of the three boiling dynamics discussed, turbulent boiling and two region boiling with each of two condensing heat transfer coefficient correlations. The reference target design was the same used to assess the potential for cylindrical targets, which featured a classic race track shaped chamber with 22.5mm height, 15mm width, and 15mm depth in tantalum. Thermal performance was predicted for each boiling condition up to an assumed thermal limit of 38% void in the boiling region or low level of 15mm boiling height.

Table 37: Volume Averaged Boiling Model Predictions at 400 psi

$\dot{Q}$ (W)	ΔV_{exp} (μL)	α
368	737.4	0
1083	844.1	0.025
1250	950.7	0.05
1357	1057.4	0.075
1437	1164.1	0.1
1501	1270.8	0.125
1555	1377.4	0.15
1602	1484.1	0.175
1643	1590.8	0.2
1680	1697.4	0.225
1714	1804.1	0.25
1745	1910.8	0.275
1773	2017.5	0.3
1800	2124.1	0.325
1824	2230.8	0.35
1847	2337.5	0.375

Table 38: Two Region Boiling Model Predictions (Horizontal Tube) at 400 psi

$\dot{Q}$ (W)	H_{boil} (mm)	Boiling Region α
1119	21	0.054
1245	20	0.091
1333	19	0.126
1403	18	0.159
1459	17	0.189
1505	16	0.217
1547	15	0.243

Table 39: Two Region Boiling Model Predictions (Vertical Plate) at 400 psi

$\dot{Q}$ (W)	H_{boil} (mm)	Boiling Region α
1699	21	0.200
1779	20	0.238
1833	19	0.267
1874	18	0.291
1905	17	0.312
1931	16	0.331
1952	15	0.347

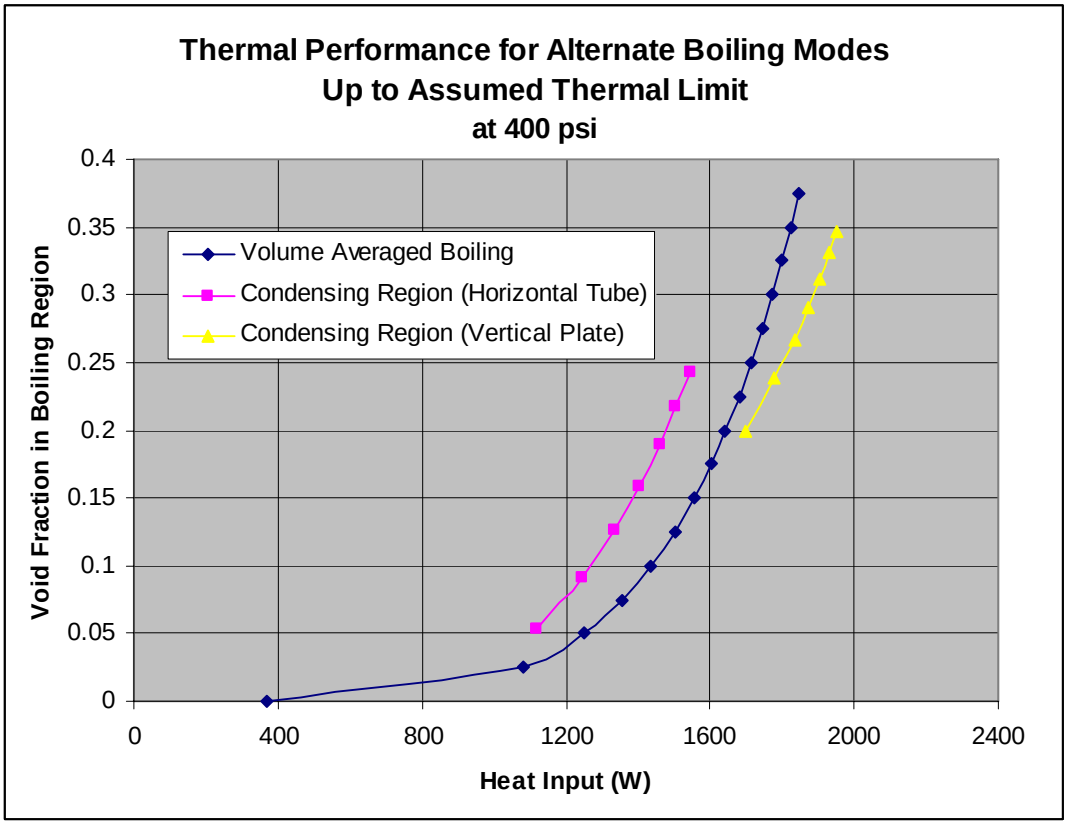

Figure 43: Thermal Performance Predictions for Alternate Boiling Modes

Model predictions which assume formation of a distinct condensing region with heat transfer governed by the horizontal tube condensation correlation show a significant reduction in thermal performance when compared to the turbulent boiling model predictions. When the correlation for film condensation on a vertical plate is used, a slight improvement in thermal performance over the turbulent boiling model is predicted. For the assumed thermally limiting conditions, the estimated thermal limit is increased by 100 W. This study suggests that there is no clear advantage to operating in a two-region boiling mode and that there may be a significant penalty. Determination of transition criteria between the turbulent boiling and two-region boiling mode is still of interest, though whether such a transition should be stimulated or avoided remains unclear.

Chapter 8

Conclusions

8.1 Summary and Conclusions

The primary purpose of this work was to develop a fundamental approach to target design from a modeling perspective, and to implement this approach to design new thermosyphon targets with enhanced production capabilities. Computational methods were developed to support target design, and validated by experimental testing of targets at both the Duke and Wisconsin cyclotrons.

Estimates of the mass flow rates in the radial and jet cooling systems generated using a characteristic forms loss model were validated by experimental flow measurements. Sight tube data was collected for two tantalum targets at Duke. Sight tube data indicated target operation under non-equilibrium conditions. The sight tube data suggested the occurrence of subcooled boiling, followed by operation in a turbulent boiling mode. There was good agreement between the experimental data and the volume averaged boiling model for average void fractions between 2.5 and 10%. Operational thermal limits were observed corresponding to maximum target void fraction of roughly 38% and average void fraction of 7 to 9%. A tantalum thermosyphon production target (TS-6) was qualified for use at the Duke cyclotron, and qualifying tests indicated good FDG yields. The new target resulted in more than a factor of 2 improvement in fluoride production capability at the Duke PET facility.

Sight tube data was collected for two silver Wisconsin test targets and one tantalum test target. Oscillation behavior suggested subcooled boiling at low heat input, followed by turbulent boiling at higher heat input. There was good agreement between the experimental data on the first silver test target and the volume averaged boiling model for heat inputs between 1280W and 1760W, corresponding to average void fractions between 7.5 and 42.5%. Operational thermal limits were observed corresponding to maximum target void fractions between 51 and 57% and average void fractions between 38 and 41%.

Critical heat flux calculations indicated that for Wisconsin targets, the target window is not expected to experience critical heat flux under normal operating conditions. However, critical heat flux could become an issue under experimental conditions at high beam current and low target pressure. Additional critical heat flux calculations indicated that critical heat flux could become an issue for 16 MeV cyclotrons around 150 μA on Havar and for 8 MeV cyclotrons around 100 μA on Havar and 150 μA on Tantalum.

Initial modeling results indicated that cylindrical target chambers may offer enhanced thermal performance over the traditional race track design. Cylindrical targets are predicted to dissipate the same heat inputs with lower average void in the target chambers, indicating higher thermal limits. Cylindrical targets also have greater depth, which should also result in higher thermal limits. An aluminum test target with a cylindrical target chamber of 17 mm diameter and 18.6 mm length is currently being fabricated for testing at the Wisconsin Medical Cyclotron. If this target operates as predicted and can produce high yields, it will be the first successful target design driven by computer modeling, rather than the conventional empirical approach.

8.2 Future Work

An aluminum test target with a cylindrical target chamber is currently being fabricated for testing at the Wisconsin Medical Cyclotron. If the experimental results are favorable, this could lead target design in a new direction.

There are still questions to be answered in the field of advanced target design. Among them is determination of the conditions under which thermosyphon target operation transitions from turbulent boiling into a two-region boiling mode with a distinct condensing region and whether such a transition will result in an enhancement or a penalty in target thermal performance. Computational models have been shown to be capable of predicting the average vapor volume fraction within the target over a wide range of operating conditions. Experimental data indicates that the actual target average vapor volume fraction oscillates significantly about this value, and that non-uniformity in the beam may result in local vapor volume fractions in the beam path that are significantly greater than the average. This implies that design decisions regarding appropriate target depth can not be made based on calculations of range thickness assuming uniform void distributions. Methods to quantify the margin in void fraction needed to prevent beam penetration as a function of beam distribution, chamber dimensions, and operating pressure are therefore needed to improve the design of boiling water targets.

List of References

Alvord CW, Williamson AC, Graves TL and Zigler SS. "Design, test and widespread implementation of a compact kilo-Watt fluoride ion target," *Nuclear Instruments and Methods in Physics Research B*, vol. 241, 2005.

Berridge MS, Voelker KW, and Bennington B. "High-yield, low-pressure [^{18}O] water targets of titanium and niobium for F-18 production on MC-17 cyclotrons," *Applied Radiation and Isotopes*, vol. 57, 2002.

Berridge, MS and Kjellström R. "Design and use of [^{18}O]water targets for [^{18}F]fluoride production," *Applied Radiation and Isotopes*, vol. 50, 1999.

Brdlik PM and Savin VK. "Heat Transfer Between an Axisymmetric Jet and a Plate Normal to the Flow," *Journal of Engineering Physics*, vol. 8, 1965.

Clark JC. High-Powered Cyclotron Recirculating Targets for Production of the ^{18}F Radionuclide. North Carolina State University. Raleigh, North Carolina: 2004.

Collier JG. Convective Boiling and Consensation. Second Edition. UK: McGraw-Hill Book Company, 1972.

Faw RE and Shultis JK. Radiological Assessment: Sources and Doses. Illinois: American Nuclear Society, 1999.

Frost HJ and Ashby MF. Deformation-Mechanism Maps: The Plasticity and Creep of Metals and Ceramics. Pergamon Press: 1982.

Idelchik IE. Handbook of Hydraulic Resistance. Third Edition. Florida: CRC Press, 1994.

Incropera FP and Dewitt DP. Fundamentals of Heat and Mass Transfer. Fourth Edition. New York: John Wiley & Sons, 1996.

Incropera FP, Dewitt DP, Bergman TL and Lavine AS. Introduction to Heat Transfer. Fifth Edition. New York: John Wiley & Sons, 2007.

Keenan JH and Keyes FG. Thermodynamic Properties of Steam. First Edition. New York: John Wiley & Sons, 1936.

Lekakh BM, Meyer JE and Kazimi MS. "Heat Transfer Conditions in Water-Cooling of a Fusion Reactor Divertor," *IEEE*, 1995.

Lienhard JP and Dhir VK. "Hydrodynamic Prediction of Peak Pool-boiling Heat Fluxes from Finite Bodies," *ASME Journal of Heat Transfer*, vol. 95, 1973.

Martin H. "Heat and Mass Transfer Between Impinging Gas Jets and Solid Surfaces," *Advances in Heat Transfer*, vol. 13, 1977.

Mills AF. Heat Transfer. Second Edition. New Jersey: Prentice Hall, 1999.

Newnam R, Doster JM and Wieland B. "Heat Exchangers For Recirculating Water Targets," *Proceedings of the Eleventh International Workshop on Targetry and Target Chemistry.* Cambridge, United Kingdom: 2006.

Newnam RP. "High Capacity Heat Exchangers for Recirculating 18F Radionuclide Production Targets," *Master of Science Thesis*. North Carolina State University, 2007. <http://www.lib.ncsu.edu/theses/available/etd-03212007-150136/>

Nuclides and Isotopes. Fifteenth Edition. California: General Electric and KAPL, 1996.

Peeples JL. "Design and Optimization of Thermosyphon Batch Targets for Production of ^{18}F," *Master of Science Thesis*. North Carolina State University, 2006. <http://www.lib.ncsu.edu/theses/available/etd-11092006-180341/>

Robb RA. Three-Dimensional Biomedical Imaging, Volume 2. Florida: CRC Press, 2000.

Roberts AD, Daniel LC and Nickles RJ. "A high power target for production of [^{18}F] fluoride," *Nuclear Instruments and Methods in Physics Research B,* vol. 95, 1995.

Roberts AN. Thermosyphon Targets Designed for the Production of ^{18}F for Use in Positron Emission Tomography. North Carolina State University. Raleigh, North Carolina: 2002.

Sitharamayya S and Raju KS. "Heat Transfer Between an Axisymmetric Jet and a Plate Held Normal to the Flow," *The Canadian Journal of Chemical Engineering*, vol. 47, 1969.

Stokely MH. "Deployment, Testing and Analysis of Advanced Thermosyphon Target Systems for Production of Aqueous [^{18}F] Fluoride via ^{18}O(p,n)^{18}F," *Doctor of Philosophy Dissertation*. North Carolina State University, 2008. <http://www.lib.ncsu.edu/etd/>

Strangis R and Lepera CG. "RELIABLE FLUORINE-18 [18F-] PRODUCTION AT HIGH BEAM POWER," *Proceedings of the Eighteenth International Conference on Cyclotrons and their Applications*. Giardini Naxos, Italy: 2007.

Valk PE, Bailey DL, Townsend DW and Maisey MN. Positron Emission Tomography: Basic Science and Clinical Practice. New York: Springer, 2003.

Wallis GB. One-dimensional two-phase flow. New York: McGraw Hill, 1969.

Wen D and Ding Y. "Natural Convective Heat Transfer of Suspensions of Titanium Dioxide Nanoparticles (Nanofluids)," *IEEE Transactions on Nanotechnology*, vol. 5, no. 3, 2006.

Wieland BW. "Batch Target and Method for Producing Radionuclide," United States Patent, no. US 7,127,023 B2. Issued: Oct. 24, 2006.

Wieland B, Illan C, Doster JM, Roberts A, Runkle R, Rowland C and Bida J. "Self-Regulating Thermosyphon Water Target for Production of F-18-Fluoride at Proton Beam Power of One kW and Beyond," *Proceedings of the Ninth International Workshop on Targetry and Target Chemistry*. Turku, Finland: 2002.

Womac DJ, Ramadhyani S and Incropera FP. "Correlating Equations for Impingement Cooling of Small Heat Sources With Single Circular Liquid Jets," *Transactions of the ASME*, vol. 115, 1993.

XACT Wire EDM Corp. Cary, Illinois <http://www.xactedm.com> November 1, 2006.

Zeisler SK, Becker DW, Pavan RA, Moschel R and Rühle H. "A water-cooled spherical niobium target for the production of [^{18}F]fluoride," *Applied Radiation and Isotopes*, vol. 53, 2000.